Collège Doctoral du Languedoc-Roussillon

THÈSE

Pour obtenir le grade de

Docteur

Délivré par **l'Université de Montpellier**

Préparée au sein de l'école doctorale
Science Chimique Balard Ed459
Et de l'unité de recherche
UMR5253 ICGM -AIME

Spécialité : **Chimie des Matériaux**

Présentée par **Yannick Nabil-Moreau**

Supports De Catalyseur Nanostructurés Pour Pile À Combustible À Membrane Échangeuse De Protons

Soutenue le 18 Décembre 2015 devant le jury composé de

Mme Déborah JONES, Directeur de Recherche, CNRS	Directrice de thèse
M. Francisco ALCAIDE, Directeur de Recherche, Cidetec	Rapporteur
M. Enrico TRAVERSA, Professeur, King Abdullah University of Science and Technology	Rapporteur
Mme Sara CAVALIERE, Maître de Conférences, Université de Montpellier	Co-encadrante de thèse
M. JACQUES ROZIERE, Professeur, Université de Montpellier	Examinateur
M. Jonathan SHARMAN, Directeur de Recherche, Johnson Matthey Fuel Cells	Examinateur
M. Ian HARKNESS, Directeur de Recherche, Johnson Matthey Fuel Cells	Examinateur

Collège Doctoral du Languedoc-Roussillon

THÈSE

Pour obtenir le grade de

Docteur

Delivred by the **University of Montpellier**

Prepared within the doctoral school
Science Chimique Balard Ed459
And the research unit
UMR5253 ICGM -AIME

Specialty: **Chemistry and Physicochemistry of Materials**

Presented by **Yannick Nabil-Moreau**

Novel Structured Catalyst Supports For PEM Fuel Cells

18 December 2015

Mme Déborah JONES, Research Director, CNRS	Supervisor
M. Francisco ALCAIDE, Research Director, Cidetec	Reviewer
M. Enrico TRAVERSA, Professor, King Abdullah University of Science and Technology	Reviewer
Mme Sara CAVALIERE, Lecturer, University of Montpellier	Co-Supervisor
M. JACQUES ROZIERE, Professeur, University of Montpellier	Examiner
M. Jonathan SHARMAN, Research Director, Johnson Matthey Fuel Cells	Examiner
M. Ian HARKNESS, Research Director, Johnson Matthey Fuel Cells	Examiner

Firstly I would like to express my sincere gratitude to Dr. Deborah Jones, Prof. Jacques Rozière and Dr. Sara Cavaliere who entrusted me to work freely and independently on my research and helped me to improve scientifically and personally. Their guidance has been very beneficial to me. Owing to their vast scientific knowledge and experience in the field, I had the opportunity to develop novel, interesting strategies for this challenging project. I really appreciate that they have ensured that I have received a high level of training and that they encouraged me to attend international conferences and workshops.

I am very thankful to all the members of the examination jury for taking the time to evaluate my work. I would like to thank the 2 "rapporteurs" Prof Enrico Traversa and Francisco Alcaide for their positive reports, but also my co-supervisors from Johnson Matthey: Ian Harkness, Jonathan Sharman and Graham Hards, who supported me efficiently and constantly during this project. I would like to reiterate my thanks to the members of my research committee: Dr. Deborah Jones without whose supervision the completion of this thesis would not have been possible, Prof. Jacques Rozière for assuming the role of president of the jury and for his persistent help concerning the scientific aspect of the thesis and Dr. Sara Cavaliere for her advice and the encouragement she has given me day to day throughout my PhD. As a mentor but also as a friend, she was essential in keeping me stimulated.

I would also like to acknowledge….

…Giorgio Ecolano for his constant support and for providing me with key advice related to both practical and theoretical issues. His help was very precious and the time we spent together as lab mates or as friends, in France or abroad will never be forgotten.

…Julien Bernard d'Arbigny for helping me during the crucial steps of the beginning of the project.

…Nicolas Donzel and Marc Dupont for the helpful discussions on PEM Fuel cell.

…Yannig Nedelec for the training and for helping me to setup the experiments that were necessary for this project.

…Cathy Andreux and Tatyana Pary for their help with all the administrative issues.

…Romain Berthelot, Bernard Fraisse / Julien Fullenwarth for the practical help and useful discussion on X-Ray fluorescence and X-Ray diffraction.

…Frederique Jaouen and Frederique Favier for the valuable discussions on electrochemistry.

…Geoffrey spikes, Benedict Prelot and Gilles Taillades for taking the time to share their scientific knowledge and help.

…Didier Cot, Frederic Fernandez, Franck Godiard and Erwan Oliviero for the TEM and SEM-EDX work.

I am also grateful for having been received warmly into the group in the Laboratory ICG-AIME in Montpellier, as well as in the Johnson Matthey Technical Center in Sonning Coomon during my stays. I would like to thank all my colleagues at these two institutes. Among them, Aurélien Kreisz, Laura Coustan, Alvaro Reyes, Julien Bernard d'Arbigny and Giorgio Ecolano deserve special consideration for sharing the office with me and for contributing to the great atmosphere that made these 3 years so pleasant.

I owe deep gratitude to Julie Delagenière, for her love and her inexhaustible support. Despite geographic distances, she has always been by my side, inspiring me to do my best and accompanying me with her dynamism in my determination to undertake personal and professional projects.

To my little brother Salem Nabil, thank you for your enthusiasm and good mood that helped me to keep smiling whenever I was facing difficult situations. I am highly indebted to Charles B., Florian D., Claire R., Marc D., Geoffrey B., Aziz C., David C., Tariel L., Micha B., Yeelen P., Said D., Francois Gerald F., Alexis C. … representing a long list of friends who give me the strength to stay motivated and to achieve my goals.

And last but not least, I would like to express my genuine gratitude to my mother for her generosity and for the affection with which she looked after me over the past 3 decades.

Table of contents

General introduction

A third of oil reserves, half of gas reserves and over 80 % of current coal reserves globally should remain in the ground so that the average global temperature does not exceed the 2°C above pre-industrial levels target agreed by policy makers[1]. In 2014, the Lima climate talks represented a highly significant shift towards renewable energy sources such as solar and wind. Consequently the declining production from existing oil and gas fields and the replacement of power plants or other assets that reach the end of their productive life set a major investment challenge for policy makers and the industry. The International Energy Agency wrote on the occasion of the world energy investment outlook 2014 that these declines and retirements represent “a real opportunity to change the nature of the energy system by switching fuels and by deploying more efficient technologies”[2].

The energy produced by renewable technologies needs to be stored. In this context, fuel cells combined with water electrolysers provide the opportunity to use hydrogen as energy carrier by converting solar or wind energy to chemical energy and chemical energy to electricity in the so-called "hydrogen cycle"[3]. Associated with a clean source of hydrogen, proton exchange membrane fuel cells (PEMFC) produce electricity without consuming fossil fuels[4]. The energy loss implied by the conversion of mechanical or thermal energy to electricity results in additional costs compared to fuel cells that grant a better efficiency[5]. Moreover fuel cells produce only water as a by-product and their use could substantially reduce greenhouse gas emissions[6].

Although first fuel cell products for off-grid power supply or automotive applications[7] are already commercially available, several issues remain to facilitate their wide spread adoption such as costs and durability. Platinum used as catalyst at the electrodes is the most expensive component in this technology[8]. Much effort has been made to develop adapted carbon based supports to reduce the amount of platinum in a PEMFC. In some PEMFC operating conditions, electrocatalyst supports based on conventional carbon suffer from corrosion, leading to aggregation, migration, detachment or isolation of platinum nanoparticles resulting in a loss of performance[6]. To overcome this limitation, the strategy adopted in the work described in this thesis is to associate an alternative composition with different morphologies and elaborate novel catalyst supports for PEMFC cathodes.

Three different synthesis routes for the elaboration of niobium carbide electrocatalyst supports leading to three different morphologies have been developed: nanostructured powders, nanofibres and nanotubes. After a presentation of the principle of fuel cells, and remaining challenges related to

PEMFC, the state of the art concerning metal electrocatalyst supports will be described. Special attention is given to 1D nanostructured supports. The three following chapters will be dedicated to a description of the synthesis and characterisation of the catalysed supports prepared in this work. Experimental techniques recurrent within the different chapters will be detailed in the Experimental Annex.

The research described in this thesis received financial support from Johnson Matthey Fuel Cells and the CNRS (CNRS Bourse de Doctorat pour Ingénieur). It was carried out at ICGM-AIME (Institute Charles Gerhardt of Montpellier; research group: Aggregates, Interfaces and Materials for Energy). Part of the characterisation was performed in the Technical Centre of Johnson Matthey Fuel Cells at Sonning Common, UK.

Chapter 1: Context and motivation

A. Introduction

1. Fuel cells

Fuel cells are energy converters generating electricity through electrochemical processes. Supported by the work of Christian Friedrich Schönbein (1799 – 1868) related to water electrolysis, William Robert Grove (1811 – 1896) demonstrated the fuel cell principle in 1839[9]: this device converted the chemical energy provided by the inverse reaction of water electrolysis **(1)** into electrical energy.

$$H_2 + \frac{1}{2}\, O_2 \;\rightarrow\; H_2O + \text{Heat and energy} \quad \textbf{(1)}$$

This system used pure gaseous hydrogen and oxygen and sulphuric acid as electrolyte. The reactions were catalysed by a porous platinum electrode. The interest for fuel cells dwindled and was renewed only in the early 1960s, when Bacon and al. substituted the acidic electrolyte by potassium hydroxide and built the first Alkaline Fuel Cell (AFC) that was then improved by Pratt and al. by reducing the weight and enhancing the durability. This technology was used by the NASA in the GEMINI (1963) and APOLLO programmes (1968)[10]. In 2015 the first commercially available hybrid hydrogen fuel cell car, the Toyota Mirai, is being sold in Japan and the USA[11].

In a fuel cell, chemical energy is converted into electricity without any combustion process. Thus its efficiency is not thermodynamically limited by the Carnot cycle. Moreover the theoretical efficiency of a fuel cell can be up to 90 % if the heat produced is captured and used in a cogeneration system. Fuel cells are generally between 40–60 % energy efficient which is far above the maximum thermal efficiency (25 % to 30 %) of a combustion engine[12,13]. As long as they are supplied with fuel, fuel cells can, in principle, deliver electricity continuously, unlike batteries where the number of charge carriers at the negative electrode, for example, is finite.

Despite these advantages, fuel cell technology suffers some limitations that need to be overcome, mainly their high cost and poor durability. Much effort has been devoted to decrease the amount of precious metal electrocatalyst for the oxygen reduction reaction (ORR) and to extend fuel cell durability by understanding the mechanisms by which materials components age prematurely, and the fuel cell operation conditions under which different ageing mechanisms predominate. The research described in this thesis is aligned with this momentum.

There are several fuel cell types, including proton exchange membrane fuel cells (PEMFC), alkaline fuel cells (AFC), direct alcohol fuel cells (DAFC) including direct methanol and direct ethanol fuel cells

(DMFC, DEFC), phosphoric acid fuel cells (PAFC), high temperature PEMFC (HT-PEMFC), molten carbonate fuel cells (MCFC), proton ceramic fuel cells (PCFC) and solid oxide fuel cells (SOFC). They are commonly classified according to the type of electrolyte, which to a large extent defines the temperature range of operation and thus fuel type and electrocatalysts[14,15]. Figure 1 and 2 schematically depict the operating conditions for the various types of fuel cell[16].

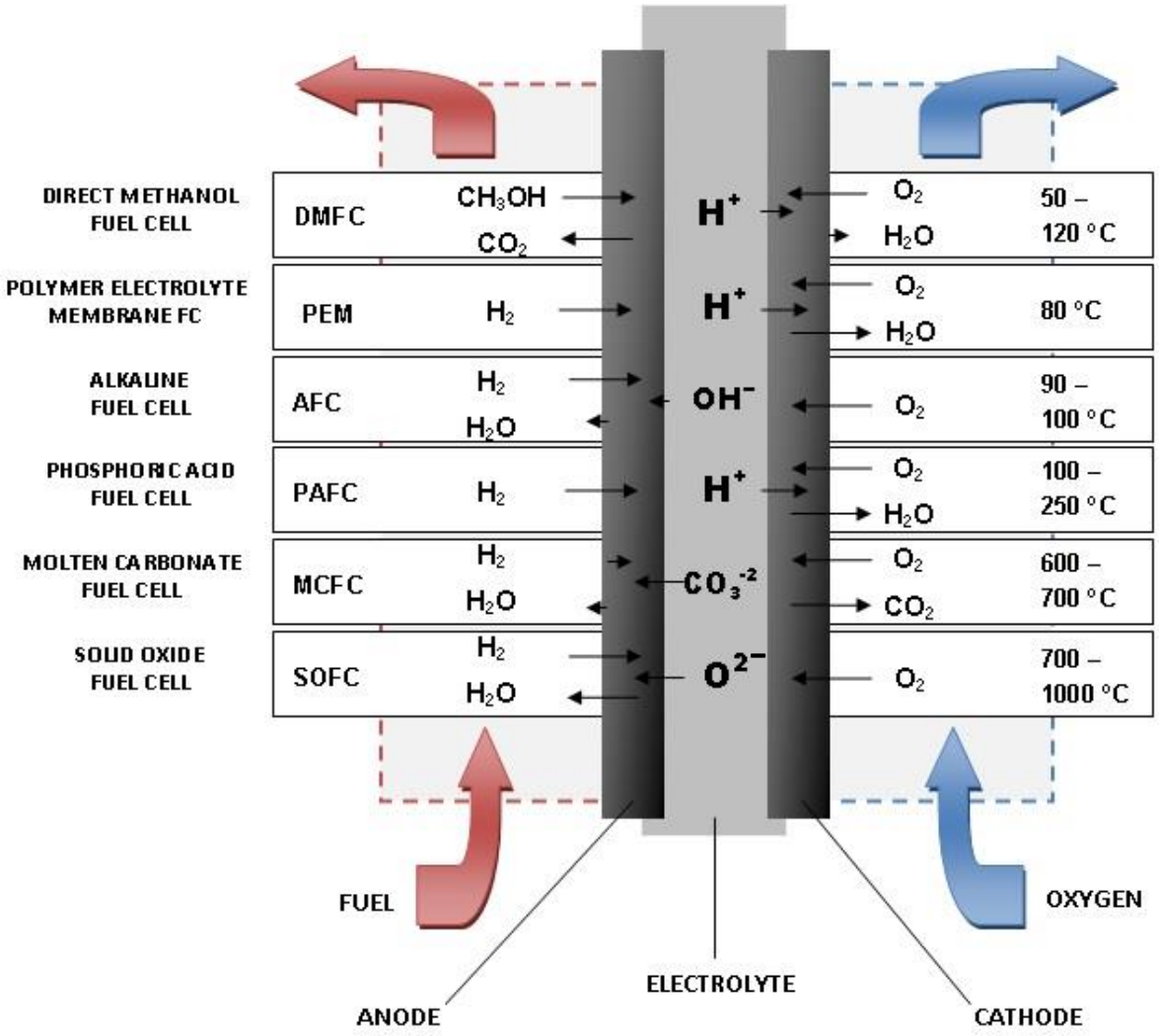

Figure 1. Specifications of the different fuel cells types (electrolyte, fuel and operating temperature range)[17].

Typical applications	**Portable electronics equipment**	**Cars, Boats, and domestic CHP**	**Distributed power generation, CHP, Buses**
Power (Watt)	**1 - 100**	**1 k - 10 k**	**1 M - 10 M**
Main Advantages	**Higher energy density than batteries and faster recharging**	**Potential for zero emissions High efficiency**	**High efficiency less pollution quiet**
Range of application	Direct Methanol FC Alkaline FC Molten Carbonate FC Solid Oxide FC Proton Exchange Membrane FC Phosphoric Acid FC		

Figure 2. Chart summarising the applications and characteristics of the various types of fuel cell[18].

2. Proton exchange membrane fuel cells (PEMFC)

Proton exchange membrane fuel cells (PEMFC) operate at low temperature (typically 80 °C) with a functionalised polymer membrane as electrolyte[19]. Their high power densities and electrical efficiency (40 – 60 %)[17] are well suited to applications where quick start-up is required, such as automobiles. This technology is for example used in the Toyota Mirai[11], the hydrogen fuel cell car. Other major manufacturers (Hyundai[20], Honda[21]) plan fuel cell passenger vehicle commercialisation in the near future[7]. Today PEMFC systems are commercialised for a variety of fields and applications such as telecommunications, data centre and residential markets (primary or backup power), and to power forklifts and other material handling vehicles.

i. Thermodynamics

The Hydrogen Oxidation Reaction (HOR) (2) takes place at the anode where electrons and protons are released and transferred to the cathode, where the Oxygen Reduction Reaction (ORR) takes place leading to water (3).

$$H_2 \rightarrow 2H^+ + 2e^- \quad \textbf{(2)} \; E°_{anode} = 0 \text{ V / SHE (HOR)}$$

$$½\, O_2 + 2e^- + 2H^+ \rightarrow H_2O \; \textbf{(3)} \; E°_{cathode} = 1.23 \text{ V / SHE (ORR)}$$

Electrons are transferred through an external circuit while protons pass through the membrane from anode to cathode, Figure 3.

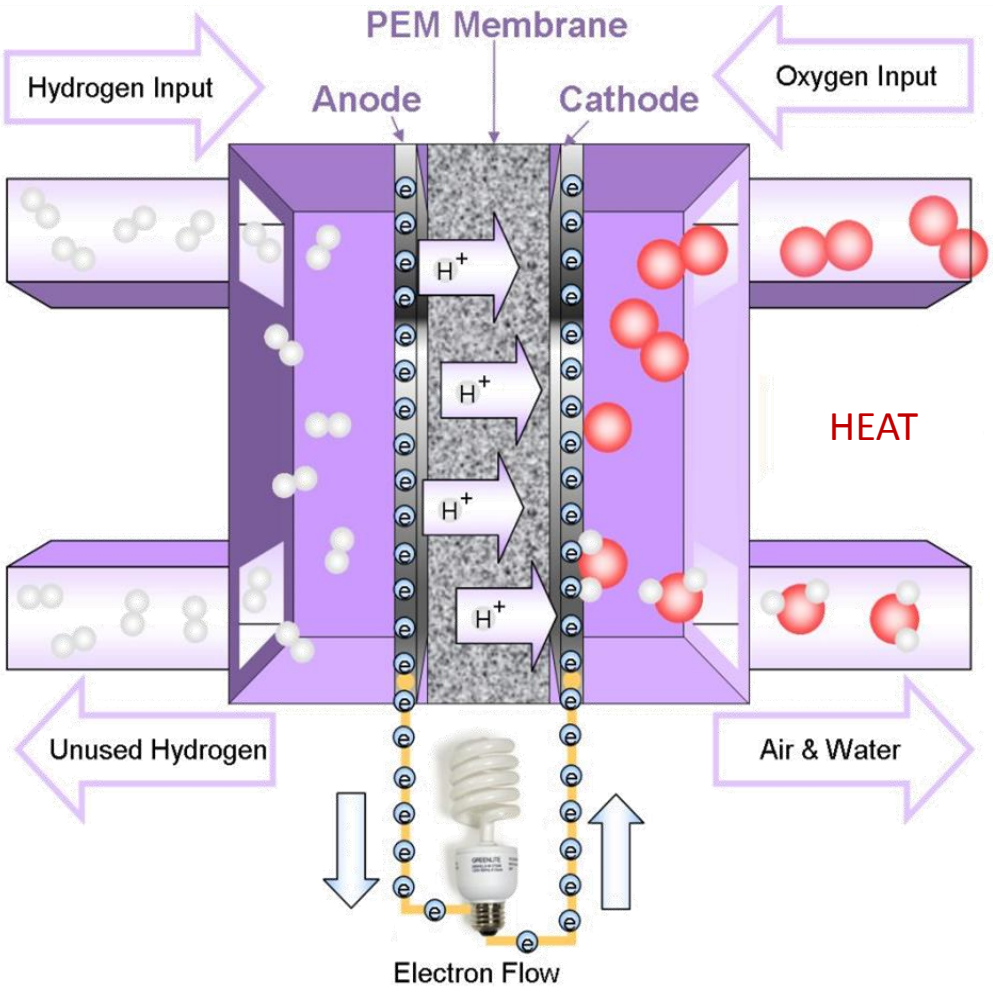

Figure 3. Schematic diagram of the principle of PEMFC operation.

Therefore the balanced overall reaction that occurs between fuel and oxidant (1) in a fuel cell is the reaction of formation of water from oxygen and hydrogen. Thermodynamically this reaction is exothermic which implies a production of heat by the system. The electrical energy released by the reactions and that can potentially be developed by the proton exchange membrane fuel cell can be quantified by the Gibbs free energy (ΔG°) of the global chemical reaction (1). This energy is expressed per mole, and matches the formation of one mole of liquid water (4).

$$\Delta G^{0}_{H_2O\,(l)} = -228.2\ kJ\,.mol^{-1}\ at\ 80\ °C \quad \textbf{(4)}$$

The Gibbs free energy under standard conditions for thermodynamic equilibrium allows defining the electromotive force or reversible open circuit voltage (5): ΔE^{0}_{eq} .

This voltage would be ideally obtained if all the chemical energy were converted to electrical energy.

$$\Delta E^{0}_{eq} = -\frac{\Delta G^{0}_{H_2O\,(l)}}{n\,F} \quad \textbf{(5)}$$

F is the Faraday constant (96,485 C· mol^{-1})

n is the number of exchanged electrons during the reaction

At 25 °C the calculated open circuit voltage (OCV) of PEMFC is 1.23 V (1.18 V at 80 °C).

Practically, the balance of the process includes the heat and the electricity produced during the reaction (1).

$$H_2 + ½\ O_2 \rightarrow H_2O + \text{Heat} + \text{Electricity} \quad \textbf{(1)}$$

And the maximum efficiency allowed by thermodynamic laws $\xi_{fuel\ cell}$ is the ratio of the maximum available work energy over the total chemical available energy within the fuel cell:

$$\xi_{fuel\ cell} = \frac{\Delta G^{R1}_{H_2O\,(l)}}{\Delta H^{R1}_{H2O\,(l)}} \quad \textbf{(7)}$$

For a PEMFC at 25 °C, at atmospheric pressure (P_{O2} and P_{H2} = 1 bar), the thermodynamic fuel cell maximum efficiency, ξ, is 83 %.

ii. Kinetics

Despite the thermodynamic forecasts, some remaining energy barrier needs to be overcome. In PEMFC operating temperature (80 °C) this activation energy is required to increase the rates of hydrogen oxidation and oxygen reduction reactions taking place at the anode and the cathode sides, respectively. Thus for both reactions the use of a suitable electrocatalyst is essential.

Hydrogen Oxidation Reaction

$$H_2 \rightarrow 2H^+ + 2e^- \quad \textbf{(2)}$$

The mechanism of hydrogen oxidation at the PEMFC anode (2) involves different steps matching the adsorption of hydrogen onto a catalyst surface such as platinum with the hydrogen molecule dissociation into single atoms (Tafel reaction, 8) and the release of one proton and one electron (Volmer reaction, 9)[22].

$$\text{Tafel reaction: } H_2 \rightarrow H_{ad} + H_{ad} \textbf{ (8)}$$

$$\text{Volmer reaction: } H_{ad} \rightarrow H^+ + e^- \textbf{ (9)}$$

There is a contribution of an alternative pathway at high overpotential. For this mechanism, the dissociation of the H_2 molecule takes place during the first step producing a proton and an electron (Heyrovski reaction), 10. The remaining absorbed hydrogen is released as one proton and one electron in a second step via the Volmer reaction(11)[23].

$$\text{Heyrovsky reaction: } H_2 \rightarrow H_{ad} + H^+ + e^- \textbf{ (10)}$$

$$\text{Volmer reaction: } H_{ad} \rightarrow H^+ + e^- \textbf{ (11)}$$

Oxygen Reduction Reaction

The ORR is kinetically limiting (10^6 slower than HOR)[24] and understanding its mechanism is essential. The one usually described in literature[25] is a direct 4-electron reduction of oxygen to water in acidic medium (3).

$$O_2 + 4H^+ + 4e^- \rightarrow 2H_2O \quad E_0 = 1.23 \text{ V} \textbf{ (3b)}$$

A second pathway via the formation of hydrogen peroxide in a 2-step mechanism is also possible: hydrogen peroxide formed during the first step by the 2-electron reduction of oxygen (12a) is consumed in a second 2-electron step leading to the formation of water (12b).

$$O_2 + 2H^+ + 2e^- \rightarrow 2\ H_2O_2 \quad E_0 = 0.67 \text{ V} \textbf{ (12a)}$$

$$2H_2O_2 + 2H^+ + 2e^- \rightarrow H_2O \textbf{ (12b)}$$

The presence of H_2O_2 was revealed by rotating ring disk electrode (RRDE) as a proof of a contribution/competition of the 2 step pathway[26]. Currently platinum nanoparticles supported on carbon (Pt/C) are the most commonly used ORR electrocatalysts. In this case, the measured hydrogen peroxide amount is negligible in operating fuel cell voltage (0.6 – 1.0 vs RHE)[24], indicating that the main mechanism on platinum is the direct 4-electron path. Any presence of hydrogen peroxide is important since it can lead to the formation of hydroxyl radicals ($HO^{\cdot}$) that can lead to membrane and carbon support degradation. Moreover, the direct 4-electron mechanism is more energetically efficient and is preferable in the case of PEMFC.

According to experimental and theoretical studies such as Density Functional Theory (DFT), two more detailed mechanisms in the presence of platinum were proposed[27].

The dissociative mechanism (13) leads to the $4e^-$ pathways. Oxygen is first adsorbed onto the platinum active sites and reduced by reacting with the proton coming from the anode through the membrane in a second step. Water is finally released out of the active sites in the last step.

$$\tfrac{1}{2}\ O_2 + * \rightarrow O* \textbf{ (13a)}$$

$$O* + H^+ + e^- \rightarrow OH* \textbf{ (13b)}$$

$$OH* + H^+ + e^- \rightarrow H_2O \textbf{ (13c)}$$

At higher current density the associative mechanism may occur, leading to the $2e^-$ pathway. In this mechanism, the oxygen bound may not be broken resulting in the formation of hydrogen peroxide (14d).

$$O_2 + * \rightarrow O_2* \textbf{ (14a)}$$

$$O_2* + H^+ + e^- \rightarrow HO_2* \textbf{(14b)}$$

$$HO_2* + H^+ + e^- \rightarrow H_2O + O* \textbf{ (14c)}$$

$$(\text{or } HO_2* + H^+ + e^- \rightarrow H_2O_2 + *) \textbf{ (14d)}$$

$$O* + H^+ + e^- \rightarrow OH* \textbf{ (14e)}$$

$$OH* + H+ + e \rightarrow H_2O + * \textbf{ (14f)}$$

Several models have been suggested for the oxygen adsorption onto platinum active sites such as Griffiths (15a), Yeager (15b) or Pauling models (15c)[28] (Figure 4). In the first model (15a) the O_2 molecule interacts with two bonds on a single platinum active site. In (15c) the O_2 molecule as a

bridge between two different platinum active sites is absorbed with two bonds. In (15b) O_2 is adsorbed on a single platinum active site with a single bond.

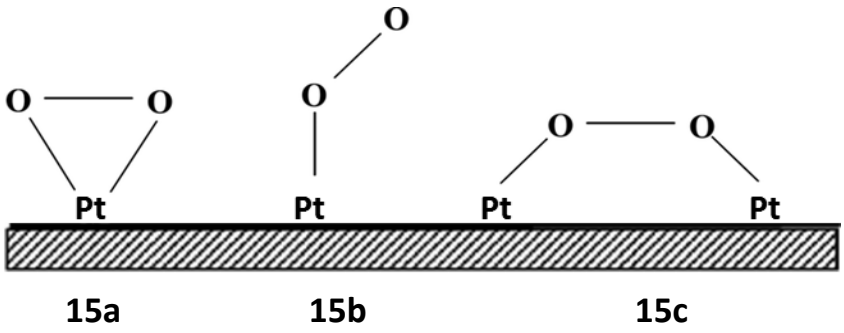

Figure 4. Griffiths (15a), Yeager (15b) and Pauling (15c) adsorption models.

Given the theoretical calculations, the Yeager model benefits more stable adsorption conditions than the two other models. In contrast to the Griffiths and Yeager model that lead to the formation of water only, the Pauling model explains the possible presence of hydrogen peroxide.

The high efficiency of platinum as electrocatalyst for the ORR in comparison to other precious metals can be explained by the Sabatier principle. The platinum - oxygen binding energy must be strong enough to promote the adsorption of oxygen onto the metal surface, and weak enough to allow the release of a water molecule and free an active site at the same time. This argument can be illustrated by the volcano plot in Figure 5, that displays the activities of different transition metals as a function of the oxygen binding energy (calculated by DFT)[29,30]. For species located on the right hand side of the diagram such as Ag or Au the binding energy with oxygen would be too weak and the adsorption would become too slow to maximise the reaction rate. Species located on the left hand side such as Ni or Pd would be adsorbed too strongly resulting in electrocatalyst active site blockage.

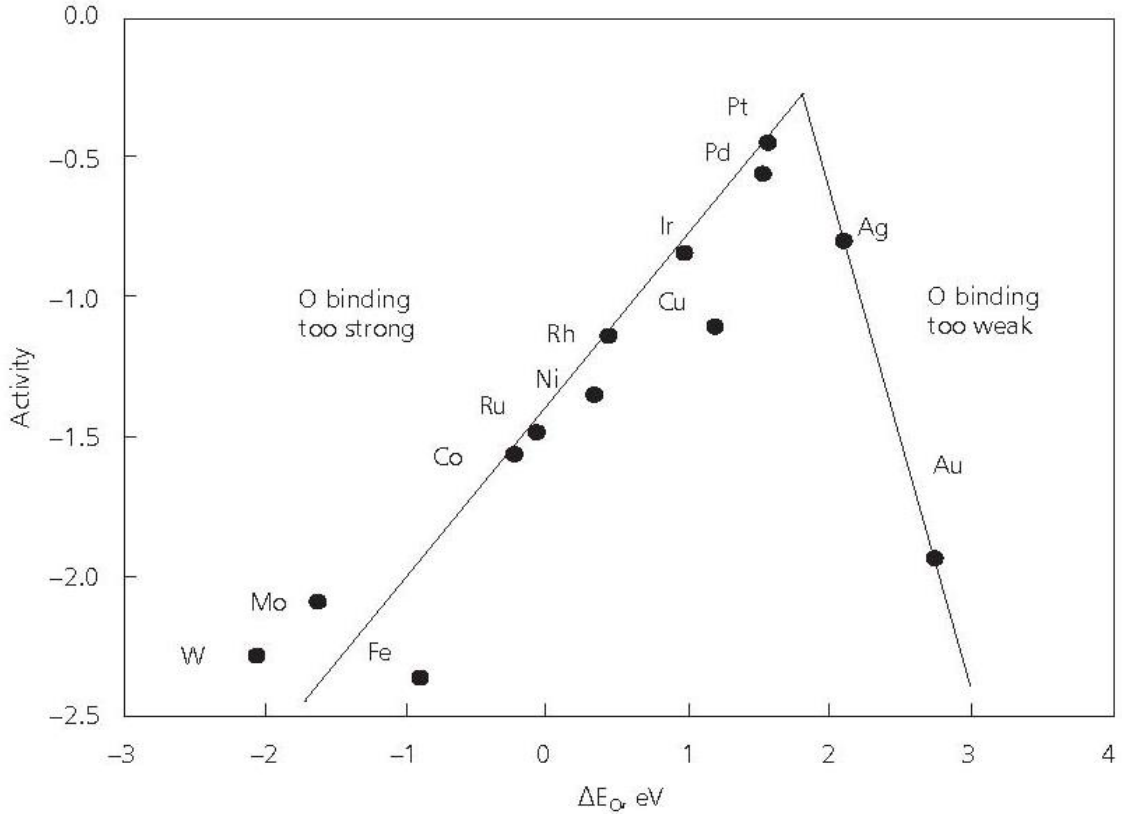

Figure 5. Volcano plot of precious metal for the oxygen reduction reaction[22].

The rate of an electrochemical reaction is usually described by the electrical current related to the charge and the consumption of the reactant and can be expressed using the Faraday's law (16a). In this equation the reaction is defined as the difference between the forward and backward reaction on the electrode.

$$i = nF\,(k_f C_{ox} - K_b C_{red}) \quad \textbf{(16a)}$$

nF : transferred charge (C)
C_{ox} and C_{red} : concentration of the reacting species at the surface of the electrode (mol · cm^{-2})
k_f, k_b : the constant of the forward and backward reaction, respectively

At the equilibrium, current is equal to zero, which means that both reactions proceed in opposite directions with the same rate. The exchange current density is defined as the current contribution matching the rate at which the forward and backward reaction occur (16b). i_0 rises with the reaction rate: for instance it is 6 orders of magnitude higher for the HOR than for the ORR.

$$i_0 = nF\,k_f C_{ox} = nF\,K_b C_{red} \quad \textbf{(16b)}$$

Given the Arrhenius equation, the rate constants can be expressed as a function of the temperature and the activation energy, that the charge must overcome to move from the electrolyte to the electrode (16c).

$$k = A \exp^{(-Ea/RT)} \quad \textbf{(16c)}$$

The electrochemical term of the energy activation is proportional to the voltage E (V), the transferred charge nF (C) and the transfer coefficient α (theoretically between 0 and 1 and usually equal to 0.5) (16d).

$$k = k_0 \exp^{(-\alpha nFE/RT)} \quad \textbf{(16d)}$$

The equation (16e) obtained from equation (16a), (16b) and (16d) is called the Butler-Volmer equation and delineates the relationship between current and potential.

$$i = i_0 [\exp^{(-\alpha nF\eta/RT)} - \exp^{(-(1-\alpha)nF\eta/RT)}] \quad \textbf{(16e)}$$

i: effective current (A)

i_0: exchange current (A)

α: transfer coefficient

n: number of transferred electron

F: Faraday's constant = 96,485 $C \cdot mol^{-1}$

η: overpotential (V) is the difference between the potential of the cathode and the equilibrium potential of the reaction

R: universal gas constant = 8.31 $J \cdot K^{-1} \cdot mol^{-1}$

T: temperature (K)

In the case of PEMFC at high overpotential, the term corresponding to the anodic reaction is negligible in comparison with the term corresponding to the cathodic reaction and the equation (16e) can be simplified to (17) and furthermore to the so-called Tafel equation (17b).

$$i = i_0 \left[\exp^{\left(\frac{-\alpha nF}{RT}\eta\right)}\right] \quad \textbf{(17)}$$

$$\log(i) = \log(i_0) + \left(\frac{-\alpha nF}{2.3RT}\eta\right) \quad \textbf{(17a)}$$

$$\eta = \left(\frac{2.3\mathrm{RT}}{\alpha \mathrm{nF}}\right)\log(i_0) + \left(\frac{2.3\mathrm{RT}}{\alpha \mathrm{nF}}\right)\log(i) = a + b\log(i) \quad \textbf{(17b)}$$

The Tafel plot displays the overpotential as a linear function of log(i). In the case of the ORR at the PEMFC cathode, two Tafel slopes are often reported in the literature depending on the current density[31]. The change in Tafel slope is attributed to the change in the nature of the adsorbed oxygen-containing species with potential, a transition that strongly affects the ORR[32]. In acidic media, typical slopes around 60 mV dec^{-1} for low overpotential and 120 mV $\cdot dec^{-1}$ for high overpotential are reported for Pt[29]. Tafel slope values highlight information on ORR electrocatalysis mechanism. In the case of platinum, the Tafel curve can be affected by several parameters such as a change in the physical structure of Pt (Pt–Pt bond distance and coordination number), adsorption of oxygen-containing species from the electrolyte onto the Pt, redox type processes[33].

3. Components of membrane electrode assemblies of PEMFC

The membrane electrode assembly (MEA) consists of two electrodes in contact with the ionomer membrane (Figure 6). These different components are shortly described in the following section.

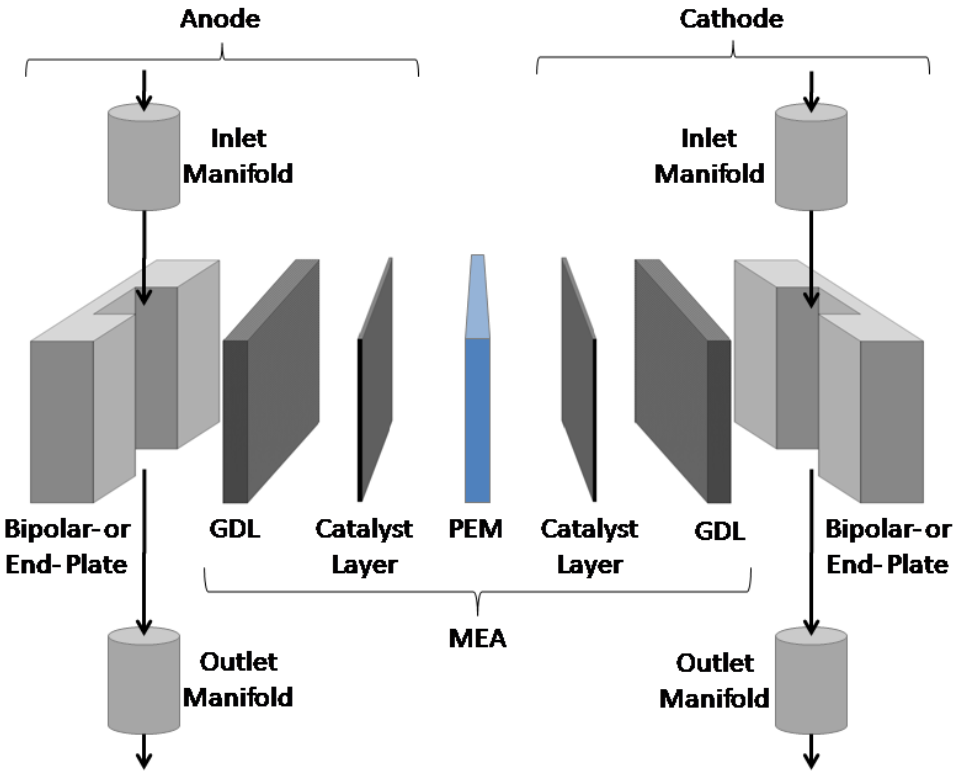

Figure 6. Exploded-view drawing of fuel cell components.

i. Electrodes

The two electrodes include the same components, a gas diffusion layer (GDL), a catalyst layer and an optional microporous layer. Concerning the preparation, the catalyst layer can be deposited on the GDL and form a gas diffusion electrode (GDE) or directly applied to the membrane (catalyst coated membrane, CCM). The MEA is usually hot pressed to develop appropriate interface between catalyst layer and membrane.

Gas diffusion layer

The gas diffusion layer stands at the interface between catalytic layer and the bipolar plate and allows distribution of the gas to the catalyst layer by diffusion. It is usually made of carbon cloth or carbon fibre papers. Its main role is to provide the gas accessibility to the catalytic layer, but its design and composition[34] optimisation also improve the water management in the electrode which is vital to ensure the high performance and long life of the fuel cell[35].

Catalyst layer

In a conventional PEMFC, the catalyst layer is made of platinum (or platinum alloy) particles supported on carbon black, the high surface area and suitable porosity of which allow a good dispersion of the electrocatalyst. Catalysed carbon black set a reference as electrocatalyst however insufficient electrochemical stability at high potential results in poor durability that justifies the development of alternative supports. The elaboration of alternative to carbon-based supports is the main objective of the work described in this PhD thesis, and their required properties will be detailed in paragraph A.4. The catalyst layer is where electrochemical reactions take place. The catalysis that takes place on both PEMFC electrodes is heterogeneous since it occurs between the gaseous fuel and the solid catalyst. Therefore the reactions (HOR and ORR) can only occur at confined spatial sites, called “triple phase boundaries” (TPB) where electrolyte, gas, and electrically connected catalyst regions contact[37]. Nafion electrolyte is conventionally used as a binder and as an ionic conductor to improve the three-phase boundary sites where the catalytically active electrode particles, electrolyte phase and gas pores intersect. (Figure 7a and 7b).

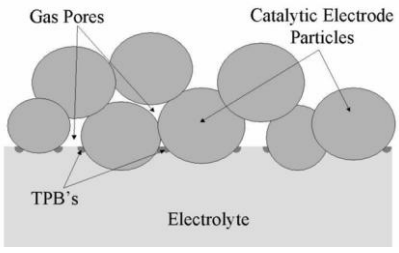

Figure 7a. Electrode-electrolyte interface illustrating the triple phase boundary reaction zones[36].

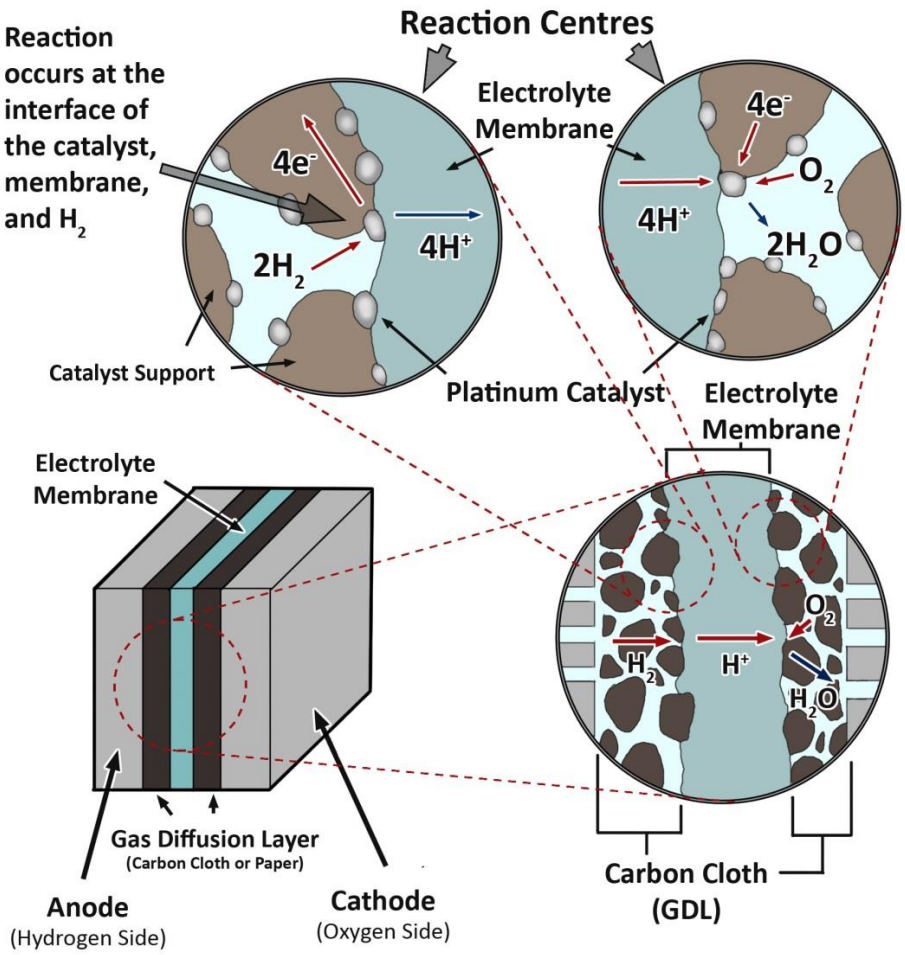

Figure 7b. ORR and HOR reaction centres in the electrode in MEA[38].

ii. Membrane

The electrolyte membrane is responsible for the proton transfer from the anode to the cathode. An efficient membrane must not conduct electrons and prevent direct gas crossover. Its mechanical strength and chemical stability are key points for the durability of the PEMFC[39].

State of the art membranes are perfluorosulfonic acid (PFSA) polymers, typified by Nafion (Figure 8). This is a long-side-chain PFSA, where side groups from the polytetrafluoroethylene backbone terminate in sulfonic acid groups that provide the protons responsible for membrane proton conductivity.

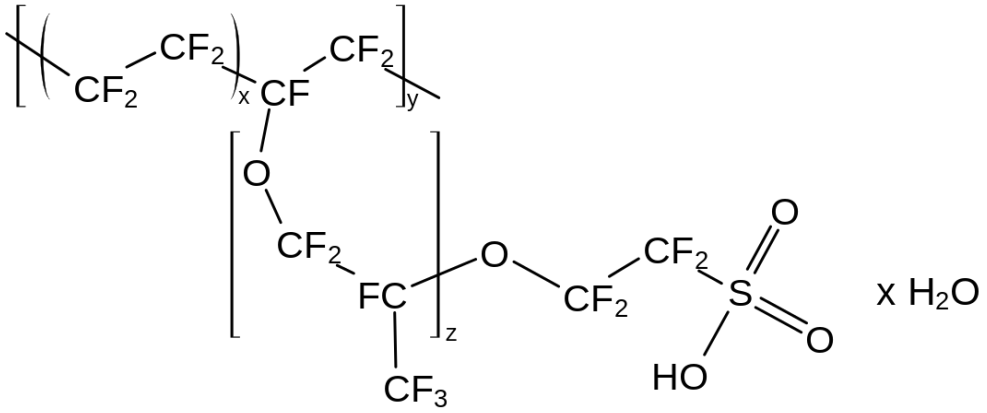

Figure 8. Nafion chemical structure.

4. Challenges and motivation

The identification of the major remaining challenges in PEMFC developments highlights the importance of a suitable electrocatalyst support for PEMFC electrodes. Currently most of the developed PEMFC employ carbon-based electrocatalyst supports, especially carbon black (Vulcan XC72, Black Pearls or Ketjenblack) because of their large surface area, their high electrical conductivity and their well-developed pores[40,41]. However, these supports suffer from carbon corrosion that leads to a loss of performance. The kinetics of carbon corrosion is significantly increased for potentials greater than 1.2 V, while in normal operating PEMFC voltages (0.6 - 0.9 V) the rate of this reaction is negligible. The presence of oxygen on both anode and cathode due to leakage from outside air or crossover implies the coexistence of H_2 and O_2 in the anode. As a result, O_2 reduction occurs at the anode side. In this situation, protons obtained from carbon oxidation or oxygen evolution promote a reverse current that is a cause of very high potential (up to 1.4 V) leading to carbon corrosion (Figure 9).

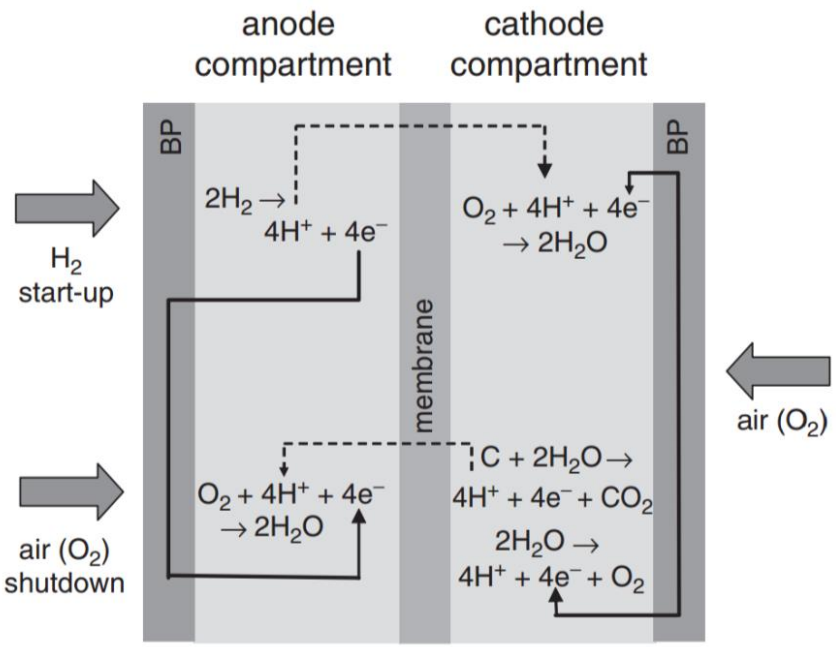

Figure 9. Schematic illustration of electrode reactions occurring for start/stop-induced carbon corrosion in the cathode[42].

The aim of this work was to develop novel materials to replace the carbon-based supports and so improve the durability of the electrodes. The novel catalysed support is required to have similar performance in a fuel cell in terms of power density. Therefore, alternative support materials must be elaborated with properties that will enable them to compete with carbon blacks. These required properties are detailed in the followings parts.

i. High surface area and suitable porosity

The number of active sites must be enhanced to promote oxygen reduction at the cathode. Optimising the active sites number per mass of catalytic layeris essential to decrease the amount of electrocatalyst. In this context a catalytic layer is usually prepared by dispersing the electrocatalyst (platinum particles) onto a support. The quality and homogeneity of the electrocatalyst dispersion significantly depends on the morphology of the support. Its porosity should be controlled to provide pores that are large enough for the electrocatalyst particles and for the gas to reach them. The pore size should be small enough to supply the support with high surface area to support high platinum loading so as to prepare thin electrodes. As references of carbon supports, carbon blacks including Vulcan XC 72 and Ketjenblack respectively feature specific surface area of 250 $m^2 \cdot g^{-1}$ and 780 $m^2 \cdot g^{-1}$ [43].

ii. High electrical conductivity

The electron transfer within the electrodes is directly related to the electronic conductivity of the support. This is consequently a pivotal requirement so that the electron transfer does not become the limiting step for the ORR kinetics. Depending on their crystal structures carbon based materials present a wide range of electrical conductivity. The highest value was measured for graphene (10 – 10^2 $S \cdot cm^{-1}$)[44,45], while that of carbon Vulcan is 0.1 – 10 $S \cdot cm^{-1}$ [46]. It is interesting to note that the electrical conductivity is also related to the grain size and the morphology of the electrocatalyst support.

iii. Electrochemical stability and durability

The benefit of a novel electrocatalyst support will be found in the insufficiency of the currently used carbon blacks in fuel cell operating conditions[47]. One crucial requirement is a high chemical and electrochemical stability to prevent the degradation of the catalyst layer overtime and improve the electrode durability. The cause of the performance loss has been the subject of studies in the past three decades. One remaining issue is the degradation of the carbon-based electrocatalyst support conventionally used in PEMFC electrodes. The corrosion reaction is generalised[48] as (18):

$$C + 2H_2O \rightarrow CO_2 + 4\,H^+ + 4e^- \qquad E° = 0.207\ V \textbf{ (18)}$$

This reaction is reported as a 3-step mechanism that consists of the oxidation of a carbon lattice (19a), the hydrolysis of the formed cation (19b) and the release of carbon dioxide (19c)[49].

$$C \rightarrow C^+ + e^- \textbf{ (19a)}$$

$$C + ½\ H_2O \rightarrow CO + H^+ \textbf{ (19b)}$$

$$CO + H_2O \rightarrow CO_2 + 2H^+ + 2e^- \textbf{ (19c)}$$

This reaction is thermodynamically allowable at the potentials at which the fuel cell cathode operates[50], but it is believed to be almost negligibly slow in the operating condition of PEMFC[51]. However, even if it proceeds very slowly, it can affect the long-term durability of PEMFCs. Furthermore in particular conditions in which hydrogen-rich regions and hydrogen-starved regions coexist in the anode chamber of a single cell, the reverse-current mechanism (previously detailed in paragraph A.4.) has been proposed[52–55], which creates higher potential (up to 1.5 V vs RHE[56]) than the open circuit voltage (OCV) of ca. 1 V usually encountered as the maximum potential. This mechanism is frequent at start-up of the system or during shut-down of the anode chamber[57] (Figure 9). When carbon corrosion occurs (18), the morphology of the support is damaged promoting

the electrocatalyst particles degradation and detachment. The isolated particles do not take part in electrochemical reaction and therefore the catalytic activity within the electrode decreases[58] (Figure 10).

The intrinsic degradation of platinum particles involves two main mechanisms: particle migration and coalescence[59–61] and Pt dissolution and re-deposition leading to electrochemical Ostwald ripening[62]. These mechanisms occur at different potentials (Figure 10). According to a study by Johnson et al.[63] on a Pt electrode during Pt oxidation/reduction at the interface with the electrolyte most of the ECSA loss at low potential is due to Pt dissolution. More precisely, according to Dubau et al.[57] it starts at 0.6 V vs RHE. Myers et al reported that the equilibrium concentration of dissolved Pt was found to increase monotonically from 0.65 to 1.1 V vs RHE and decrease at potentials 1.1 V vs RHE[64]. As was reported by Kinoshita et al. also, the amount of platinum dissolved per cycle was independent of the upper potential limit at potentials > 1.2 V (≈5 $ng \cdot cm^{-2} \cdot cycle^{-1}$)[65].

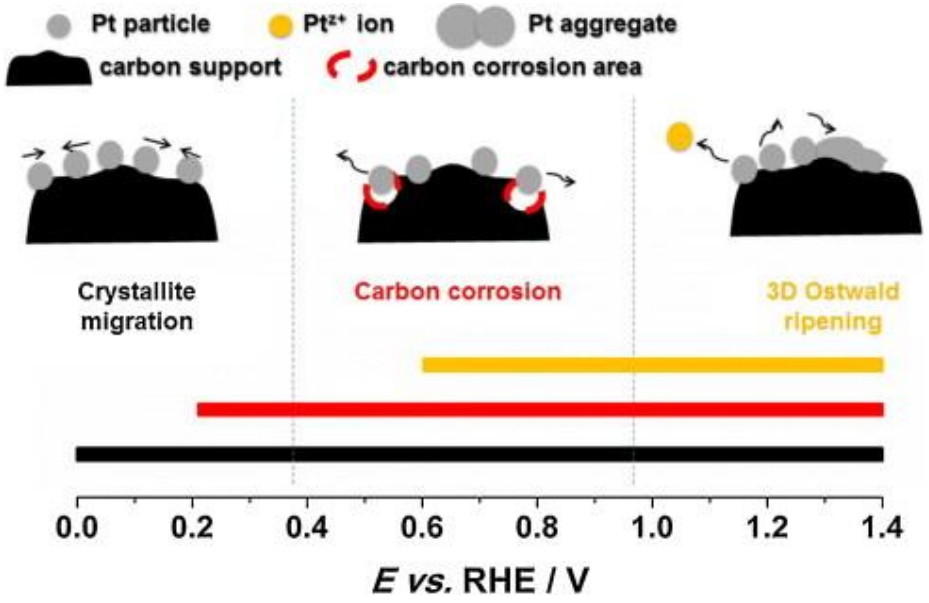

Figure 10. Degradation mechanisms of carbon-supported Pt nanocatalysts[66].

Furthermore by-products of the carbon corrosion such as CO or CO_2 can poison the electrocatalyst surface by blocking the access of hydrogen to active sites[67] (Figure 10). Radical species such as $HO^{\cdot}$ or $HOO^{\cdot}$ have been identified as accelerating agents for the support degradation[68]. Pt can catalyse carbon corrosion leading to the carbon degradation at the interface with Pt preferentially[69].

Exploring non-carbonaceous compositions such as metal oxides or composition without free carbon carbides is a major trend in the development of novel electrocatalyst supports[70].

B. Alternative electrocatalyst support for PEMFC cathodes

A multitude of materials have been investigated for a partial or total replacement of carbon blacks as electrocatalyst support for fuel cells electrodes[69]. This strategy was followed mainly to improve the electrode durability but also to possibly benefit from a promotion of the ORR activity.

1. Metal oxides

Inorganic oxides such as SnO_2, TiO_2, Nb_2O_5, Ta_2O_5, WO_3, and Sb_2O_3 are being considered as alternatives to carbon supports due to their inertness in strong oxidative conditions[69]. Theoretical[71] and experimental studies[72,73] have described their high electrochemical stability in fuel cell operating conditions. Furthermore, metal oxides are known to promote Pt electrocatalysis e.g. by the so-called strong metal support interaction (SMSI). For instance in the case of Pt/TiO_2 the Pt 4f binding energy was decreased compared to Pt/C[74,75]. This SMSI interbonding effect affects the cleavages of intermediates involved in the ORR leading to higher reaction rates.

So far, Pt supported on TiO_2[76–78], WO_3[79,80] and SnO_2[81] showed to be efficient catalysts for the ORR and methanol oxidation reaction (MOR). Nevertheless metal oxides are generally semi-conducting. One of the strategies used to increase their conductivity is the use of doping agents including ionic Nb[82], Ta[83] and Sb[84]. Depending on the oxide, the doping agent is used to add electrons (resulting in a n-type semiconductor) or to increase the number of "holes" (resulting in a p-type semiconductor). The limitation induced by the low electronic conductivity has also been circumvented by increasing the Pt loading on the support so as to decrease the thickness of the catalyst layer[85]. Associated with carbon, the use of metal oxides such as TiO_2 or SnO_2 resulted in further electrical conductivity improvement[86] leading to an ORR activity increase compared to pure oxide support and an enhanced durability compared to carbon based supports.

2. Metal nitrides

Since they are characterised by high electronic conductivity, excellent mechanical stability and corrosion resistance in acidic media, transition metal carbides (TMCs) and nitrides (TMNs) are considered as suitable candidates as electrocatalyst supports. Furthermore some of them show intrinsic electrocatalytic behaviour [70,87]. TiN displays a high MOR activity as well as high CO resistance that was attributed to the synergistic effect between Pt and TiN[88]. Mo_2N, investigated as ORR electrocatalyst, provided a maximum power density of 65 $mW \cdot cm^{-2}$ in single fuel cell[89]. Also ZrN and ZrON have shown electrocatalytic activity featuring a ORR onset potential of 0.7 V vs RHE [90].

3. Metal carbides

Since the use of TMCs is reported not only as supports but also as electrocatalysts themselves, this section is organised into three parts corresponding to the role played by the material in the electrode: Electrocatalyst, Co-catalyst and Electrocatalyst support. Key examples are also summarised in Table 1.

i. Electrocatalysts

In 1963, Mazza and Trasatti first reported that TMCs including WC, TiC, and TaC were active towards the ORR in sulfuric acid[91]. In particular, tungsten carbide featured superior activity than other carbides[92,93] that can be explained by the relation between the catalytic activity and the electronic structure. Indeed, Pt-like behaviour of WC is due to a change in electron distribution of W by the presence of C. Consequently, WC and Pt display a similar valence band structure[94]. This was proven by XPS, showing that the electronic density of WC at the Fermi level is very similar to that of the noble metal[70]. With the development of DFT, the energy of a complex multi-electron system can be determined as a function of the electron density. Using this theory, Norskov et al. have correlated the electronic structure of metal surfaces to their catalytic activity[95], confirming the similarity of tungsten carbide to platinum[94].

In order to benefit from the electrocatalytic activity of carbides, carbide/carbon composites such as SiC/carbide derived carbon or WC with amorphous carbon have been elaborated without further precious metal. In the first example, carbon was formed during the synthesis route[96], whereas in the latter it was used as carbon source to form the carbide[97]. The effect of the addition of carbon on the stability of these composites was not reported.

Research on metal carbides as electrocatalysts has been often extended to nitrides and oxynitrides including TaON and TaN that display an enhanced catalytic activity toward ORR and are obtained by slight modifications of the synthesis parameters[98].

ii. *Co-catalysts*

Due to their electrocatalytic activity TMCs have also been associated with noble metals, and their promoting effect leads to a similar ORR activity, but with lower Pt loadings[99]. For instance, the ORR electrocatalytic activity of a Pt monolayer deposited by ALD on WC was reported to be similar to that of Pt bulk[100]. This result was explained by the oxygen binding energy on WC that was initially almost twice high as on Pt, but that was decreased to that of Pt (111) once one Pt monolayer was added[100]. Following the same strategy, a platinum modified dimolybdenum carbide (Pt/Mo_2C) thin film prepared by a co-impregnation method, demonstrated similar hydrogen evolution reaction activity

as bulk Pt[101]. Another strategy has been the addition of metal carbides to conventional Pt/C supported electrocatalysts to improve their ORR activity. For instance, ZrC was added to Pt/C in order to take advantage of carbon to ensure high specific surface area and of ZrC to promote the ORR catalysis[102]. This example highlights the recurrent need of controlled morphology and porosity to increase the surface area of carbides.

A similar strategy was used on titanium dioxide that was catalysed by a carbide based electrocatalyst (Pt-WC-TiO_2) supported on a bamboo charcoal based support[103,104]. In this case, WC and TiO_2 were both used to protect carbon from corrosion and to assist the electrocatalytic activity of Pt. A double synergistic effect was reported either between Pt and WC (as described above) and Pt and TiO_2 due to strong metal support interaction.

iii. **Electrocatalyst supports**

As it is the most studied carbide and because of its similar electronic structure to platinum, WC was the earliest carbide to be investigated among alternative electrocatalyst supports[69]. Tungsten carbide hollow microspheres as supports for Pt show enhanced electrocatalytic activity towards the ORR[105106], the HER[107], and the MOR[108]. This approach was then extended to other metal carbides. MoC porous nanospheres have been catalysed with Pt particles resulting in high ECSA and MOR and ORR catalytic activity[109]. An enhanced electrochemical stability was reported for this material compared to Pt/C. This support features a high surface area (542 $m^2 \cdot g^{-1}$) mainly due to microporosity (80 %)[109]. Titanium carbide associated with different precious metals (Pt by impregnation[99] or Pt-Ir by a thermal reduction process[110]) shows high ECSA and ORR activity. However, a treatment under hydrogen was required to obtain improved ORR activity compared to Pt/C. Indeed, the formation of a surface oxide layer (reported for instance also for WC) led to a reduction in its electronic conductivity which could affect the catalytic activity of catalysed carbide[111]. The durability over prolonged electrochemical cycles was not investigated for this material. This was a pivotal aspect, however, of the study of Pt/SiC prepared by an impregnation technique using a wood material as carbon source. Accelerated durability tests including cycling (0.6 – 1 V vs RHE) and start/stop testing (1 - 1.5 V vs RHE) showed improved chemical stability compared to a commercial Pt/C but also led to Si leaching[112].

Niobium carbide nanowires synthesised by a carbon thermal method on bamboo, and catalysed with platinum particles, showed high electrochemical stability in accelerated stress tests resulting in 20 % more retained catalyst active surface area than Pt/C, for a comparable initial ECSA (71 $m^2 \cdot g^{-1}$ vs 73 $m^2 \cdot g^{-1}$) and enhanced MOR mass activity (766 $A \cdot g^{-1}$ vs 222 $A \cdot g^{-1}$)[113]. This NbC nanowire support

showed a high electrical conductivity (5.02 $m\Omega \cdot cm^{-1}$) that was attributed to the composition and to the 1D nanostructured morphology. Since continuous morphologies such as fibres imply a decrease of the interface between grains, they are expected to feature a higher electrical conductivity than a less organised material with the same porosity. This illustrates that nanowires are promising supports in terms of electrical conductivity, durability and catalytic activity[93,113].

Table 1. Key examples of transition metal carbides investigated as electrocatalysts, co-catalysts and electrocatalyst supports.

ref	Carbide based electrodes	Electrocatalyst synthesis / deposition	Targeted electrochemical reaction	Main improvement	Main limitation
93	WC nanofibres		ORR	Controlled morphology	Low catalytic activity (carbon at the surface)
96	SiC with carbide derived carbon		ORR	Enhanced durability (-1 V to 0.2 V vs RHE)	Low catalytic activity
97	WC on amorphous carbon		MOR	High surface area 344 $m^2 \cdot g^{-1}$	No stability reported Use carbon (amorphous)
Co-catalyst					
100	WC with Pt monolayer	ALD	ORR	Pt bulk like activity	No stability reported

102	ZrC with Pt particles (dispersed on Vulcan XC 72)	Pt particles by MW assisted polyol process	ORR	Enhanced ECSA and catalytic activity vs Pt/C	Low surface area Carbon-based
103	TiO_2/WC/C with Pt particles	Pt particles by MW assisted polyol process	MOR	Enhanced ECSA and catalytic activity vs Pt/C	No stability reported Use carbon
Support					
107	Hollow microsphere WC with Pt particles	Pt particles by MW assisted polyol process	HER	Enhanced catalytic activity vs Pt/C	No stability reported
105	Hollow microsphere WC with Pt particles	Pt particles by standard polyol process	ORR	Notable surface area for a carbide (64 $m^2 \cdot g^{-1}$) Similar ECSA than Pt/C	Oxide layer formation
106	microsphere WC with Pt particles	Pt particles by pulsed MW assisted polyol process	ORR	High surface area (256 $m^2 \cdot g^{-1}$) Enhanced ECSA and catalytic activity vs Pt/C	No stability reported
99	TiC with Pt particles	impregnation	ORR	Enhanced ECSA and catalytic activity vs Pt/C	- Oxide layer affecting the performance - No stability reported

[114]	TiC nanofibres with Pt particles	-	ORR	Enhanced ECSA and catalytic activity vs Pt/C High surface area (500 $m^2 g^{-1}$)	Use carbon
[114]	TiC nanofibres with Pt particles	urea-assisted ethylene glycol reduction	MOR	Enhanced ECSA and catalytic activity vs Pt/C Electrochemical stability to cycling (93 % ECSA retained vs 88% for Pt/C)	No carbon content investigation
[101]	(Mo_2C Pt modified thin film) Or Pt/MO_2C core shell "powder"	Pt metal impregnation method	HER	Catalytic activity similar to bulk Pt	No stability reported
[109]	MoC 15 nm diameters spheres with Pt particles	Pt particles by MW assisted polyol process	ORR and MOR	Enhanced ECSA and catalytic activity vs Pt/C High surface area (542 $m^2 \cdot g^{-1}$) Electrochemical stability to cycling (93 % retain vs 80% for Pt/C)	High surface area mainly due to microporosity (442 $m^2 \cdot g^{-1}$)

112	SiC with Pt particles	Modified Polyol method	ORR	Improved electrochemical stability (ECSA and catalytic activity)(92 % retained vs 85 % for Pt/C)	Silicon leaching
113	NbC nanowires with Pt particles	Sodium borohydride reduction method	MOR	Similar ECSA and catalytic activity than Pt/C Electrochemical stability to cycling (97 % retained vs 81% for Pt/C)	Possible use of carbon
Other precious metal as electrocatalyst					
110	TiC with Pt/Ir particles	Thermal reduction process	ORR	Enhanced ECSA and catalytic activity vs Pt/C	No stability reported - low surface area ($14\ m^2 \cdot g^{-1}$)
115	WC with Pd particles	Polyol method	MOR	Notable surface area ($42\ m^2 \cdot g^{-1}$) surface area Stability in alkaline media vs Pd/C	Low catalytic activity vs Pt/C
116	Fe/Fe_3C catalysed with PtSn “wire” like morphology	PtSn wire like morphology by polyol (ethylene glycol reduction method)	EOR	Catalytic activity EOR	No stability reported

4. Electrospun materials as electrocatalyst supports

In the context of the preparation of 1D nanostructured materials, electrospinning allows the elaboration of continuous fibres with homogeneous diameters down to the nanoscale opening the way to new properties and consequent applications[117]. This technique is described in further details in the following paragraph.

i. History and principle of electrospinning

The history of electrospinning started in 1902 with the patent of Cooley[118]. Continuous advances in the electrospinning process such as the patent of A. Formhals[119] and comprehension of the involved mechanism reflected by the fundamental work of G. Taylor on electrohydrodynamics[120] led to realisation of its potential as a method for the elaboration of 1D nanomaterials[121]. Electrospinning is conventionally applied to polymers. The polymer solution or melt is injected through a metal needle. A potential is applied between the polymer solution droplet and a grounded target. When the applied electric field overcomes the surface tension of the liquid, the number of charges within the fluid reaches a critical value and the drop deform into the "Taylor cone"[122]. The created electrostatic repulsion stretches the polymer solution into a continuous jet[123]. The solvent evaporates in flight and nanofibres are deposited on the grounded collector (Figure 11). They are collected as a mat with a thickness that can be tuned with the experiment duration.

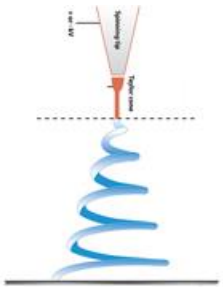

Figure 11. Nanofibres formation by electrospinning.

The electrospinning setup consists of three major components (Figure 12):

- A spinneret (metal needle) containing polymer melts or polymer solutions. The setup can be tuned with a coaxial needle to obtain core shell structures or hollow morphologies such as nanotubes.

- A grounded collector that serves as a counter electrode. The use of a rotating drum collector as grounded target allows a two dimensional mat of homogeneous thickness to be obtained.

- A high voltage power supply.

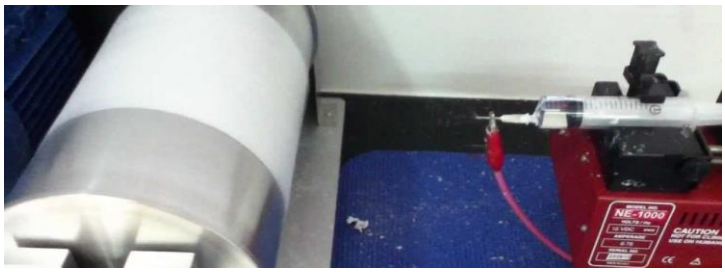

Figure 12. Electrospinning setup with a rotating drum as a target.

Much effort has been devoted in the last decades to the synthesis of nanofibres with different nature and composition widening the range of materials deposited to beyond polymers. To prepare ceramic nanofibres, an inorganic precursor can be spun with the help of a carrier polymer that ensures the required rheological properties[124]. In this case, electrospinning process is coupled with further heat treatments that lead to the targeted composition: calcination in air to remove the organic part or more specific treatments in the presence of reducing atmosphere to achieve different final compositions. Because of these heat treatments and the induced grain growth, the preparation of a self-standing mat with inorganic composition is a remaining challenge. Research to overcome this limitation includes optimisations of the experimental parameters and setup in order to obtain metal oxide nanofibres yarns [125] or flexible ceramic nanobelt networks [126].

The characteristics of the prepared nanofibres depend on several parameters such as the properties of the precursor solution (viscosity, carrier polymer structure and concentration, conductivity), the parameters of the electrospinning setup (applied voltage and distance between needle and target) but also ambient conditions (temperature, humidity)[122,127].

ii. Electrospun materials in PEMFC cathodes

The different suitable compositions for alternative electrocatalyst supports reviewed in the state of the art have been associated with electrospinning. One dimensional electrocatalysts or supports for PEMFC cathodes based on carbon, metal oxides, and more recently transition metal carbides have been prepared. This paragraph gives an overview of the developments in this area.

Carbon nanowires have been prepared by carbonising electrospun polyacrylonitrile (PAN) or polybenzimidazole (PBI). They present advantages over conventional commercial carbon nanoparticle catalyst supports including better stability to corrosion[49], efficient electrocatalyst dispersion[128,129] and adapted porosity for the catalyst layer[130,131].

Electrospinning of metal oxides has also been explored for fuel cell cathode applications[132]. For instance, TiO_2 doped with niobium or treated under reducing atmosphere and catalysed with platinum particles showed high stability and ORR electrocatalytic activity[78,133,134]. Electrospun SnO_2 nanofibres also showed good durability and displayed excellent performance as anode for the HOR[135] or as cathode when doped with Nb[82] and Sb[84].

Few studies report the preparation of non-supported electrocatalysts as pure or alloyed noble metal nanowires[136]. In terms of durability, Pt/Fe nanowires were reported to display enhanced electrochemical stability compared to Pt/C in addition to high catalytic activity towards the ORR[137]. Other bimetallic alloys have been developed for anodic reactions such as Pt/Rh and Pt/Ru for MOR featuring better performance than Pt/C[138]. The difficulty in elaborating fibres with very thin diameters is a challenge for the preparation of 1D nanostructured electrocatalysts with an optimised ECSA.

Metal carbides are prepared by electrospinning, calcination and a final carburation step (Figure 13). For instance, WC nanofibres have been prepared by electrospinning of ammonium metatungstate (AMT) and polyvinylpyrrolidone (PVP) followed by calcination and carburation as electrocatalyst for the ORR in alkaline medium[93].

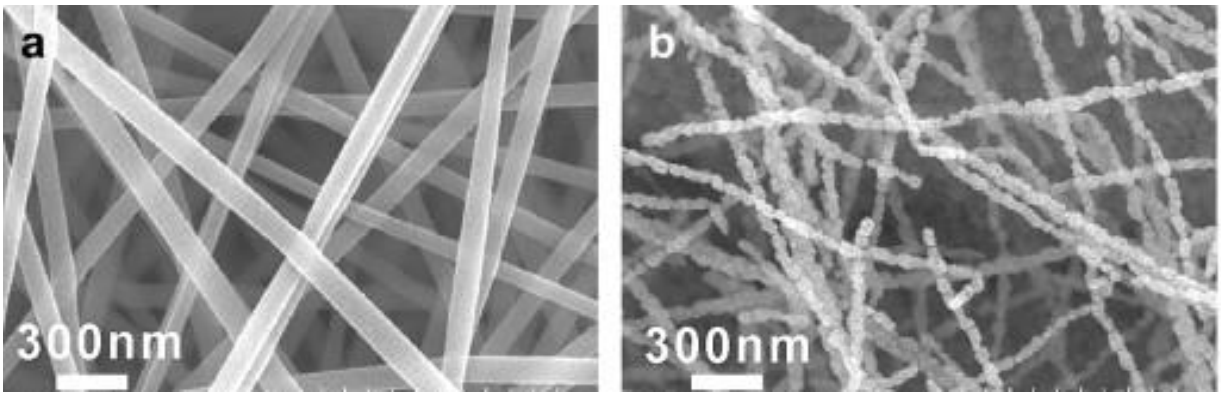

Figure 13. SEM images of (a) as-spun AMT–PVP composite nanofibres, (b) WC [93]

Chromium carbide and nitride have been prepared by electrospinning and a direct carburation using the carrier polymer (PAN) as the carbon source. The obtained nanofibres were active toward the ORR catalysis. The intrinsic catalytic activity was poor probably because of the low chromium content in the fibres. Several synthesis routes based on electrospinning led to niobium based nanofibres (Nb_2O[139,140] or Nb_2O_5/NbC[141]), but none of them have been investigated as electrocatalyst support.

C. Synthesis and deposition of Pt electrocatalysts

Several chemical and electrochemical methods can be used for the synthesis and deposition of a metal catalyst on the support. The most common are described here, including impregnation, colloid methods ("Bönnemann" method, microemulsion and polyol)[142] and electrodeposition.

1. Pt nanoparticles

i. Impregnation method

In the impregnation method, the Pt salt (for example H_2PtCl_6) is reduced directly onto the support either under a flow of H_2 at around 300 °C or by using a reducing agent[143]. It is a very simple method, which allows obtaining a good dispersion on the support with very small Pt nanoparticle size of around 2 nm. One of the advantages of this method is the deposition of the Pt nanoparticles within the pore structure of the support. The disadvantage of this method is the very poor Pt loading, between 1 and 10 $\%_{wt}$, which is too low for PEMFC cathode application. The attempt to increase the metal loading on the carbon support leads to a less homogeneous distribution of the particle size.

ii. Colloid methods

Since the impregnation method does not provide the control of Pt particle size and distribution colloid methods were developed[144]. They consist on the reduction of platinum salt in solution, followed by the adsorption of the Pt ions onto the support. Stabilising agents and surfactants allow an efficient control of the metal nanoparticle size and prevent their agglomeration[145]. Ethylene glycol is a suitable stabilising agent because it can be easily removed from the catalyst surface by a heat treatment at 160 °C[146]. However regarding the low concentration of the metal particles, the colloidal method requires a large amount of solvent that would be a disadvantage for up-scaled production.

In the so-called Bönnemann method, tetraalkylammonium salt acts as both the reducing agent and the stabilising agent. It was used for the elaboration of Pt and Pt alloys particles in tetrahydrofuran (THF). For example, PtRu and Pt_3Sn particles were obtained with a very narrow particle size distribution (2 nm diameter). Unlike ethylene glycol, this surfactant needs to be removed by calcination at 300 °C which can damage the catalyst structure[147].

The use of nanoreactors in a microemulsion is another possibility to control nucleation and growth of metallic nanoparticles in order to obtain narrow size distributions. The surfactant acts as a separator between the non-polar solvent and the water droplets in which the reduction of the metal salt occurs[148].

In the polyol method[149,150] ethylene glycol plays the role of solvent, reducing agent and stabilising agent. The latter is oxidized to aldehydes, carboxylic acid and CO_2 and the platinum salt reduced to metallic platinum. At high pH the glycolic acid groups dissociate into glycolate groups which stabilise the platinum colloid by forming chelate-type complexes[151]. This mechanism of stabilisation allows controlling the particles size with the concentration of glycolate and thus with the pH of the solution. The higher is the pH the higher the concentration of glycolate and the smaller is the Pt particle size. Other parameters such as precursor salt concentration, temperature and time of the reaction have also major influence on the particles diameter. The usual reflux at 160 ° C for 3 h leads to 2 – 4 nm particles for an initial pH set above 11[152]. This platinum particle diameter is close to the optimal size for the ORR catalysis in acidic medium. Sattler and Ross[153] and Peuckert[154] have found a maximum efficiency for 3.5 nm particles diameter (matching a mass activity of 40 $A \cdot g^{-1}$ at 0.9 V vs RHE for an ECSA of 80 $m^2 \cdot g^{-1}_{Pt}$ in phosphoric acid)[153]. They attributed it to the surface structure of smaller particles[155]. However, other investigations performed by Takasu[156] highlighted a plateau in electrocatalytic activity in the range of particles with a diameter between 2 and 4.5 nm. Watanabe[157], Bregoli[158] and Bett[159] showed that the activity increases as the particles size decreases (with a mass activity and ECSA maxima of respectively 160 $A \cdot g^{-1}$ at 0.85 V vs RHE and 200 $m^2 \cdot g^{-1}_{Pt}$ obtained for 1.4 nm crystallite in sulphuric acid)[157], but that diameters lower than 2 nm resulted in poor durability due to spontaneous agglomeration and sintering[49].

iii. Microwave-assisted polyol method

Polyol method was recently improved by the microwave assistance that shortens the conventional 3-hour reaction to 6 minutes[78,160]. Other advantages are also crucial, including homogeneous heating and activation, high reaction rate and chemical yield. These assets result in a uniform nucleation and growth suitable for the synthesis of nanoparticles with a narrow size distribution. Moreover given its dielectric constant (ε = 41.2), ethylene glycol is appropriate for the rapid heating provided by the microwave[160].

2. Pt thin layers

Covering the support with a thin, contiguous and conformal platinum film is a beneficial alternative to catalyse the support[161]. Such extended Pt surface will enhance the catalyst performance by minimising the contribution of edge and corner usually composing the Pt particulate catalyst resulting in much higher surface specific area activity towards the ORR[162,163]. By achieving sufficiently thin coating, such structure will significantly increase the ORR mass activity compared to conventional Pt particles[164]. This approach is also expected to improve the durability of the catalysed support by protecting the support with a highly stable noble metal coverage that will be less energetically subject to sintering and dissolution[165,166] .

i. Physical vapour deposition and chemical vapour deposition

Physical vapour deposition (PVD) describes a family of coating processes that involve vacuum evaporation and the subsequent condensation or the bombardment of the substrate to be coated with energetic positively charged ions. The result of these physical processes is a very strong adhesion between the coating and the tooling substrate and tailored physical, structural and tribological properties of the film[167]. Chemical vapour deposition (CVD) is a chemical process that uses a controlled atmosphere at high temperatures (1000 °C) to achieve reactions between various gaseous phases and the heated surface of substrates within the reactor[168,169]. As different gases are transported through the reactor, distinct coating layers are formed on the substrate. Films deposited by CVD usually have better conformity than films deposited by PVD and therefore CVD is preferred when conformal platinum films are needed.

ii. Atomic layer deposition

Atomic layer deposition (ALD) is a thin film deposition technique that can be considered as a special modification of CVD. On the contrary to the conventional CVD, the precursors are introduced to the reactor in alternate pulses that are separated by inert gas purging[170]. The film grows in a layer-by-layer manner by precursor chemisorption on the substrate surface making the process self-limiting. The thickness of the deposited films can be controlled accurately simply by the number of applied growth cycles. It has a large variety of application such as microelectronics and catalysis. Few Pt ALD processes have been reported for the elaboration of PEMFC electrode[100,171,172]. Among them, the thermal ALD process using a platinum precursor and O_2 gas has become the most widely used[173].

iii. Electrodeposition

Electrodeposition consists on the surface modification of a conductive support by the reduction of a metal salt in solution[174]. The challenge is to determine the conditions that lead preferentially to the 2D growth of a Pt monolayer than to 3D multilayer growth. Smooth Pt monolayer can be deposited on Au substrates[175], but practically it is only possible to obtain a partial Pt monolayer coverage. The formation of a saturated adsorbed hydrogen layer is used to inhibit the 3D growth by quenching the Pt deposition in order to cover the support with Pt islands[176]. Repeating this procedure through cyclic pulses at the suitable potential allow achieving thin continuous platinum film.

iv. Exchange reactions

Surface exchange reactions[177] are also being explored to prepare thin Pt films. Galvanic displacement of Cu monolayer results in a monolayer coverage of the noble metal[178]. Using this technique on previously prepared Cu nanowires, Pt coated copper nanowires have been synthesised as electrocatalyst for the ORR resulting in an ECSA of 31 $m^{2} \cdot g^{-1}$ and high ORR catalytic activity[179]. This method can be extended to various conductive supports with the deposition of a Cu monolayer performed by under potential deposition (UPD)[180] and galvanic displacement[181]. It represents a convenient alternative strategy to direct platinum deposition since the copper film can be easily removed making the electrodeposition easy to study[182]. However, various substrates would present different amount and types of active sites towards the UPD that should be studied to optimise the parameter of the deposition.

D. Conclusion

Proton exchange membrane fuel cells provide electricity with zero emissions at the point of use. The technology has advanced to the point of commercialisation of a fuel cell vehicle in 2015 (Toyota) and installation of thousands of domestic CHP systems in Japan. Pt particles supported on particulate carbon blacks are the state of the art PEMFC electrocatalyst. However, insufficient electrochemical stability of carbon at high potential excursions results in poor durability performance that requires the development of alternative supports. The literature survey on non-carbon supports highlights the suitability of transition metal carbides in terms of electrochemical stability and electronic conductivity. Some of them are also intrinsically active towards the ORR, demonstrating the possibility of synergic effects to promote electrocatalysis.

In this context, the work described in this manuscript aims at the development of transition metal carbides with adapted properties and tuned morphologies to meet the requirements of PEMFC electrocatalyst supports. Starting from a material already designed and investigated in the laboratory, tungsten carbide porous microspheres[105], we developed various chemical and physical synthesis routes to niobium carbide nanomaterials and characterised them as electrocatalyst supports. Particular attention was devoted to the control of surface area and porosity that are key parameters for the support materials.

This manuscript describes a range of synthesis routes leading to the association of the chosen carbide composition with different morphologies and dimensionalities leading to nanostructured materials with high surface areas. These supports have been catalysed by deposition of platinum nanoparticles synthesised by a microwave-assisted polyol method. They have been characterised by their structural and morphological properties, and evaluated as electrocatalyst supports for the oxygen reduction reaction. The results have been compared to a commercial carbon based catalysed support in order to study the feasibility of a replacement of carbon black with a more stable material. After the *ex situ* electrochemical characterisation by rotating disk electrode, membrane electrode assemblies were prepared with the most promising catalysed supports in order to investigate them in a single fuel cell.

E. References

1. J. Hansen, P. Kharecha, M. Sato, V. Masson-Delmotte, F. Ackerman, D. J. Beerling, P. J. Hearty, O. Hoegh-Guldberg, S.-L. Hsu, C. Parmesan, J. Rockstrom, E. J. Rohling, J. Sachs, P. Smith, K. Steffen, L. Van Susteren, K. von Schuckmann and J. C. Zachos, *PLoS One*, 2013, **8**, 81648.

2. F. Birol, *Paris Int. Energy Agency*, 2008.

3. M. Specht, *Int. J. Hydrogen Energy*, 1998, **23**, 387–396.

4. Danish Energy Agency, *Danish Clim. Energy Policy*, 2012. (http://www.ens.dk/en/policy/danish-climate-energy-policy)

5. F. Barbir, *Int. J. Hydrogen Energy*, 1996, **21**, 891–901.

6. S. Maass, F. Finsterwalder, G. Frank, R. Hartmann and C. Merten, *J. Power Sources*, 2008, **176**, 444–451.

7. U. Eberle, B. Müller and R. von Helmolt, *Energy Environ. Sci.*, 2012, **5**, 8780.

8. C. Sealy, *Mater. Today*, 2008, **11**, 65–68.

9. L. Blomen and M. Mugerwa, *Fuel cell systems*, **ch. 1** The first century, Springer Science & Business Media, 2013, 19-24.

10. G. Acres, *J. Power Sources*, 2001, **100**, 60–66.

11. J. Lippert, *Toyota plans mirai fuel-cell car traveling 300 miles per tank*, 2014. (http://www.bloomberg.com/news/articles/2014-11-17)

12. M. C. Williams, J. P. Strakey and W. A. Surdoval, *J. Power Sources*, 2005, **143**, 191–196.

13. N. Behling, *Fuel cells: current technology challenges and future research needs*, **Ch. 1** Introduction, Newness, 2012, 1-6.

14. F. Alcaide, P.-L. Cabot and E. Brillas, *J. Power Sources*, 2006, **153**, 47–60.

15. S. Basu, *Fuel Cell Science and Technology*, Ch. 1 Introduction, Springer, 2007 1-10.

16. B. C. Steele and A. Heinzel, *Nature*, 2001, **414**, 345–52.

17. Breakthrough Technologies Institute, *fuel cell 2000*, 2015. (http://www.fuelcells.org/base.cgim?template=types_of_fuel_cells)

18. J. Larminie, A. Dicks and M. McDonald, *Fuel cell systems explained*, Ch. 1 Introduction, 2003, 1-24.

19. D. Wilkinson, J. Zhang, R. Hui, J. Fergus and X. Li, *Proton exchange membrane fuel cells: materials properties and performance*, 2009.

20. W. Sung, Y. Song, K. Yu and T. Lim, *Recent Advances in the Development of Hyundai· Kia's Fuel Cell Electric Vehicles*, 2010. (http://papers.sae.org/2010-01-1089)

21. T. Nakajima, *Fuel cells & hydrogen for sustainable transport*, 2009. (http://hydrogenlink.net/download/pictures/h2cop15/2_honda-fuelcell-vehicles-copenhagen.pdf)

22. N. M. Markovic, B. N. Grgur and P. N. Ross, *J. Phys. Chem. B, Mater. surfaces, interfaces Biophys.*, **101**, 5405–5413.

23. P. M. Quaino, J. L. Fernández, M. R. Gennero de Chialvo and A. C. Chialvo, *J. Mol. Catal. A Chem.*, 2006, **252**, 156–162.

24. L. Su, W. Jia, C.-M. Li and Y. Lei, *ChemSusChem*, 2014, **7**, 361–78.

25. M. Winter and R. J. Brodd, *Chem. Rev.*, 2004, **104**, 4245–4269.

26. C. Sánchez and A. Bard, *Anal. Chem.*, 2009, **81**, 8094–8100.

27. L. Zhang and Z. Xia, *J. Phys. Chem. C*, 2011, **115**, 11170–11176.

28. E. Yeager, *J. Mol. Catal.*, 1986, **38**, 5–25.

29. J. Zhang, *PEM Fuel Cell Electrocatalysts and Catalyst Layers: Fundamentals and Applications*, ch. 1 PEM Fuel Cell Fundamentals, Springer, 2008, 1-79.

30. V. Zhdanov and B. Kasemo, *Electrochem. commun.*, 2006, **8**, 1132–1136.

31. J. X. Wang, F. A. Uribe, T. E. Springer, J. Zhang and R. R. Adzic, *Faraday Discuss.*, 2008, **140**, 347–62; discussion 417–37.

32. V. Stamenković, T. J. Schmidt, P. N. Ross and N. M. Marković, *J. Electroanal. Chem.*, 2003, **554-555**, 191–199.

33. D. A. Walsh, A. Ejigu, J. Smith and P. Licence, *Phys. Chem. Chem. Phys.*, 2013, **15**, 7548–54.

34. L. Giorgi, E. Antolini, A. Pozio and E. Passalacqua, *Electrochim. Acta*, 1998, **43**, 3675–3680.

35. J. Chen, T. Matsuura and M. Hori, *J. Power Sources*, 2004, **131**, 155–161.

36. R. O'Hayre, D. Barnett and F. Prinz, *Electrochemical proceedings : Proton Conducting Membrane fuel cells IV*, 2006, **2004-21**, 23-37.

37. R. O'Hayre, D. Barnett and F. Prinz, *J. Electrochem. Soc.*, 2005, **152**, A439–A444.

38. D. J. Jones, in *Global Change, Energy Issues and Regulation Policies*, vol. 2, **Ch. 8** Introduction to hydrogen and fuel cell technologies and their contribution to a sustainable energy future, Springer Netherlands, 2013, 161–178.

39. S. Subianto, M. Pica, M. Casciola, P. Cojocaru, L. Merlo, G. Hards and D. J. Jones, *J. Power Sources*, 2013, **233**, 216–230.

40. L. Li, L. Hu, J. Li and Z. Wei, *Nano Res.*, 2015, **8**, 418–440.

41. Y. Shao, G. Yin, Y. Gao and P. Shi, *J. Electrochem. Soc.*, 2006, **153**, A1093.

42. F. Büchi, M. Inaba and T. Schmidt, in *Polymer electrolyte fuel cell durability*, **Ch. 1** stack component-catalyst-dissolution and stabilization of platinum in oxygen cathod, Springer, 2009, 7–29.

43. J. Speder, A. Zana, I. Spanos, J. J. K. Kirkensgaard, K. Mortensen, M. Hanzlik and M. Arenz, *J. Power Sources*, 2014, **261**, 14–22.

44. S. Guo and S. Sun, *J. Am. Chem. Soc.*, 2012, **134**, 2492–5.

45. X. Zhou, J. Qiao, L. Yang and J. Zhang, *Adv. Energy Mater.*, 2014, **4**, 1-25.

46. A.-F. Che, V. Germain, M. Cretin, D. Cornu, C. Innocent and S. Tingry, *New J. Chem.*, 2011, **35**, 2848–2853.

47. R. Makharia, S. Kocha, P. Yu, M. A. Sweikart, W. Gu, F. Wagner and H. A. Gasteiger, *ECS Trans.*, 2006, **1**, 3–18.

48. K. Kinoshita, *Carbon: electrochemical and physicochemical properties*, John Wiley Sons, 1988.

49. Y. Shao, G. Yin and Y. Gao, *J. Power Sources*, 2007, **171**, 558–566.

50. F. N. Büchi, M. Inanba and T. J. Schmidt, Eds., *Polymer Electrolyte Fuel Cell Durability*, Springer-Verlag, New York, 2009.

51. M. Mathias, R. Makharia and H. Gasteiger, *electrocheical Soc. Interface*, 2005, **14**, 24–35.

52. M. Oszcipok, M. Zedda, D. Riemann and D. Geckeler, *J. Power Sources*, 2006, **154**, 404–411.

53. T. F. Fuller, *J. Electrochem. Soc.*, 1993, **140**, 1218.

54. T. W. Patterson and R. M. Darling, *Electrochem. Solid-State Lett.*, 2006, **9**, A183.

55. H. Tang, Z. Qi, M. Ramani and J. F. Elter, *J. Power Sources*, 2006, **158**, 1306–1312.

56. C. Reiser, L. Bregoli and T. Patterson, *Electrochem. Solid-State Lett.*, 2005, **8**, A273.

57. L. Dubau, L. Castanheira, F. Maillard, M. Chatenet, O. Lottin, G. Maranzana, J. Dillet, A. Lamibrac, J.-C. Perrin, E. Moukheiber, A. ElKaddouri, G. De Moor, C. Bas, L. Flandin and N. Caqué, *Wiley Interdiscip. Rev. Energy Environ.*, 2014, **3**, 540–560.

58. D. Rohendi, E. H. Majlan, A. B. Mohamad, W. R. W. Daud, A. A. H. Kadhum and L. K. Shyuan, *Int. J. Hydrogen Energy*, 2015, **40**, 10960–10968.

59. H. Gasteiger, W. Gu and R. Makharia, in *Handbook Of Fuel Cell: Fundamentals Technology And Application*, effisciency loss contributions, Wiley & sons, 2003.

60. A. Honji, *J. Electrochem. Soc.*, 1988, **135**, 355.

61. G. A. Gruver, *J. Electrochem. Soc.*, 1980, **127**, 1219.

62. V. Komanicky, K. C. Chang, A. Menzel, N. M. Markovic, H. You, X. Wang and D. Myers, *J. Electrochem. Soc.*, 2006, **153**, B446.

63. D. C. Johnson, D. T. Napp and S. Bruckenstein, *Electrochim. Acta*, 1970, **15**, 1493–1509.

64. X. Wang, R. Kumar and D. J. Myers, *Electrochem. Solid-State Lett.*, 2006, **9**, A225.

65. K. Kinoshita, J. T. Lundquist and P. Stonehart, *J. Electroanal. Chem. Interfacial Electrochem.*, 1973, **48**, 157–166.

66. Y. Shao-Horn, W. C. Sheng, S. Chen, P. J. Ferreira, E. F. Holby and D. Morgan, *Top. Catal.*, 2007, **46**, 285–305.

67. Q. Li, R. He, J.-A. Gao, J. O. Jensen and N. J. Bjerrum, *J. Electrochem. Soc.*, 2003, **150**, A1599.

68. M. Cai, M. S. Ruthkosky, B. Merzougui, S. Swathirajan, M. P. Balogh and S. H. Oh, *J. Power Sources*, 2006, **160**, 977–986.

69. Y. Yu, H. Li, H. Wang, X-Z. Yuan, G. Wang and M. Pan, 2012, *Journal of Power Sources*, **205**, 10–23.

70. S. Sharma and B. G. Pollet, *J. Power Sources*, 2012, **208**, 96–119.

71. K. Sasaki, F. Takasaki and Z. Noda, *ECS Trans.*, 2010, **33**, 473–482.

72. F. Takasaki, S. Matsuie, Y. Takabatake, Z. Noda, a. Hayashi, Y. Shiratori, K. Ito and K. Sasaki, *J. Electrochem. Soc.*, 2011, **158**, B1270.

73. K. Kanda, Z. Noda, Y. Nagamatsu, T. Higashi, S. Taniguchi, S. M. Lyth, A. Hayashi and K. Sasaki, *ECS Electrochem. Lett.*, 2014, **3**, F15–F18.

74. S. J. Tauster, *Acc. Chem. Res.*, 1987, **20**, 389–394.

75. J. Shim, C.-R. Lee, H.-K. Lee, J.-S. Lee and E. J. Cairns, *J. Power Sources*, 2001, **102**, 172–177.

76. S. H. S. Kang, Y. Y.-E. Sung and W. W. H. Smyrl, *J. Electrochem. Soc.*, 2008, **155**, B1128.

77. Z. Zhang, J. Liu, J. Gu, L. Su and L. Cheng, *Energy Environ. Sci.*, 2014, **7**, 2535-2558.

78. I. Savych, J. Bernard d'Arbigny, S. Subianto, S. Cavaliere, D. J. Jones and J. Rozière, *J. Power Sources*, 2014, **257**, 147–155.

79. P. J. Kulesza, *J. Electrochem. Soc.*, 1989, **136**, 707.

80. P. J. Kulesza, B. Grzybowska, M. A. Malik, M. Chojak and K. Miecznikowski, *J. Electroanal. Chem.*, 2001, **512**, 110–118.

81. M. Watanabe, S. Venkatesan and H. Laitinen, *J. Electrochem. Soc.*, 1983, **130**, 59–64.

82. I. Savych, S. Subianto, Y. Nabil, S. Cavaliere, D. Jones and J. Rozière, *Phys. Chem. Chem. Phys.*, 2015, **17**, 16970–16976.

83. Y. Wang, T. Brezesinski, M. Antonietti and B. Smarsly, *ACS Nano*, 2009, **3**, 1373–1378.

84. S. Cavaliere, I. Jiménez-Morales, G. Ercolano, I. Savych, D. Jones and J. Rozière, *ChemElectroChem*, 2015, n/a–n/a.

85. S.-Y. Huang, P. Ganesan and B. N. Popov, *Appl. Catal. B Environ.*, 2011, **102**, 71–77.

86. J. Ma, A. Habrioux and N. Alonso-Vante, *ChemElectroChem*, 2014, **1**, 37–46.

87. Y. Liu, T. G. Kelly, J. G. Chen and W. E. Mustain, *ACS Catal.*, 2013, **3**, 1184–1194.

88. O. T. M. Musthafa, S. Sampath and O. Muhammedá, *Chem. Commun.*, 2008, **1**, 67–69.

89. H. Zhong, H. Zhang, G. Liu, Y. Liang, J. Hu and B. Yi, *Electrochem. commun.*, 2006, **8**, 707–712.

90. G. Liu, H. M. Zhang, M. R. Wang, H. X. Zhong and J. Chen, *J. Power Sources*, 2007, **172**, 503–510.

91. F. Mazza and S. Trassatti, *J. Electrochem. Soc.*, 1963, **110**, 847.

92. M. Voïnov, D. Bühler and H. Tannenberger, *J. Electrochem. Soc.*, 1971.

93. X. S. Zhou, Y. J. Qiu, J. Yu, J. Yin and S. Gao, *Int. J. Hydrogen Energy*, 2011, **36**, 7398–7404.

94. R. Levy and M. Boudart, *Science,* **181,** 1973, 54773c9.

95. B. Hammer and J. K. Nørskov, *Impact of Surface Science on Catalysis*, Elsevier, 2000, vol. 45.

96. H. Pan, J. Zang, X. Li and Y. Wang, *Carbon N. Y.*, 2014, **69**, 630–633.

97. H. Zheng, Z. Chen, Y. Li and C. Ma, *Electrochim. Acta*, 2013, **108**, 486–490.

98. Y. Ohgi, A. Ishihara, K. Matsuzawa, S. Mitsushima, K. Ota, M. Matsumoto and H. Imai, *Electrochim. Acta*, 2012, **68**, 192–197.

99. L. Yang, Y. C. Kimmel, Q. Lu and J. G. Chen, *J. Power Sources*, 2015, **287**, 196–202.

100. I. J. Hsu, D. A. Hansgen, B. E. McCandless, B. G. Willis and J. G. Chen, *J. Phys. Chem. C*, 2011, **115**, 3709–3715.

101. T. G. Kelly, K. X. Lee and J. G. Chen, *J. Power Sources*, 2014, **271**, 76–81.

102. P. Justin, P. H. K. Charan and G. R. Rao, *Appl. Catal. B Environ.*, 2014, **144**, 767–774.

103. G.-H. Song, M.-Q. Shi, Y.-Q. Chu and C.-A. Ma, *Electrochim. Acta*, 2013, **112**, 53–58.

104. C. Xu, M. Shi, L. Kang and C. Ma, *Mater. Lett.*, 2013, **91**, 183–186.

105. J. Bernard D'Arbigny, G. Taillades, M. Marrony, D. J. Jones and J. Rozière, *Chem. Commun.*, 2011, **47**, 7950–7952.

106. Y. Wang, S. Q. Song, V. Maragou, P. K. Shen and P. Tsiakaras, *Appl. Catal. B-Environmental*, 2009, **89**, 223–228.

107. C. Tang, D. Wang, Z. Wu and B. Duan, *Int. J. Hydrogen Energy*, 2015, **40**, 3229–3237.

108. G. Cui, P. K. Shen, H. Meng, J. Zhao and G. Wu, *J. Power Sources*, 2011, **196**, 6125–6130.

109. Z. Yan, J. Xie and P. K. Shen, *J. Power Sources*, 2015, **286**, 239–246.

110. S. Sui, L. Ma and Y. Zhai, *J. Power Sources*, 2011, **196**, 5416–5422.

111. Y. Liu and W. E. Mustain, *ACS Catal.*, 2011, **1**, 212–220.

112. S. N. Stamatin, J. Speder, R. Dhiman, M. Arenz and E. M. Skou, *ACS Appl. Mater. Interfaces*, 2015, **7**, 6153–6161.

113. Z. Qiu, H. Huang, J. Du, T. Feng, W. Zhang, Y. Gan and X. Tao, *J. Phys. Chem. C*, 2013, **117**, 13770–13775.

114. H. Liu, F. Wang, Y. Zhao and H. Fong, *Nanoscale*, 2013, **5**, 3643–3647.

115. J.-S. Moon, Y.-W. Lee, S.-B. Han and K.-W. Park, *Int. J. Hydrogen Energy*, 2014, **39**, 7798–7804.

116. H. Wang, Y. Ma, W. Lv, S. Ji, J. Key and R. Wang, *J. Electrochem. Soc.*, 2015, **162**, H79–H85.

117. S. Subianto, S. Giancola, G. Ercolano, Y. Nabil, D. Jones, J. Rozière, and S. Cavaliere, *Electrospinning for Advanced Energy and Environmental Applications*, **ch. 2** Electrospun Nanofibers for Low-Temperature Proton Exchange Membrane Fuel Cells, CRCPress, 29-61, 2015.

118. J. Cooley, *US Pat. 692,631*, 1902.

119. D. S. E. Anthony and L. Andrady, *US Pat. 7297305 B2*, 2007.

120. G. Taylor, *Proc. R. Soc. A Math. Phys. Eng. Sci.*, 1969, **313**, 453–475.

121. W. E. Teo and S. Ramakrishna, *Nanotechnology*, 2006, **17**, R89–R106.

122. D. H. Reneker and A. L. Yarin, *Polymer (Guildf).*, 2008, **49**, 2387–2425.

123. G. Taylor, *Proc. R. Soc. London. Ser. A. Math. Phys. Sci.* , 1964, **280** , 383–397.

124. R. Ramaseshan, S. Sundarrajan, R. Jose and S. Ramakrishna, *J. Appl. Phys.*, 2007, **102**, 111101.

125. a. F. Lotus, E. T. Bender, E. a. Evans, R. D. Ramsier, D. H. Reneker and G. G. Chase, *J. Appl. Phys.*, 2008, **103**, 024910.

126. S. Huang, H. Wu, M. Zhou, C. Zhao, Z. Yu, Z. Ruan and W. Pan, *NPG Asia Mater.*, 2014, **6**, e86.

127. C. Mit-uppatham, M. Nithitanakul and P. Supaphol, *Macromol. Chem. Phys.*, 2004, **205**, 2327–2338.

128. F. Coloma, A. Sepulvedaescribano and F. Rodriguezreinoso, *J. Catal.*, 1995, **154**, 299–305.

129. J. J.-H. Park, Y.-W. Y. Ju, S.-H. S. Park, H. H.-R. Jung, K.-S. Yang and W.-J. Lee, *J. Appl. Electrochem.*, 2009, **39**, 1229–1236.

130. C. A. Bessel, K. Laubernds, N. M. Rodriguez and R. T. K. Baker, *J. Phys. Chem. B*, 2001, **105**, 1115–1118.

131. I.-S. Park, K.-W. Park, J.-H. Choi, C. R. Park and Y.-E. Sung, *Carbon N. Y.*, 2007, **45**, 28–33.

132. Y.-J. Wang, D. P. Wilkinson and J. Zhang, *Chem. Rev.*, 2011, **111**, 7625–51.

133. A. Bauer, L. Chevallier, R. Hui, S. Cavaliere, J. Zhang, D. Jones and J. Rozière, *Electrochim. Acta*, 2012, **77**, 1–7.

134. S. Cavaliere, S. Subianto, L. Chevallier, D. J. Jones and J. Rozière, *Chem. Commun. (Camb).*, 2011, **47**, 6834–6836.

135. A. A. B. Suryamas, G. M. G. Anilkumar, S. Sago, T. Ogi and K. Okuyama, *Catal. Commun.*, 2013, **33**, 11–14.

136. H. J. Kim, Y. S. Kim, M. H. Seo, S. M. Choi, J. Cho, G. W. Huber and W. B. Kim, *Electrochem. commun.*, 2010, **12**, 32–35.

137. J. Shui, C. Chen and J. C. M. Li, *Adv. Funct. Mater.*, 2011, **21**, 3357–3362.

138. Y. S. Kim, S. H. Nam, H.-S. Shim, H.-J. Ahn, M. Anand and W. B. Kim, *Electrochem. commun.*, 2008, **10**, 1016–1019.

139. A. Le Viet, M. V. Reddy, R. Jose, B. V. R. Chowdari and S. Ramakrishna, *J. Phys. Chem. C*, 2010, **114**, 664–671.

140. J. Rajan, P. S. Archana, A. Le Viet, Q. L. Bao, K. P. Loh, M. Muhammad Yusoff, G. N. M. A.

Kumar and S. Ramakrishna, *Adv. Mater. Res.*, 2012, **545**, 21–26.

141. K. Nakane, M. Morinaga and N. Ogata, *J. Mater. Sci.*, 2013, **48**, 7774–7779.

142. K.-Y. Chan, J. Ding, J. Ren, S. Cheng and K. Y. Tsang, *J. Mater. Chem.*, 2004, **14**, 505.

143. E. Antolini, *J. Mater. Sci.*, **38**, 2995–3005.

144. C. Coutanceau, S. Brimaud, C. Lamy, J.-M. Léger, L. Dubau, S. Rousseau and F. Vigier, *Electrochim. Acta*, 2008, **53**, 6865–6880.

145. A. Esmaeilifar, S. Rowshanzamir, M. H. Eikani and E. Ghazanfari, *Energy*, 2010, **35**, 3941–3957.

146. E. Lebègue, S. Baranton and C. Coutanceau, *J. Power Sources*, 2011, **196**, 920–927.

147. H. Bönnemann and R. Brinkmann, *J. New Mater. Electrochem. Syst.*, 2000, **3**, 199–206.

148. M. Boutonnet, J. Kizling, P. Stenius and G. Maire, *Colloids and Surfaces*, 1982, **5**, 209–225.

149. F. Fievet, J. Lagier, B. Blin, B. Beaudoin and M. Figlarz, *Solid State Ionics*, 1989, **33**, 198–205.

150. G. Viau, P. Toneguzzo and A. Pierrard, *Scr. Mater.*, 2001, **44**, 2263–2267.

151. C. Bock, C. Paquet, M. Couillard, G. A. Botton and B. R. MacDougall, *J. Am. Chem. Soc.*, 2004, **126**, 8028–37.

152. H.-S. Oh, J.-G. Oh, Y.-G. Hong and H. Kim, *Electrochim. Acta*, 2007, **52**, 7278–7285.

153. M. L. Sattler and P. N. Ross, *Ultramicroscopy*, 1986, **20**, 21–28.

154. M. Peuckert, *J. Electrochem. Soc.*, 1986, **133**, 944.

155. N. Markovic, H. Gasteiger and P. N. Ross, *J. Electrochem. Soc.*, 1997, **144**, 1591–1597.

156. Y. Takasu, N. Ohashi, X.-G. Zhang, Y. Murakami, H. Minagawa, S. Sato and K. Yahikozawa, *Electrochim. Acta*, 1996, **41**, 2595–2600.

157. M. Watanabe, S. Saegusa and P. Stonehart, *Chem. Lett.*, 1988, **9**, 1487–1490.

158. L. J. Bregoli, *Electrochim. Acta*, 1978, **23**, 489–492.

159. J. Bett, J. Lundquist, E. Washington and P. Stonehart, *Electrochim. Acta*, 1973, **18**, 343–348.

160. M. Tsuji, M. Hashimoto, Y. Nishizawa, M. Kubokawa and T. Tsuji, *Chemistry*, 2005, **11**, 440–52.

161. C. T. Campbell, *Surf. Sci. Rep.*, 1997, **27**, 1–111.

162. N. M. Marković, T. J. Schmidt, V. Stamenković and P. N. Ross, *Fuel Cells*, 2001, **1**, 105–116.

163. N. Kristian and X. Wang, *Electrochem. commun.*, 2008, **10**, 12–15.

164. V. Stamenkovic, B. S. Mun, K. J. J. Mayrhofer, P. N. Ross, N. M. Markovic, J. Rossmeisl, J. Greeley and J. K. Nørskov, *Angew. Chemie*, 2006, **118**, 2963–2967.

165. R. R. Adzic, J. Zhang, K. Sasaki, M. B. Vukmirovic, M. Shao, J. X. Wang, a. U. Nilekar, M. Mavrikakis, J. a. Valerio and F. Uribe, *Top. Catal.*, 2007, **46**, 249–262.

166. K. Sasaki, J. . Wang, M. Balasubramanian, J. McBreen, F. Uribe and R. . Adzic, *Electrochim. Acta*, 2004, **49**, 3873–3877.

167. R. F. Bunshah, *J. Vac. Sci. Technol. A Vacuum, Surfaces, Film.*, 1985, **3**, 553.

168. S. Yamazaki, *US Pat. 4,869,923*, 1989.

169. J. Crawley and V. Saywell, *US Pat. 5,871,586*, 1999.

170. M. Leskelä and M. Ritala, *Thin Solid Films*, 2002, **409**, 138–146.

171. C. Liu, C.-C. Wang, C.-C. Kei, Y.-C. Hsueh and T.-P. Perng, *Small*, 2009, **5**, 1535–8.

172. M. Lashdaf, J. Lahtinen, M. Lindblad, T. Venäläinen and A. O. I. Krause, *Appl. Catal. A Gen.*, 2004, **276**, 129–137.

173. H. C. M. Knoops, a. J. M. Mackus, M. E. Donders, M. C. M. van de Sanden, P. H. L. Notten and W. M. M. Kessels, *Electrochem. Solid-State Lett.*, 2009, **12**, G34.

174. A. Arvia, *J. New Mater. Electrochem. Syst.*, 2004, **7**, 133–144.

175. T. Kondo, M. Shibata, N. Hayashi, H. Fukumitsu, T. Masuda, S. Takakusagi and K. Uosaki, *Electrochim. Acta*, 2010, **55**, 8302–8306.

176. Y. Liu, D. Gokcen, U. Bertocci and T. P. Moffat, *Science*, 2012, **338**, 1327–30.

177. D. Gokcen, S.-E. Bae and S. R. Brankovic, *Electrochim. Acta*, 2011, **56**, 5545–5553.

178. S. R. Brankovic, J. X. Wang and R. R. Adžić, *Surf. Sci.*, 2001, **474**, L173–L179.

179. S. M. Alia, K. Jensen, C. Contreras, F. Garzon, B. Pivovar and Y. Yan, *ACS Catal.*, 2013, **3**, 358–362.

180. V. Sudha and M. Sangaranarayanan, *J. Phys. Chem. B*, 2002, **106**, 2699–2707.

181. H. Tang, J. H. Chen, M. Y. Wang, L. H. Nie, Y. F. Kuang and S. Z. Yao, *Appl. Catal. A Gen.*, 2004, **275**, 43–48.

182. M. Khosravi and M. K. Amini, *Int. J. Hydrogen Energy*, 2010, **35**, 10527–10538.

F. Table of Figures

Chapter II: Niobium carbide nanostructures as electrocatalyst support

A. Introduction

This chapter describes the synthesis and characterisation of nanostructured NbC based electrocatalyst supports. The choice of niobium carbide has been justified by a preliminary investigation of the stability and electrical conduction properties of commercial bulk NbC. This study showed a suitable chemical stability in sulphuric acid at 80 °C, a BET surface area of 1 $m^2 \cdot g^{-1}$ calculated from the N_2 adsorption/desorption and an electrical conductivity of 18 $S \cdot m^{-1}$ at 20 °C. This value is 2 orders of magnitude lower than that obtained for carbon Vulcan XC 72 (5 – 14 10^2 $S \cdot m^{-1}$ at 20° C) but makes it a better candidate as electrocatalyst support than other carbides e.g. tantalum carbide (6 $S \cdot m^{-1}$). (Conductivities were measured with an in house device using the Van der Pauw method. Further details concerning this characterisation are reported in the Experimental Annex). The expected low surface area of bulk niobium carbide justifies the synthesis of a NbC based nanomaterial with a controlled morphology that will provide the required porosity. The characterisation of this material sets up the characterisation protocol that will be applied to the other synthesised materials presented in chapters III and IV.

B. Synthesis and characterisation

1. Synthesis of niobium carbide nanostructures

Metal carbides are usually prepared by powder metallurgy techniques such as the direct reaction of metal or metal hybrid powders with carbon[1]. Concerning niobium carbide, the reported temperatures for a direct carburation are in the range of 1300 – 1400 °C[1,2]. Another kind of synthesis is the conversion of niobium oxide into carbide taking place at lower temperatures but for longer time (e.g. 17 hours at 900 °C[3,4]).

In order to promote the formation of a porous morphology, the synthesis protocol of NbC nanostructures was inspired by a 3-step route previously developed in the AIME – ICGM laboratory giving rise to WC highly porous hollow microspheres[5]. This synthesis is made of 3 steps: a glucose template hydrothermal synthesis and 2 specific thermal treatments (carburation and methanation) (Table 1).

Table 1. Synthesis route to niobium carbide nanostructures.

Step	Conditions
1. Hydrothermal synthesis	12 h 170 °C in autoclave
2. Carburation	3 h 1100 °C in Ar (2 °C · min^{-1})
3. Methanation	2h 1100 °C in H2 (4 °C · min^{-1})

This synthesis consists on the formation in autoclave of carbon microspheres[6] containing a niobium salt (ammonium niobate oxalate, ANO) that are used respectively as carbon and niobium sources during the carburation step at 1100 ° C. Microspheres are obtained by the condensation and polymerisation of the glucose precursor. After aromatisation, the formed oligomers result in microspheres with a carbonised core and an hydrophilic surface[7]. Their growth is controlled by time, temperature and glucose concentration. In a further step, called carburation, the conversion to carbide takes place. The morphology obtained after each step is characterised in the dedicated part (paragraph B.2.) The conversion to carbide is not complete, thus the synthesised materials contain residual carbon. In order to remove the latter, three methanation steps at 1100 °C under hydrogen were performed A temperature programmed reduction (TPR) furnace equipped with a thermal conductivity detector (TCD) has been used to monitor the progression of the methanation reaction[8].

Indeed, gases produced and consumed during the reaction **(1)** affect the thermal conductivity of the furnace gas.

$$C + 2H_{2\,(g)} \rightarrow CH_{4\,(g)} \textbf{(1)}$$

Figure 1 presents the thermal conductivity signal obtained during the 2 first methanations (ongoing methanation) and during the last methanation (completed methanation). The thermal conductivity of CH_4 (0.030 $W \cdot m^{-1} \cdot K^{-1}$ at 25°C) is negligible compared to that of H_2 (0.168 $W \cdot m^{-1} \cdot K^{-1}$ at 25°C)[9]. Therefore, the decrease in thermal conductivity matches the consumption of H_2 during the methanation. While the methanation reaction was ongoing, a plateau was observed on the TCD curves (Figure 1a). At the end of a complete methanation (Figure 1b) that results in a negligible amount of residual carbon, the initial thermal conductivity was reached.

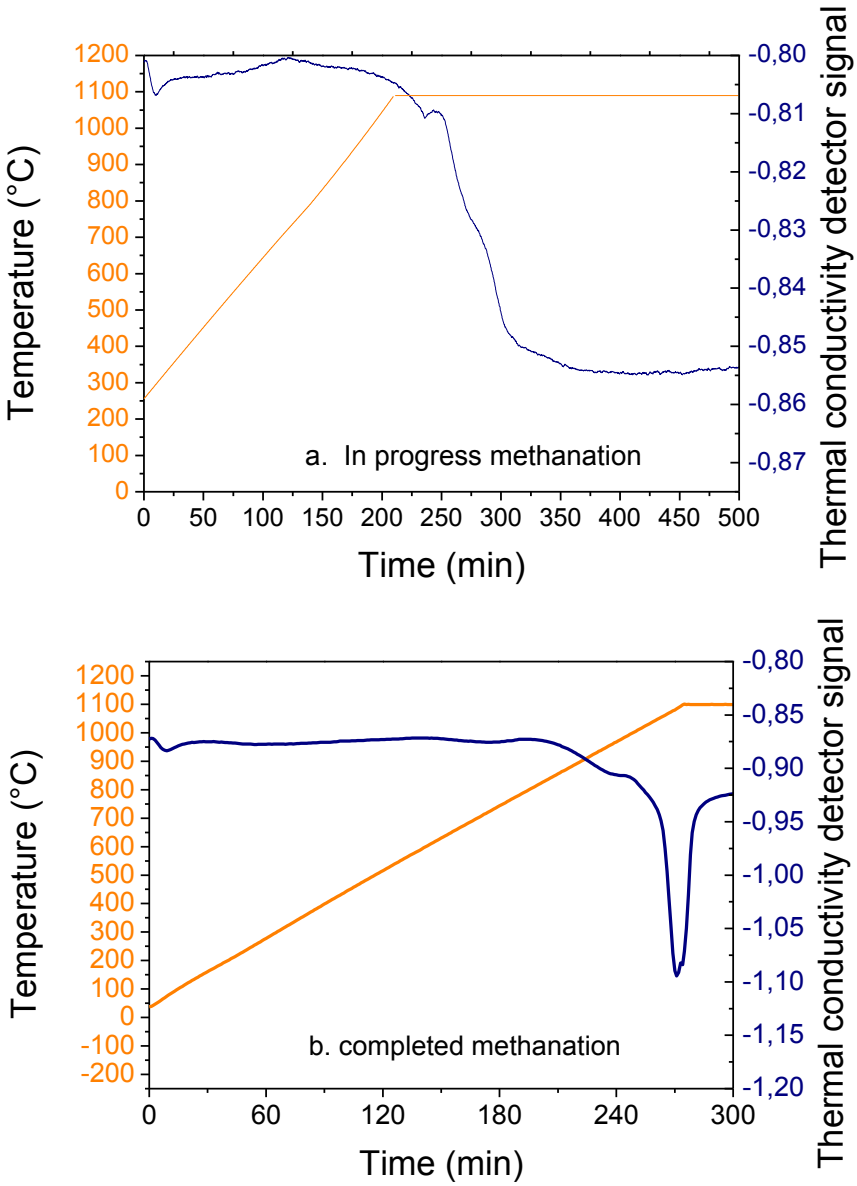

Figure 1. Evolution of the thermal conductivity during the methanation of the NbC/C nanostructures.

a. in progress b. completed

The final support was obtained after 3 consecutive methanations lasting respectively 4.5, 4.5 and 0.5 hours. These prolonged reactions could eventually led to further reduced Nb containing phases such as metallic niobium or Nb_2C. Their absence was assessed by X-ray diffraction (XRD) and X-ray photoelectron (XPS) spectroscopy presented in paragraph B.2. The calculation of the residual carbon amount is described in paragraph B.2.

2. Morphological characterisation of niobium carbide nanostructures

The morphology of NbC materials obtained with the 3-step synthesis was investigated by SEM. After each step it was possible to follow the morphology evolution.

The hydrothermal synthesis (step 1) resulted in the structuration of microspheres (Figure 2) with a number and volume weighted average diameter of respectively 3.9 and 4.7 µm. The diameter distributions are reported in the Figure 3. The volume weighted size distribution calculated by considering perfectly spherical objects affects the weighting related to the amount of material, while the number weighted size distribution is only relevant to the number of microspheres. Correlating these information is essential to obtain a reliable size distribution[10].

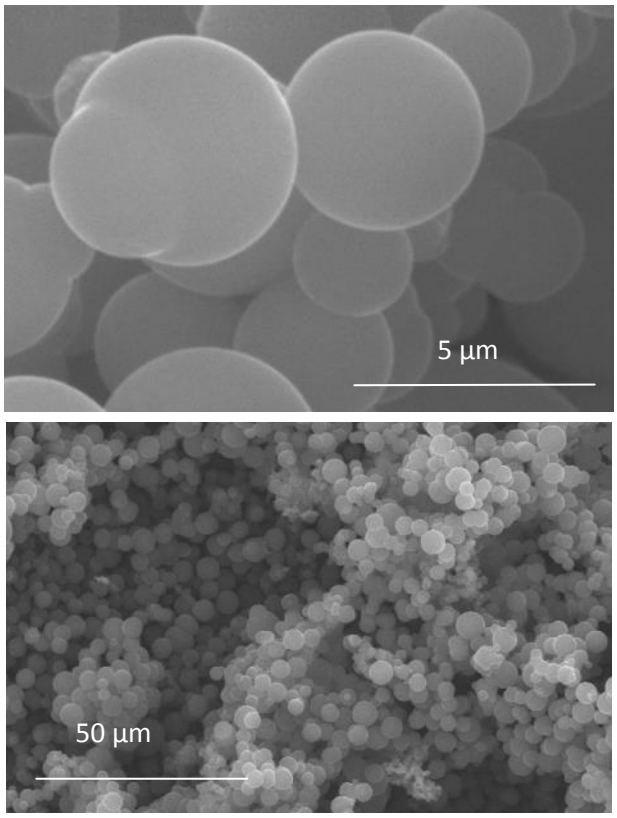

Figure 2. SEM micrograph of ANO/glucose composite microspheres obtained by hydrothermal synthesis.

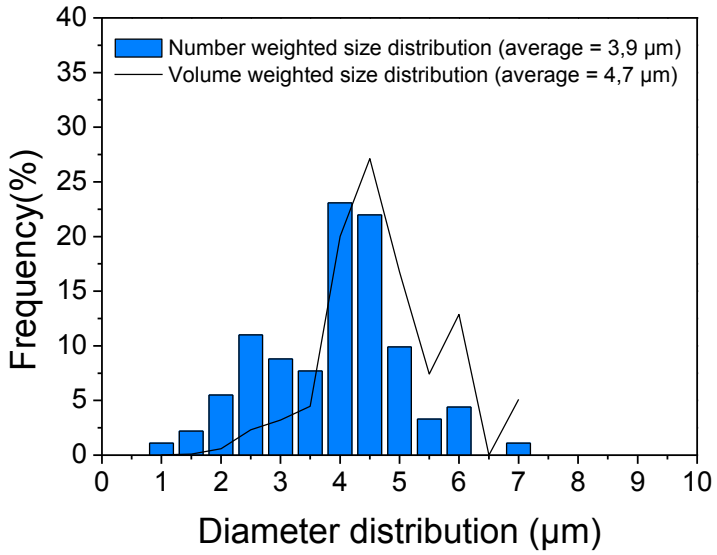

Figure 3. Size distribution of the NbC/C microspheres obtained after de hydrothermal synthesis.

After the carburation (step 2) nanostructures as well as filaments at the surface of the microsphere appear (Figure 4). Energy Dispersive X-ray does not reveal any composition difference between microspheres and nanostructures morphologies. After the methanation step, SEM micrographs show NbC grains made of nanostructures (Figure 5). Their diameter size is in the 25 - 100 nm range. Because of their various crystallite shapes, no accurate size distribution has been plotted. The residual carbon was identified before its complete removal as a “binding” phase between the grains. Figure 6 shows the high resolution SEM observation of this amorphous carbon surrounded by NbC grains. Some broken microspheres remaining from glucose structuration were observed among these NbC nanostructures (Figure 7).

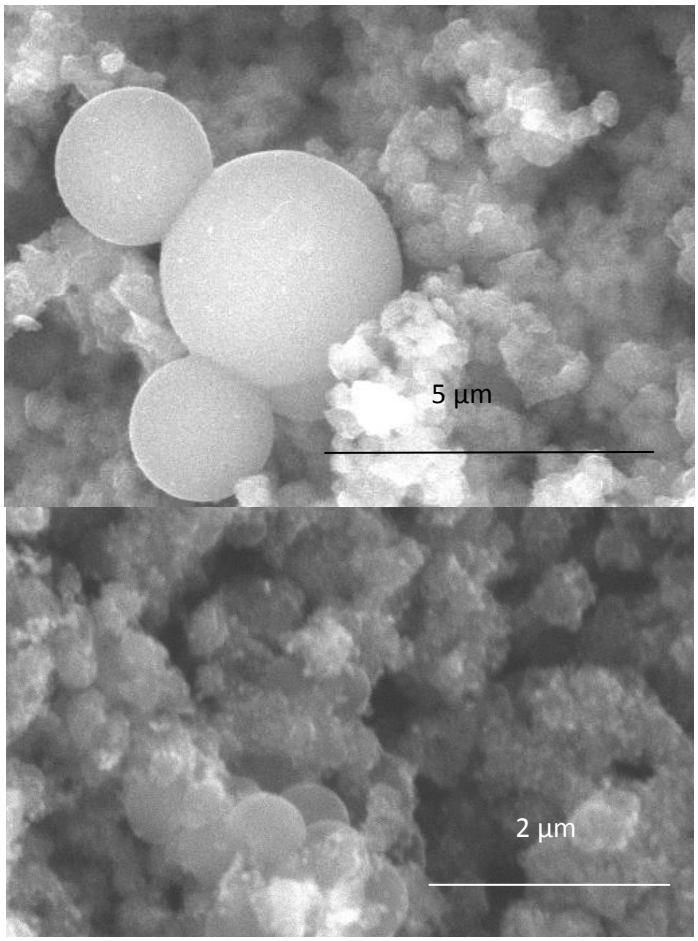

Figure 4. SEM micrograph of NbC/C nanostructures and microspheres after carburation.

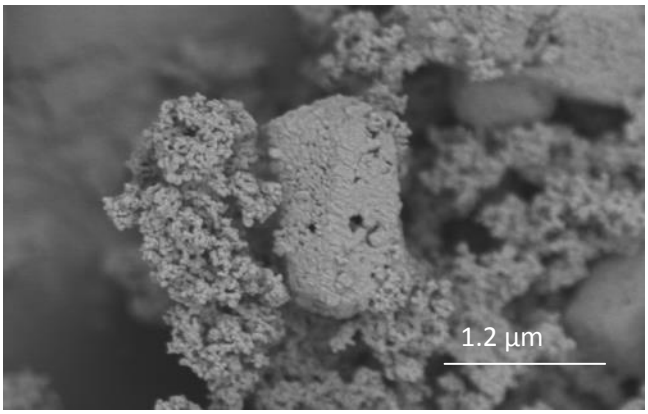

Figure 5. SEM micrograph of NbC/C nanostructures obtained after methanation.

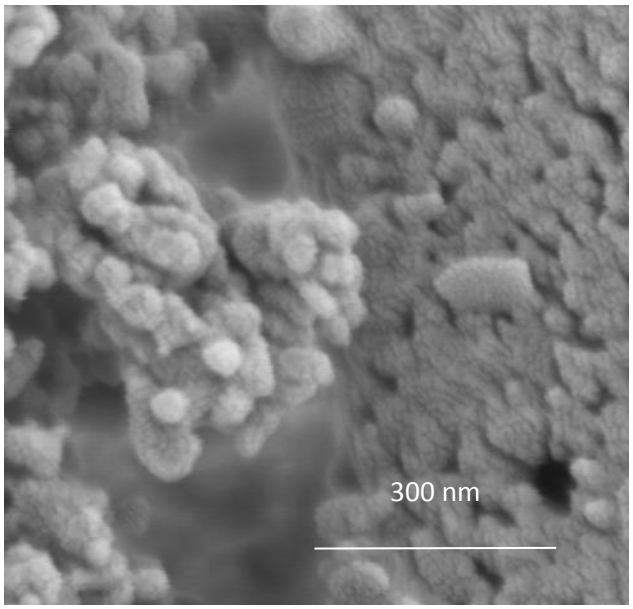

Figure 6. SEM micrograph of NbC/C (94/6 $\%_{wt}$) nanostructures with a small volume of amorphous carbon.

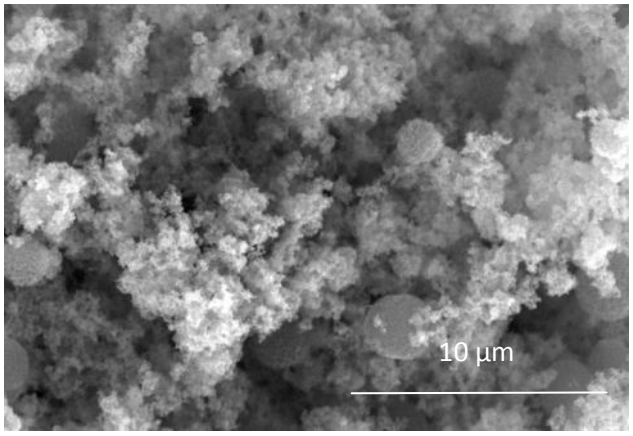

Figure 7. SEM micrograph of NbC/C nanostructures with vestiges of microspheres after 3 methanation steps.

Together with the nanostructured morphology, specific surface area is an essential requirement for the synthesis of electrocatalyst supports. Nitrogen adsorption/desorption was thus performed on the prepared NbC/C materials (Figure 8). The obtained isotherms are of type IV, typical for a mesoporous material and is accompanied by a H3 hysteresis loop often given by aggregates of particles[11]. The difference between the two isotherms suggests that the removed porosity is mainly due to micropores, attributable to the presence of residual microporous carbon.

The BET surface area was calculated for the synthesised materials with different residual carbon amount obtained by tuning the methanation steps. The calculated values were then plotted versus the residual carbon content and fitted with a linear curve (Figure 9). The BET surface area rises with the amount of carbon suggesting that a large part of this surface area can be attributed to the porosity of carbon. The extrapolation of this linear curve allows estimating the surface area of a hypothetical pure NbC without residual carbon. The linear fit obtained with a range of materials with low carbon content gives an intercept of 52 $m^2 \cdot g^{-1}$. The synthesis of a material with 0 % residual carbon requires prolonged methanation steps which led to NbC grain growth that does not allow reaching such a high surface area**.** The materials that were selected for further evaluation as electrocatalyst support are a compromise between their carbon content and BET surface area. Indeed, on a one hand our aim is to find a corrosion resistant support alternative to carbon, and on the other hand the latter should have a sufficient surface area and porosity to allow efficient electrocatalyst dispersion. The prepared NbC/C feature a BET surface area between 65 and 90 $m^2 \cdot g^{-1}$ and a residual carbon amount of less than 10 %.

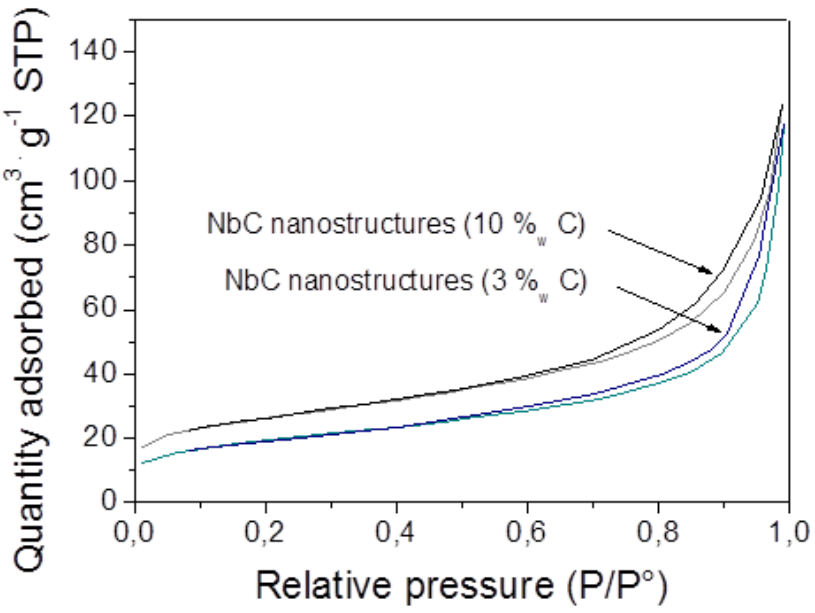

Figure 8. Nitrogen adsorption/desorption of two NbC/C nanostructures (3 and 10 $\%_{wt}$ of residual carbon).

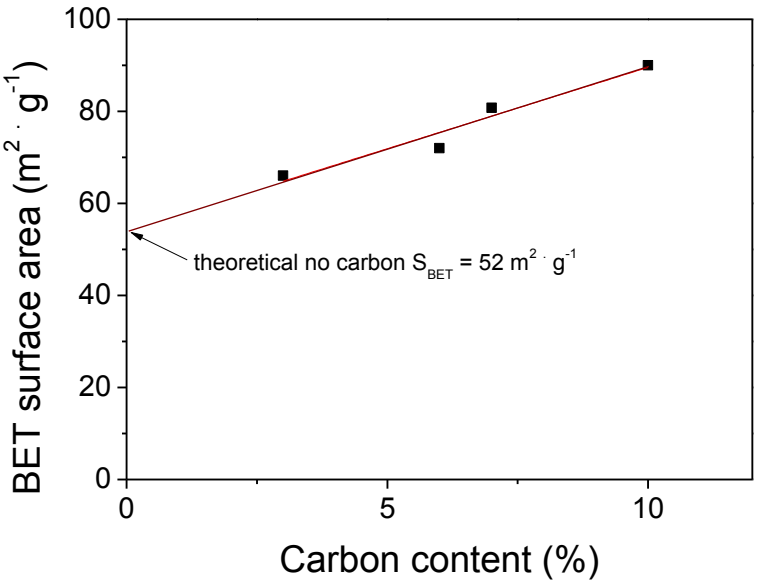

Figure 9. BET surface area of the NbC materials as a function of their residual carbon content determined by TGA (paragraph B.3).

This synthesis route provides with the required specific surface area for the targeted application. However, the large proportion of microporosity might be not suitable for good electrocatalyst dispersion.

3. Characterisation of the chemical and structural composition of niobium carbide nanostructures

The chemical and structural composition of the synthesised material was characterised after carburation (Figure 10) and methanation (Figure 11) steps by powder X-ray diffraction (XRD).

After carburation the cubic phase pattern of niobium carbide (JCPDS reference 038 – 1364 cubic Fm – 3m) was identified as well as broadened peaks matching the possible excess carbon in 20 – 30 °/2θ and 40 – 45 °/2θ[12,13] highlighted in Figure 10.

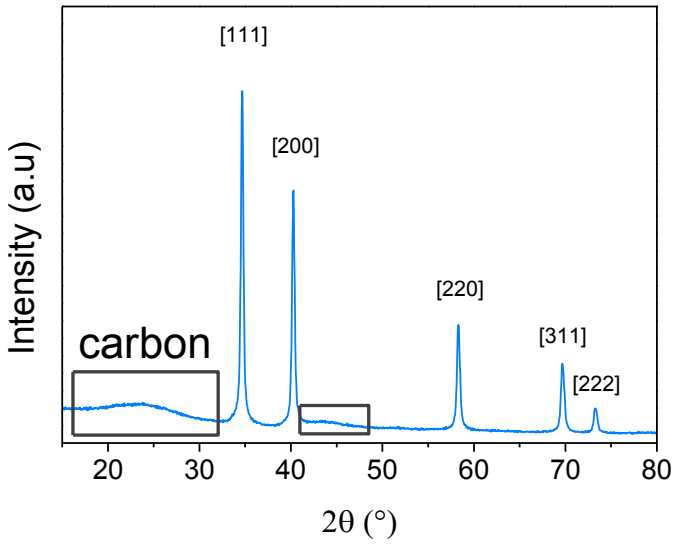

Figure 10. X-ray diffractogramm of the NbC material after carburation (step 2).

After methanation, the cubic phase of niobium carbide (ref 038 – 1364 cubic Fm – 3m) was the only crystalline phase present in the X-ray diffractogramm (Figure 11). 14, 14 and 13 nm and 18, 16 20 nm were calculated as crystallite size with the Scherrer formula with the respective miller planes ([111], [200] and [220]). This increase during the methanation confirms the hypothesis of a grain growth during the methanation. As a proof of the removal of a part of the residual carbon the broadened peak at 20 – 30 °2θ was no more visible. However, to quantify the possible amount of residual carbon not detectable by XRD, a method based on thermogravimetric analysis and further validated by X-ray fluorescence (XRF) and elemental analysis was elaborated.

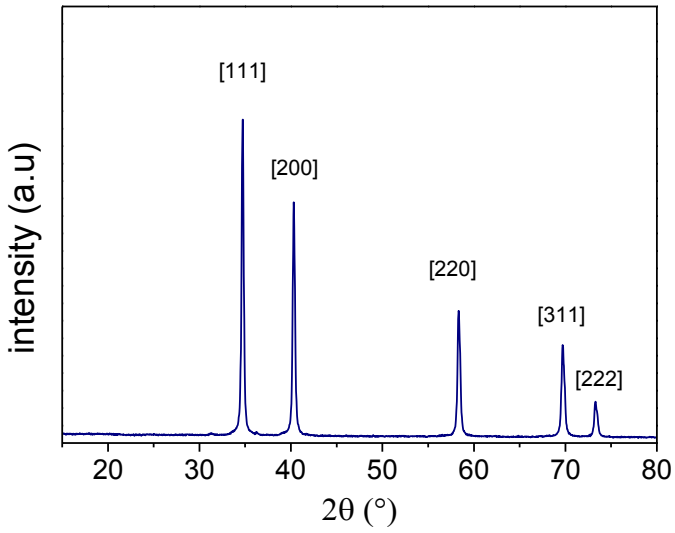

Figure 11. X-ray diffractogramm of the material after methanation (step 3).

The amount of residual carbon (i.e. $C_{residual}$ weight to the total weight of niobium carbide + $C_{residual}$) was determined by thermogravimetric analysis (TGA) at 1100 °C in air. During this heat treatment two reactions take place simultaneously[14]:

1. Oxidation of niobium carbide to a mixture of niobium oxides Nb_2O_5 and NbO_2 that involves a mass gain[14].

2. Oxidation of carbon to CO and CO_2 that gives a mass loss[15,16].

These 2 reactions occur in the same temperature range and cannot be differentiated. However, the mass variation during TGA is directly related to the NbC/C ratio. A calibration (Figure 13) was made using standards prepared by mixing known amounts of commercial niobium carbide and carbon Vulcan XC 72 R. This calibration links the mass variation (Figure 13) with the fraction of residual carbon in the NbC/C mixture. The TGA curve of the standards (Figure 12) presents the same weight loss patterns of synthesized NbC materials (Figure 14 and Figure 15) reflecting the 2 identified reactions.

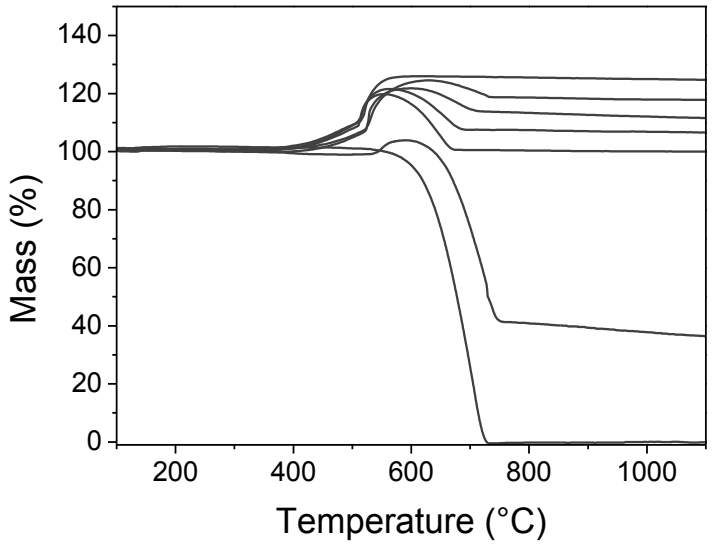

Figure 12. Thermogravimetric analyses of NbC/C standards (mixture of commercial NbC (Alfa Assar) and Vulcan XC 72 R (Cabot).

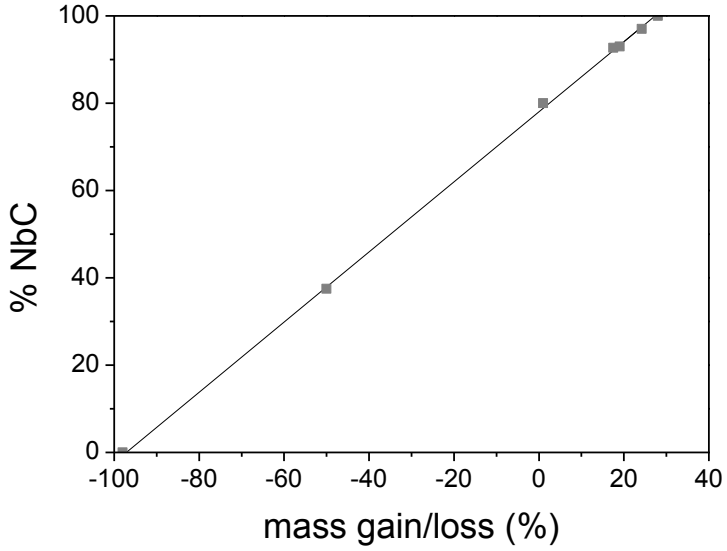

Figure 13. Calibration curve for the determination of NbC and carbon content obtained by TGA.

The TGA of NbC nanostructures before methanation displays an overall mass gain that corresponds to NbC/C = 50/50 (Figure 14).

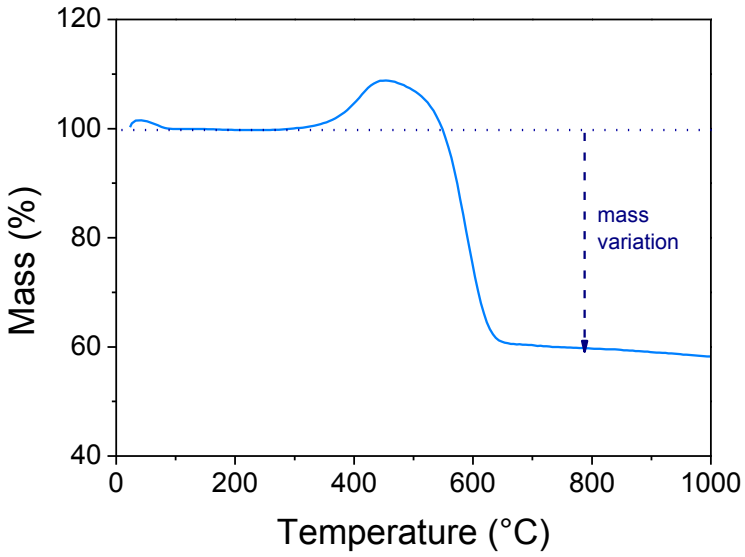

Figure 14. Thermogravimetric analysis of synthesised NbC/C after the carburation (step 2).

After 1 and 3 methanations, it displays an overall mass gain that corresponds respectively to NbC/C = 85/15 and 97/3 (Figure 14). The material with the lowest amount of residual carbon was selected for further analysis and characterisation. When repeated, the synthesis route included 3 consecutive methanations to 1100 °C.

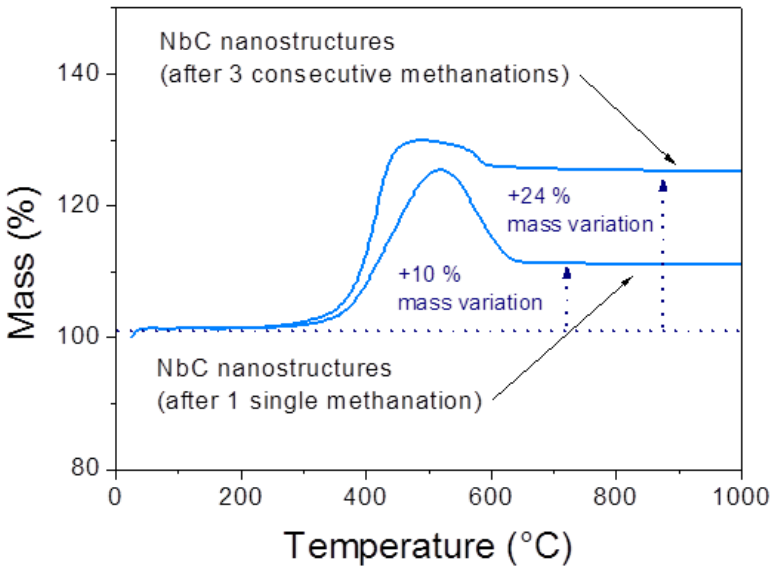

Figure 15. Thermogravimetric analyses of synthesised NbC/C after 1 and 3 consecutive methanations (step 3).

The fraction of residual carbon contained in the synthesised niobium carbide materials obtained by TGA was confirmed by carbon hydrogen nitrogen sulphur (CHNS) elemental analysis[17,18].

Indeed for the sample with the lowest residual carbon i.e. NbC/C = 98/2, elemental analysis indicates that the total amount of carbon is 13 $\%_{wt}$, which leads to an amount of residual (non-carbide) carbon of 2 $\%_{wt}$, if it is considered that carbon is present in niobium carbide and as amorphous carbon, and that niobium is only present as niobium carbide. These hypotheses are consistent with the X-ray diffraction (XRD) characteristics of the material.

The chemical composition of the material was also confirmed by X-ray fluorescence (XRF). Two calibrations were made by mixing carbon Vulcan XC 72 R and commercial niobium carbide. Carbon and niobium amounts were plotted versus the intensity of the signal matching these elements (Figure 16 and Figure 17). The carbon calibration leads to 13 $\%_{wt}$ of carbon, which is consistent with the two previous analysis methods. Given the Nb calibration, the amount of Nb is 94 $\%_{wt}$, which is above the theoretical value for a pure NbC material (89 $\%_{wt}$). This unexpected value can be explained by the accuracy of the method in the extremity of the Nb content range.

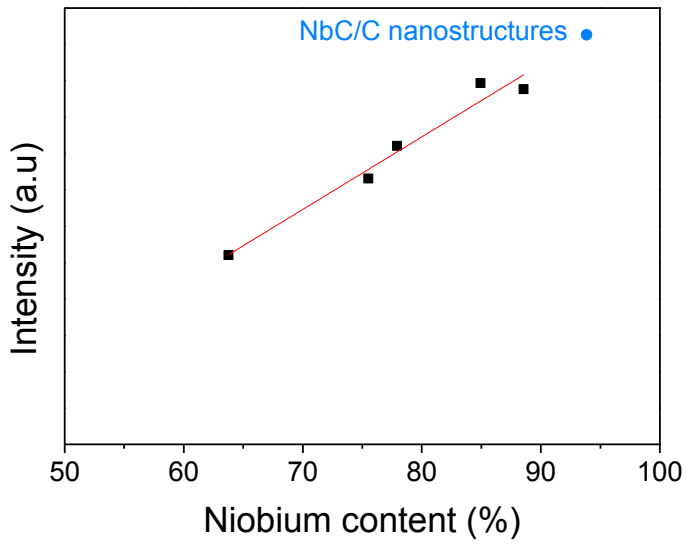

Figure 16. XRF calibration for the determination of niobium content.

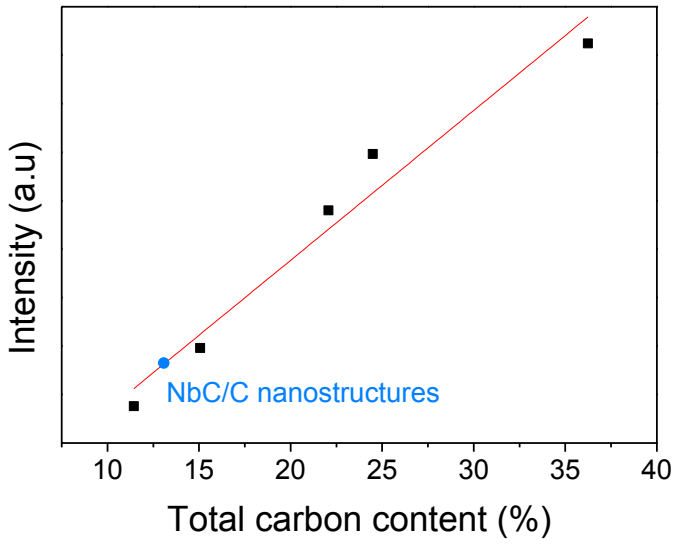

Figure 17. XRF calibration for the determination of carbon content.

The Nb / C ratio can be increased by the presence of Nb in a lower oxidation state (Nb_2C or $Nb_{metallic}$). This hypothesis is disproved by the XRD that did not display the pattern of other phase than NbC. However, the presence of other amorphous Nb containing species is still possible. For this reason, X-ray photoelectron spectroscopy (XPS) was carried out to verify the possible presence of Nb_2C or $Nb_{metallic}$ that could have been formed by reduction during the methanation step.

Figure 18 shows the high resolution XPS spectrum of the Nb region obtained for the synthesised NbC after methanation that led to 3 $\%_{wt}$ of residual carbon. The peaks of 3d Nb orbital (Nb $3d_{5/2}$= 204.1, Nb $3d_{3/2}$ 206.8 eV) and Nb_2O_5 (Nb $3d_{5/2}$= 207.4, Nb $3d_{3/2}$ 210.12) are fitted by two doublets in accordance with the theoretical energy values[19] (Nb $3d_{5/2}$= 204.7 eV for NbC[20] and Nb $3d_{5/2}$= 207.2 eV for Nb_2O_5[21]).

By integrating the Nb $3d_{5/2}$ peaks of NbC and Nb_2O_5, 36 $\%_{at}$ of oxide was calculated. Since this significant amount of niobium pentoxide was not visible on XRD it can be concluded that this compound is concentrated at the surface of the NbC materials as a thin amorphous layer. This surface passivation has been already reported for NbC particles[20]. A particular attention will be paid to the resistivity of such a layer as it could insulate the electrocatalyst from the conductive NbC core of the support[22]. The evolution of this niobium oxide layer and its progression to the core of the material could be an issue regarding the long-term stability. Any traces of metallic niobium or diniobium carbide Nb_2C have been detected by XPS, proving that the reaction was stopped before further reduction of niobium carbide.

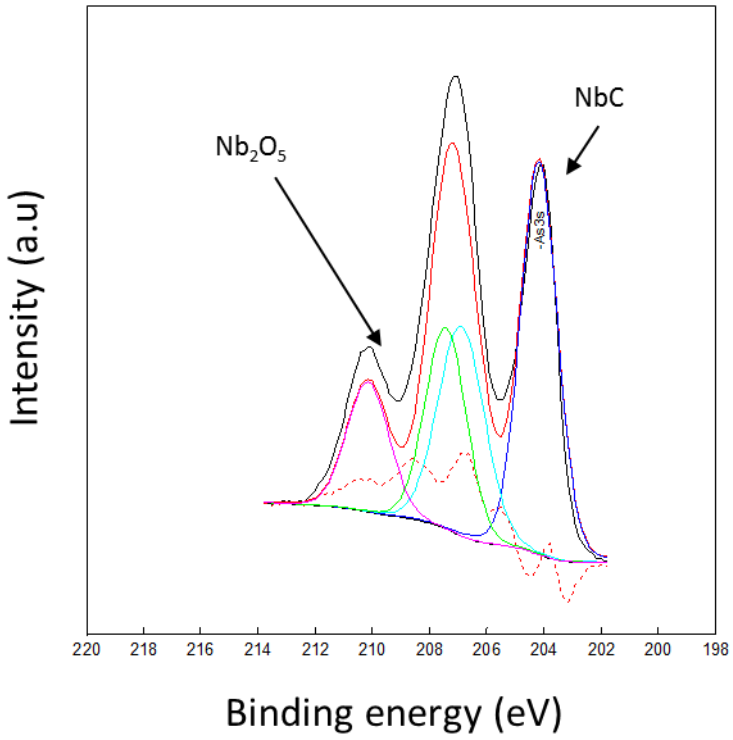

Figure 18. XPS high resolution spectrum of the Nb 3d region for NbC/C nanostructures.

4. Electrical characterisation of niobium carbide nanostructures

Electrical conductivity of the NbC nanostructures was measured using Van der Pauw method as a function of the temperature, up to 200 °C. At room temperature (25 °C) a value of 10^3 $S \cdot m^{-1}$ was obtained. This value is higher than the 5.1 10^2 $S \cdot m^{-1}$ obtained for carbon Vulcan XC 72 R and the 0.18 $S \cdot m^{-1}$ obtained for commercial NbC. For the synthesised NbC, a small increase of the electrical conductivity was observed when increasing the temperature, while the conductivity of carbon slightly increased with the temperature in the range of the study (20 – 200 °C). The high conductivity of the NbC/C nanostructures compared to pure bulk NbC can be attributed to the residual carbon still present in the material (6 $\%_{wt}$) that compensate the increase of grain boundaries due to the nanostructured morphology that should result in a lower conductivity. The nature of the residual carbon could explain the higher conductivity than carbon Vulcan XC 72 R.

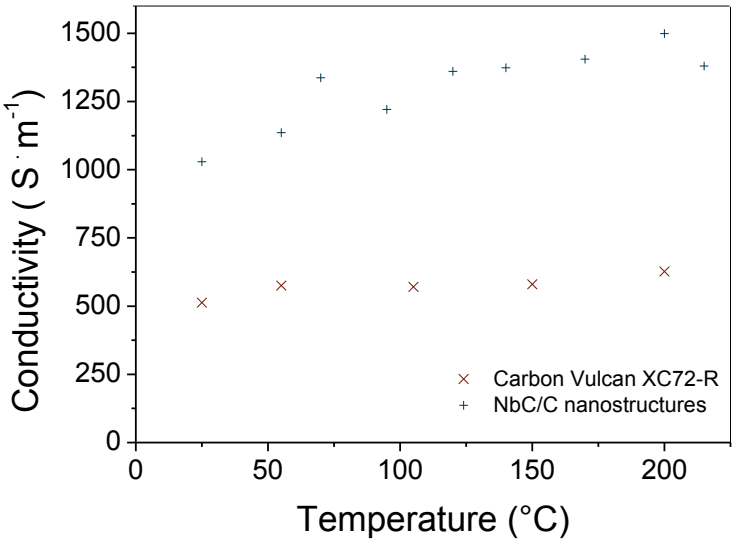

Figure 19. Electrical conductivity values measured in air for carbon Vulcan XC 72-R and NbC nanostructures as a function of the temperature.

C. Synthesis and characterisation of Pt supported on NbC nanostructures

1. Synthesis of Pt supported on NbC nanostructures

To be investigated as electrocatalyst support, the material was loaded with a platinum based electrocatalyst. Thus the preparation of the catalysed support consists of two consecutive steps: the synthesis of platinum particles and their deposition onto the NbC nanostructures.

Platinum particles have been prepared by the polyol method that is presented in the chapter 1 in the paragraph D.3. This synthesis route, developed by Fievet et al[23], was improved by microwave assistance. The standard 2 hours long reflux at 160 °C have been replaced by a 6 minutes microwave treatment that produces platinum nanoparticles with a narrow size distribution[24,25]. The latter will be used as well to catalyse the supports investigated in the third and fourth chapter in order to compare their performance as electrocatalyst support for PEMFC cathodes.

Zeta potential measurements were performed on platinum particles and NbC nanostructures to study the influence of the pH on the surface charge in order to improve the adhesion of the nanocatalyst. At acidic pH (5 – 2) the surface charges of the electrocatalyst is positive while that of the support is negative. Therefore, in this pH range the electrostatic interaction is favourable for the electrocatalyst deposition[26]. After the Pt nanoparticle preparation, the pH of their colloidal suspension was adjusted to 4. A suspension containing the NbC nanostructures was then added to it and let reacting. After filtration and rinsing, the catalysed was activated with a short heat treatment at 160 °C in air[27] to remove eventual traces of ethylene glycol on its surface.

2. Physico-chemical characterisation of Pt supported on NbC nanostructures

Size and distribution of the synthesised Pt particles were evaluated by TEM microscopy (Figure 20).

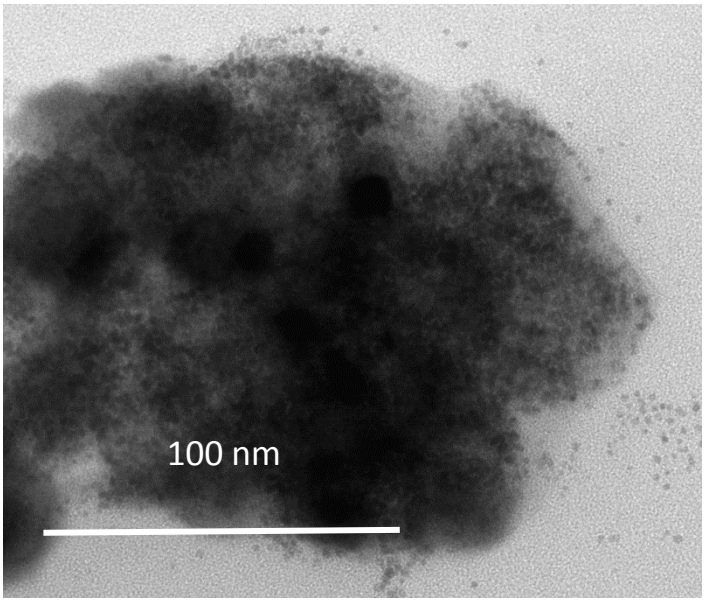

Figure 20. TEM micrographs of the NbC nanostructures catalysed with Pt nanoparticles.

The diameter distribution reported in Figure 21 displays a narrow distribution from 1.5 nm to 5 nm with an average of respectively 3.1 nm or 3.3 nm for a number or volume-weighted calculation. Given the small size of the particles, the number weighted size distribution leads to an under-estimation of the particles size. The volume-weighted size distribution gives a better representation of the actual particles size [10].

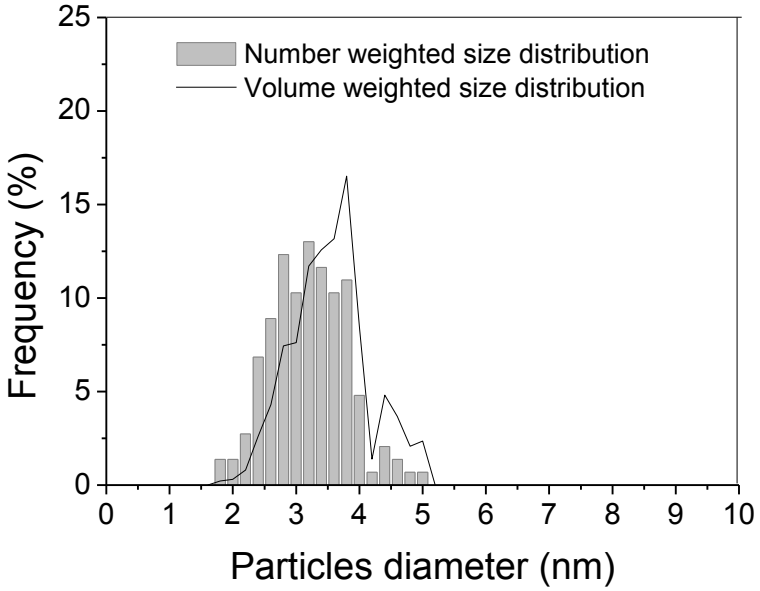

Figure 21. Pt particles size distribution (histogram).

The X-ray diffraction pattern is consistent with that given in the JCPDS reference 004 – 0802 (cubic Fm – 3m) with broadened peaks expected for nanoparticles (Figure 22). The crystallite size was calculated with the Scherrer formula[28]. The crystallite size of the Pt nanoparticles of 3.6 nm in average was calculated from the peaks matching the Miller planes [111], [200] and [220]. The details of the calculations are summarised in the Experimental Annex (paragraph E.3).

The X-ray diffractogramm pattern of niobium carbide NbC (ref 038 – 1364 cubic Fm – 3m) is unchanged, showing that the electrocatalyst deposition does not affect the crystalline structure of the support.

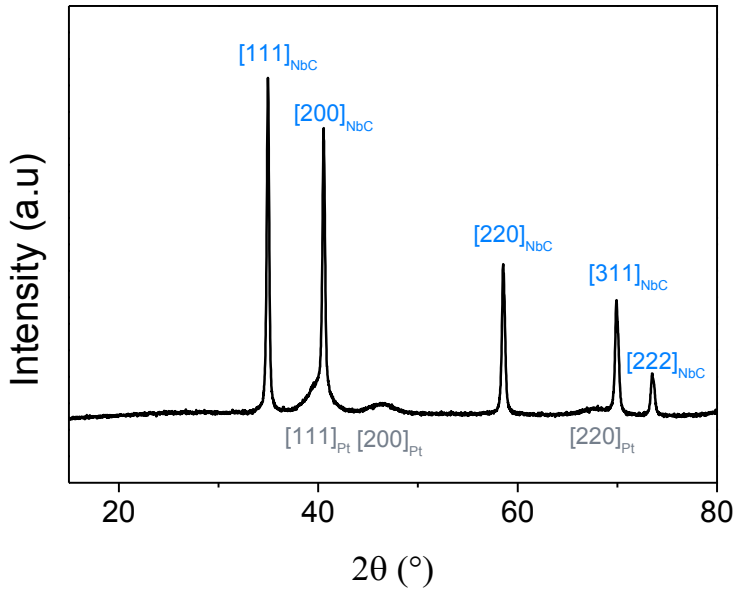

Figure 22. X-ray diffractogramm of the Pt catalysed NbC nanostructures.

A homogeneous dispersion of the particles onto the NbC nanostructures was observed by BE - SEM (Figure 23) and TEM (Figure 20, Figure 24 and Figure 25). Pt particles were also deposited on the NbC microspheres (Figure 25).

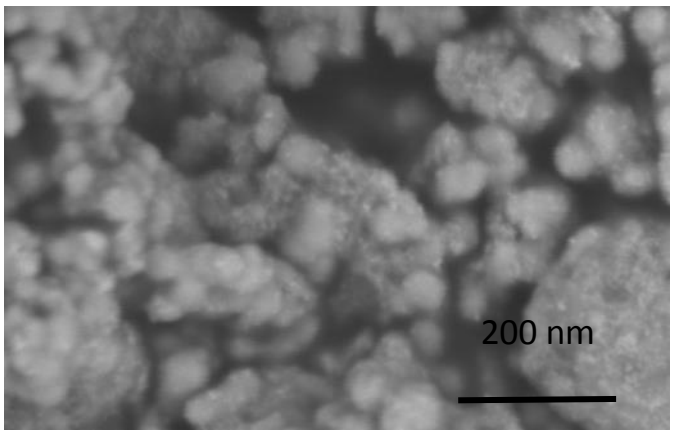

Figure 23**.** High resolution BE-SEM micrographs of the Pt/NbC nanostructures.

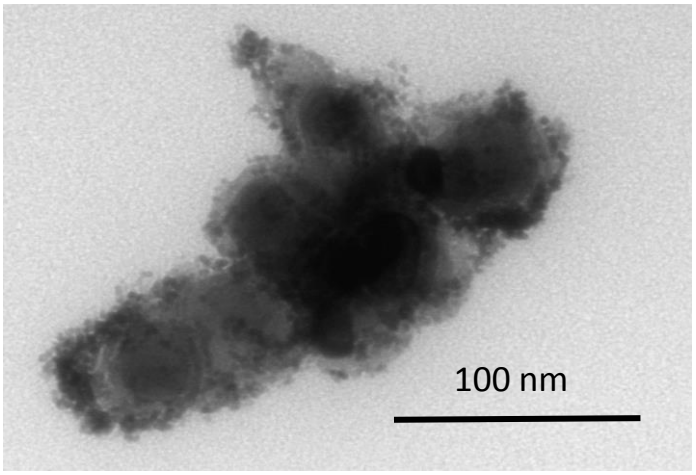

Figure 24. TEM micrographs of the NbC nanostructures catalysed with Pt nanoparticles.

Figure 25. TEM micrographs of Pt nanoparticles deposited ate the surface of vestige of a NbC microsphere.

Platinum loading was evaluated by X-ray fluorescence by using a calibration with standards prepared from commercial platinum black and niobium carbide. The NbC/C nanostructures (93/7 $\%_{wt}$) were loaded with 16 $\%_{wt}$ of platinum. This measurement was confirmed by energy dispersive X-ray analysis (EDX) coupled with SEM. When the synthesis was repeated, a slightly higher loading of 20 $\%_{wt}$ was reached.

Owing to the high density of niobium carbide (8 $g \cdot cm^{-3}$)[29] compared to that of carbon (2 $g \cdot cm^{-3}$ for graphite)[29], the platinum loading needs to be adapted to match a similar platinum loading in volume as for carbon supported platinum:

$$\%V = \frac{m_{Pt}/d_{Pt}}{m_{Pt}/d_{Pt} + m_{sup}/d_{sup}} \qquad \textbf{(2a)}$$

$$\%V = \frac{{}^{1}/_{d_{Pt}}}{{}^{1}/_{d_{Pt}} + {}^{1}/_{d_{sup}} \times {}^{(1-\%wt)}/_{\%wt}} \quad \textbf{(2b)}$$

%V = platinum loading in volume
$\%_{wt}$ = platinum loading in mass
m_{sup} = masse of support
d_{sup} = density of the support materials (2 $g \cdot cm^{-3}$)
m_{Pt} = masse of platinum
d_{Pt} = platinum density (21 $g \cdot cm^{-3}$)

For example a mass platinum loading of 50 $\%_{wt}$ for Pt/carbon corresponds to a volume loading of 8.7 $\%_{Vol}$ which matches a platinum loading of 20 $\%_{wt}$ for a Pt/NbC. As a consequence the 16 $\%_{wt}$ of Pt/NbC that was obtained corresponds to 40 $\%_{wt}$ Pt/C (that matches a volume loading of 6.96 $\%_{vol}$ for both chemical compositions).

D. Electrochemical characterisation of NbC nanostructures supported Pt on rotating disc electrode

The electrochemical characterisation was carried out in a 3-electrode cell (electrocatalyst loaded support as working electrode, reversible hydrogen electrode as reference electrode and Pt wire as counter electrode) and is divided in three parts respectively dedicated to the ECSA determination, the evaluation of the electrochemical stability and the measurement of the electrocatalytic activity towards ORR. Experimentally these electrochemical investigations consist on cyclic voltammetry that report the current matching the different electrochemical reactions that occur at particular potentials. The measurements were performed on a rotating disc electrode (RDE) in order to measure the limited diffusion current and isolate the kinetic current contribution. To evaluate the novel Pt/NbC electrocatalyst, each experiment was also performed on a reference commercial Pt/C (50 $\%_{wt}$) for comparison.

1. Electrochemical surface area

An ink was prepared so as to deposit a thin layer of catalysed support onto a rotating disc electrode. The catalysed materials were dispersed in a mixture of water and isopropanol and deposited onto the glassy carbon electrode. Because of the difference of morphology between Pt/NbC and Pt/C, different formulations were used so as to optimise the thickness and the homogeneity of the electrocatalyst layer on the electrode (setup described in the Experimental Annex).

Cyclic voltammetry was carried out at 50 $mV \cdot s^{-1}$ in N_2 saturated $HClO_4$ (0.1 M solution). In Figure 26 the current density is shown normalised by the amount of platinum on the electrode for a better comparison of the 2 catalysed supports. The three typical zones of a voltammogram of Pt in acidic medium may be identified:

1 - Hydrogen adsorption/desorption (reactions (3) and (4)) region in the potential range of 0.05 to 0.4 V vs RHE.

$$H^+_{(as)} + e^- + \text{Pt active site} \rightarrow \text{Pt} - \text{H} \quad \textbf{(3)}$$

$$\text{Pt} - \text{H} \rightarrow H^+_{(aq)} + e^- + \text{Pt active site} \quad \textbf{(4)}$$

2 - In the double-layer region only the capacitive processes take place.

3 - At high potential, an oxide layer is formed on the platinum surface from 0.8 V vs RHE. This PtO layer is reduced in the reverse sweep from 1.2 V to 0.6 V vs RHE.

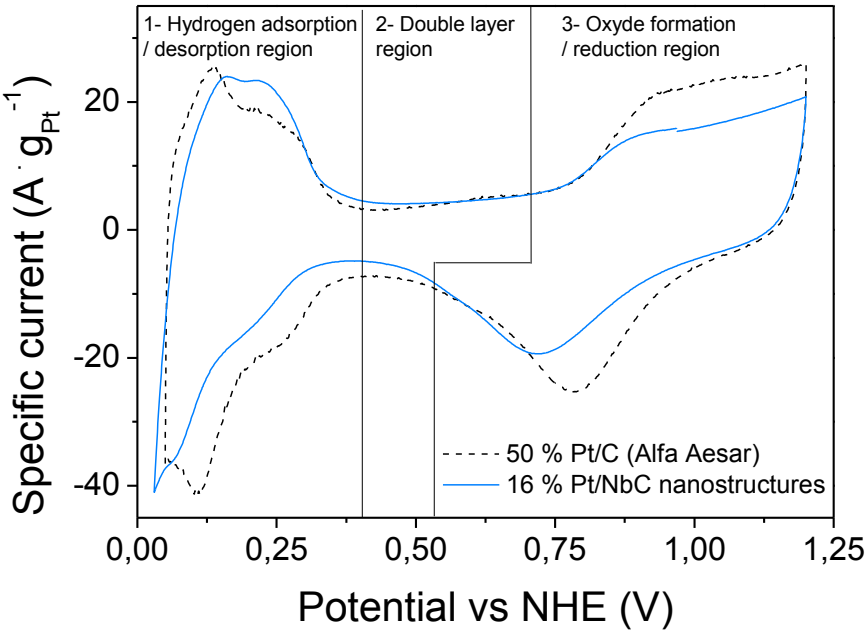

Figure 26. Cyclic voltammograms of the 16 % Pt/NbC supports and Pt/C 50 % in N_2 saturated $HClO_4$.

The hydrogen region is usually used to estimate the electrochemical surface area (ECSA) by integrating the hydrogen adsorption/desorption peak after subtracting the double layer region[30]. By assuming that the particles are randomly dispersed and that no planes are preferably available, the charge Q_{1cm2} matching the adsorption of one monolayer of hydrogen on 1 cm^2 of Pt is 210 µC[31,32]. The

ECSA of 16 % NbC nanostructures and of 50 % Pt/C were calculated using equation (5) by integrating the charge matching the adsorption of hydrogen on platinum on the voltammograms (Figure 26):

$$ECSA = \frac{integrated\ charge}{Q_{1cm^2} \times m_{Pt}} \quad \textbf{(5)}$$

ECSA = electrochemical surface area ($m^2 \cdot g^{-1}$)
integrated Charge = the charge matching the adsorption of hydrogen on active Pt sites
Q_{1cm2} = charge matching 1 cm^2 of Pt (210 $\mu C \cdot cm^{-2}$)
m_{Pt} = platinum mass on the electrode

ECSA of 16 $\%_{wt}$ Pt/NbC nanostructures was slightly lower than the ECSA of 50 $\%_{wt}$ Pt/C (42 $m^2 \cdot g^{-1}$ vs 52 $m^2 \cdot g^{-1}$). Although no information about the catalysation process used for the commercial 50 $\%_{wt}$ Pt/C was available to comment this difference, TEM observations shows a homogeneous dispersion of similarly sized Pt particles on the carbon support (Figure 27). The number and volume weighted average diameters measured from the TEM micrographs are similar to those of the 16 $\%_{wt}$ Pt/NbC nanostructures (respectively 3.4 and 3.8 nm vs 3.1 and 3.3 nm for the nanoparticles we synthesised).

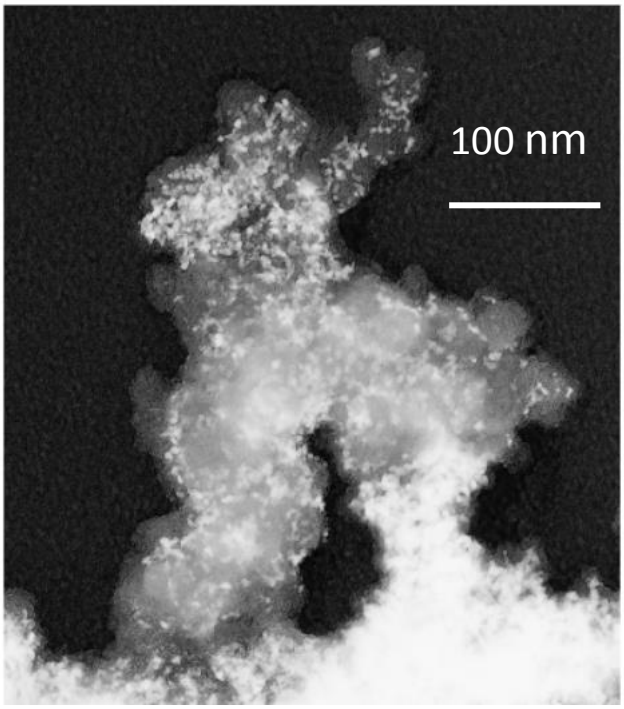

Figure 27. TEM micrograph of the 50 % Pt/C reference.

Considering the average diameter of the Pt particles in both cases, the expected ECSA should be higher. Indeed, if we approximate the cuboctahedral shape[33] of Pt particle as spherical we can calculate their surface area ($SA_{theoretical}$) using equation (6). With an average diameter of 3.3 nm, the theoretical electrochemical surface area for the Pt nanostructures would be 86 $m^2 \cdot g^{-1}$ while it would be 75 $m^2 \cdot g^{-1}$ for the 3.8 nm Pt particles of the reference Pt/C..

$$SA_{theoretical} = \frac{Surface}{Volume \times density} = \frac{4\pi r^2}{\frac{4}{3}4\pi r^3 \times d} = \frac{3}{d \times r} \quad \textbf{(6)}$$

Since the particles are supported, this calculation overestimates the ECSA. Morphological properties such as an unadapted microporosity could also explain the significant difference between the theoretical and experimental ECSA values.

2. Stability over time

During the past 10 years, numerous accelerated stress tests (AST) that have been developed to assess the durability of a fuel cell or its components[34]. They have been proven to be a valuable tool that significantly reduced the duration of experiments compared to steady state lifetime tests. They can be performed *in situ* or *ex situ* and provide with reliable results on lifetime evaluation and degradation mechanism[35].

This PhD work focuses on the PEMFC cathode. Therefore an AST has been conceived to corrode the electrocatalyst support *ex situ* so as to evaluate the durability of the Pt/NbC and compare it with Pt/C. In this AST, the ECSA is monitored during potential cycles as an indicator of the stability of the electrocatalyst on the support. Its degradation causes an ECSA loss that is reported as a proportion of the initial one. The AST consists on 10,000 electrochemical cycles between 0.6 V and 1.4 V vs RHE at 500 $mV \cdot s^{-1}$ (Figure 28). Every 100 cycles, two cycles were carried out at a slower rate of 50 $mV \cdot s^{-1}$ for ECSA monitoring. The ECSA loss is due to the degradation of the electrocatalyst support leading to particle detachment but also to the degradation of the electrocatalyst himself caused by the platinum particles evolution[36]. These mechanisms have been depicted in further details in the chapter I in the paragraph B.4.iii. The chosen potential is in agreement with the potentials recommended by the department of energy for similar electrochemical stability investigations. They recommend two different AST, targeting the specific investigation of the catalyst durability (0.6 to 1 V vs RHE) or the support durability (1-1.5 V vs RHE)[37]. The AST developed for this project combines them in order to reach the carbon corrosion, assess the electrocatalyst durability and highlight the electrostability of the synthesised alternative supports[38] compared to carbon based supports. Concerning the chosen scan rate of the AST, A report of several AST shows close agreement of dissolution rates per potential cycle with widely varying scan rates, indicating that the dissolution reaction is more dependent on the number of oxidation-reduction cycles rather than on the length of the cycle or time at oxidising potentials[35].

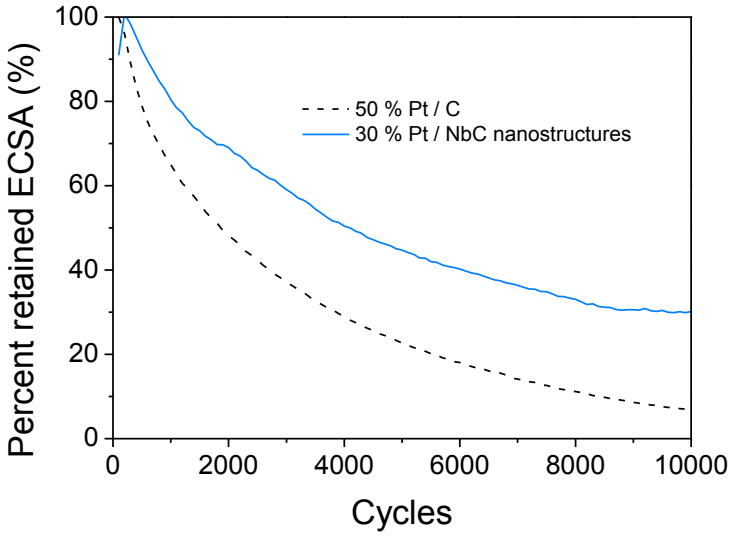

Figure 28. Stability of the ECSA of the catalysed supports during the accelerated stress test to 1.4 V.

Through this accelerated stress test, the ECSA of the Pt/NbC nanostructures and that of the commercial carbon based electrocatalyst feature a decay of 70 % and 95 % respectively (resulting in respectively 13 and 3 $m^2 \cdot g^{-1}$ as final ECSA), showing an improved stability of the synthesised support to electrochemical corrosion. It has to be noticed that this AST was performed on a second batch of Pt/NbC that led to a slightly different Pt loading of 20 $\%_{wt}$. This result suggests also that the low residual carbon amount and the Nb_2O_5 layer identified by XPS analysis (paragraph B.2) is not an issue concerning the stability of the NbC based support.

A preliminary AST consisting of 3,000 electrochemical cycling in a lower potential range (0.03 V and 1.2 V vs RHE) led to a more similar ECSA decrease for the Pt/C and Pt/NbC nanostructures (-28 % and 32 % respectively) (Figure 29). It can be noticed that WC hollow microspheres that were catalysed with similarly sized Pt nanoparticles (2.6 nm) displayed a similar stability (ECSA decrease of -15 % after 1,000 cycles) when investigated with an AST up to 1.25 V vs RHE. During this previous study, a commercial and an in house prepared Pt/carbon catalysed supports led to a 100 % loss after respectively 125 and 325 cycles. The difference between the results obtained during this two AST suggests that the platinum degradation (involving Pt detachment/coalescence/migration, Pt dissolution/reprecipitation and Ostwald ripening) was mainly responsible of the ECSA loss. With the AST to 1.4 V vs RHE, that focuses more on the support stability, the novel Pt/NbC nanostructures distance themselves from Pt/C.

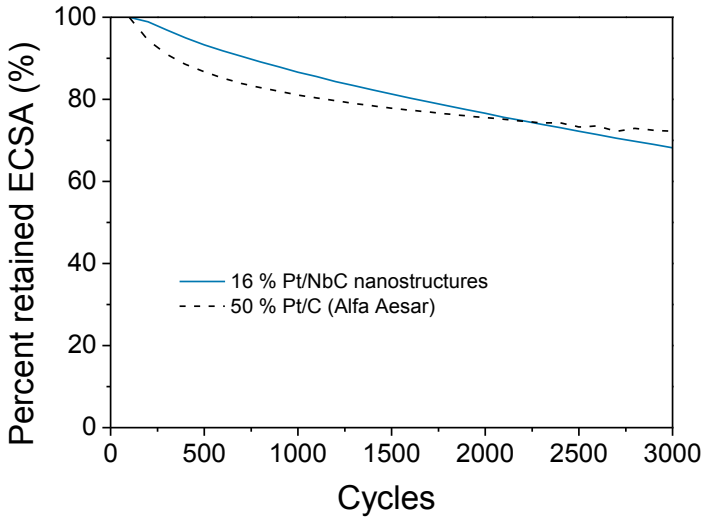

Figure 29. Stability of the ECSA of the catalysed supports during the accelerated stress test to 1.2 V.

This shows that the stability of the Pt/NbC nanostructures could be further improved by modifying the Pt based electrocatalyst. For instance *in situ* electrocatalyst depositions such electrodeposition are an alternative deposition that would provide with a stronger interaction between the electrocatalyst and the support. By targeting 2D Pt thin film, it would also contribute to extend the platinum surface area.

3. Activity towards the oxygen reduction reaction

As electrocatalyst support for the PEMFC cathode, Pt/NbC nanostructures have been evaluated for their activity towards the ORR. Figure 30 shows the linear sweep voltammogram obtained at 20 $mV \cdot s^{-1}$ in O_2 saturated in 0.1 M $HClO_4$ solution at 1600 rpm after the subtraction of the background obtained in N_2 saturated medium in the same conditions.

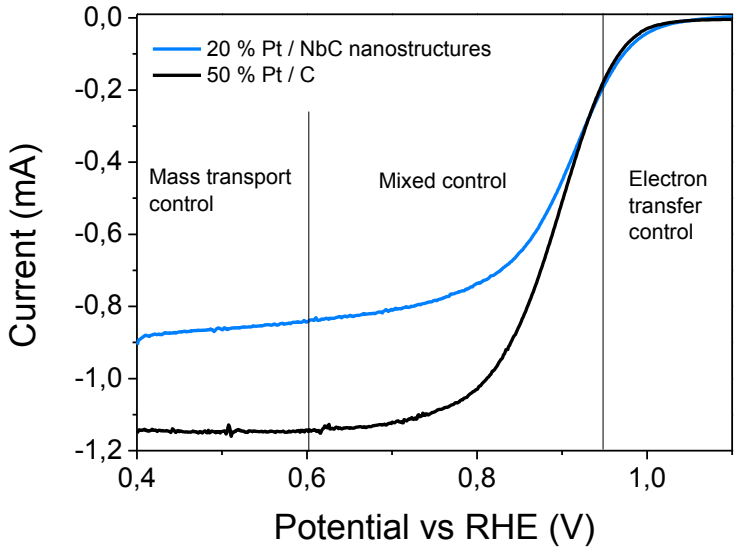

Figure 30. ORR voltammograms of the catalysed NbC nanostructures compared with commercial Pt/C at 1600 RPM.

The kinetic of oxygen reduction can be explained by two processes occurring for every electrochemical reaction in solution and determining its rate: electron transfer and mass transfer. Since the rate of the reaction is proportional to the current, the 2 regions can be differentiated on the curves (Figure 30) depicting the current as a function of the potential:

- At high potentials (0.85 – 1 V vs RHE) reaction rate is the limited by the electron transfer process.

- At low potentials (0.4 – 0.6 V vs RHE) the reaction is limited by the mass transfer process (in that case the amount of oxygen at the electrode).

The Levich equation[39] was used to isolate the current contribution matching the transfer process (I_k, kinetic current) from the current contribution due to the mass transfer process (I_d, diffusion limited current) (7):

$$\frac{1}{I_{tot}} = \frac{1}{I_k} + \frac{1}{I_d} = \frac{I_j I_d}{I_d - I_k} \quad \textbf{(7a)}$$

$$I_k = \frac{I_{tot} I_d}{I_d - I_{tot}} \quad \textbf{(7b)}$$

Kinetic current was used to calculate the mass activity in order to compare the catalytic activity of Pt/NbC nanostructures and Pt/C. A mass activity of 60 $A \cdot g^{-1}$ at 0.9 V vs RHE was calculated for the 20 % Pt/NbC nanostructures. This result is lower than the mass activity calculated for the 50 % Pt/C, 87 $A \cdot g^{-1}$ at 0.9 V (Figure 31). It has to be noticed that the activation heat treatment on the catalysed supports resulted in a 20 % mass activity increase that can be attributed to the complete removal of ethylene glycol.

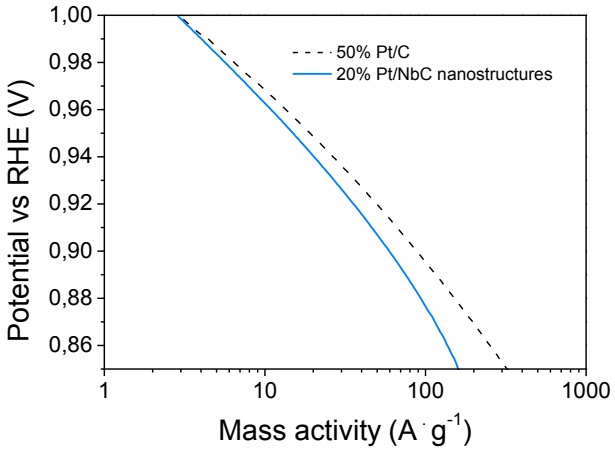

Figure 31. Tafel plot of the mass activity of 20 % Pt/NbC nanostructures vs Pt/C.

As explained in more details in paragraph 1.B.2.ii, the calculated slope of 59 $mV \cdot dec^{-1}$ is typical of platinum on carbon at low overpotentials (1 – 0.95 V vs RHE). This value is similar to a polycrystalline Pt in acidic media in a low current density range (In this conditions, the theoretical Tafel slope is 59 $mV \cdot dec^{-1}$)[30,40]. A similar slope was calculated for the Pt/NbC (68 $mV \cdot dec^{-1}$). For higher overpotentials (0.75 – 0.85 V vs RHE) a slope of 117 $mV \cdot dec^{-1}$ was calculated (at high current densities, Tafel slope usually rises to 120 $mV \cdot dec^{-1}$. As already discussed in the chapter I paragraph B.2.ii, this increase is usually attributed to a change in the nature of the adsorbed oxygen-containing species from the

solution in the Pt surface[41]. A more important increase of the Tafel slopes was observed for the Pt/NbC nanostructures at high overpotentials (142 $mV \cdot dec^{-1}$).

A different mechanism for the ORR catalysis would also be responsible of Tafel slopes differences. Thus the number of electrons exchanged during the reaction was investigated by using the equation (2) that expresses the diffusion-limited current of polarisation curves. The diffusion limited visible current in the Figure 30 can be expressed by the Koutecky Levich equation[42] (2) which allows estimating the number of electron involved in the kinetic of the reaction (Figure 32 and 33):

$$I_d = n\,B\,\omega^{\frac{1}{2}} \quad \textbf{(2)}$$

In which $B = 0.2\,m_{Pt}\,F\,D_{O_2}^{\frac{2}{3}}\,\nu^{\frac{-1}{6}}\,C_{O_2}$

m_{Pt} is the mass of platinum on the electrode, F is the faraday constant (96,485 $C \cdot mol^{-1}$), D_{O2} is the diffusion coefficient of O_2 in $HClO_4$ (1.93 10^5 $cm^2 \cdot s^{-1}$), ω the rotation speed of the RDE and ν the kinematic viscosity of the electrolyte (1.009 10^{-2} $cm^2 \cdot s^{-1}$), C_{O2} the bulk O_2 solubility (1.26 10^{-3} $mol \cdot L^{-1}$).

The polarisation curves were performed at different rotation speeds (400, 900, 1600, 2500 rpm) so as to plot the diffusion limited current versus the root square of the rotation speed (Koutecky Levich plot) (Figure 32).

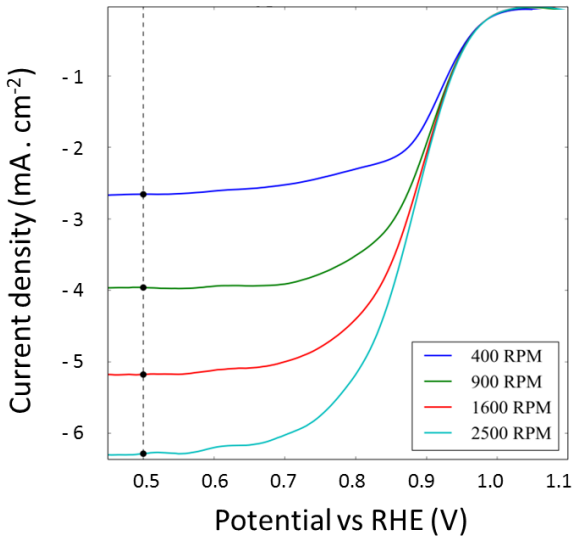

Figure 32. ORR voltammograms of the catalysed NbC nanostructures at 400, 900, 1600 and 2500 RPM.

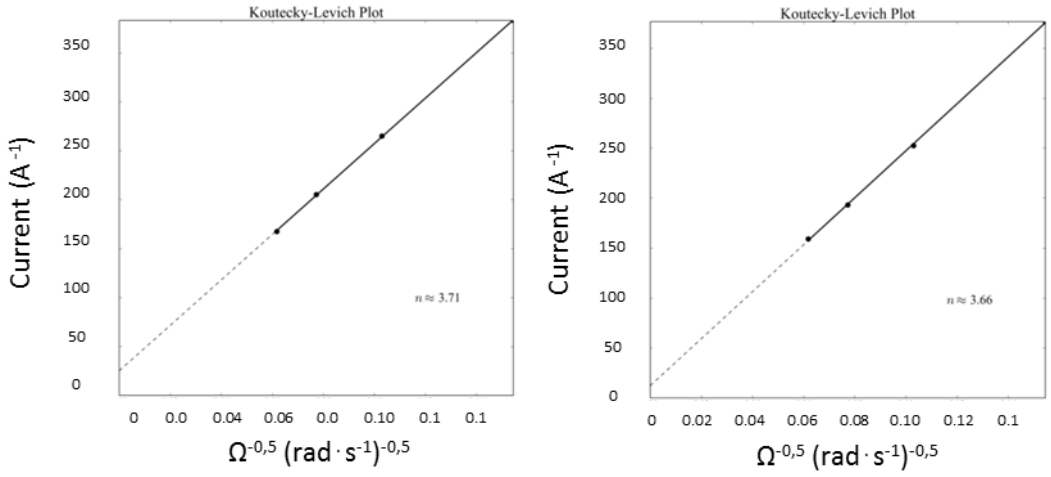

Figure 33. Koutecky Levich plots of the diffusion limited current at 2500, 1600, 900 and 400 rpm obtained with Pt/C and Pt/NbC nanostructures with the calculated number of electron involved in the ORR.

The Koutecky Levich plots were linear for both catalysed material, suggesting a first order dependence of the ORR on the Pt surface. The plot passed nearly through the origin, as expected for the diffusion-limited (Levich). The number of electrons calculated from the linear fit was similar for the Pt/NbC nanostructures and the Pt/C and confirmed the expected 4-electron mechanism.

Given the similar ECSA and ORR activity, it can be concluded that NbC nanostructures are a suitable material for the dispersion of Pt particles. The higher electrochemical stability of Pt/NbC at high potential (superior to 1.2 V vs NHE) confirmed the advantage of the use of an alternative material such as niobium carbide instead of conventional carbon support.

E. Conclusion and perspectives

1. Approach and method

The comparison of the synthesised catalysed Pt/NbC support with a commercial Pt/C confirms the approach that will be followed during this project. This synthesis route set the standard techniques for the characterisation of a NbC based material as electrocatalyst support (SEM, TEM, XRD, XPS, XRF, TGA, cyclic voltammetry). The developed microwave assisted polyol method led to Pt particles with a suitable diameter that will be used to catalyse all the supports synthesised during this PhD project. Furthermore the various physicochemical and electrochemical techniques that were carried out for the characterisation of the Pt/NbC nanostructures will be also performed on the other NbC based materials discussed in the following chapters. The electrochemical accelerated stress tests were well adapted to characterise the stability of the electrocatalysts, and the monitoring of the ECSA of the supported platinum particles.

2. A suitable composition and morphology to improve

A novel electrocatalyst support was successfully synthesised by associating a NbC composition with a low amount of residual carbon with a controlled morphology. This material gave an opportunity to confirm that the niobium carbide was suitable for the targeted application. Its electrical conductivity competes with that of carbon. The controlled morphology provides with specific surface area that can be tuned in the range of 60 – 80 $m^2 \cdot g^{-1}$ by adjusting the residual carbon amount. However, the obtained porosity was still mainly due to the microporosity of residual carbon and therefore is less favourable to obtain a suitable electrocatalyst dispersion.

The material was easily catalysed through Pt nanoparticles prepared by a microwave assisted polyol method. The same electrocatalysts were used for all the supports prepared in this PhD work so as to better compare them. Pt/NbC nanostructures feature a catalytic activity towards ORR that is only slightly lower than that of commercial Pt/C. Their stability through AST up to 1.4 V vs RHE was higher compared to Pt/C, suggesting that the low residual carbon amount or the Nb_2O_5 layer identified by XPS analysis do not affect negatively the stability of the catalysed NbC nanostructure.

To further study the influence of the morphology on the support properties, 1D nanostructured NbC have been prepared by electrospinning. These alternative morphologies together with new electrocatalyst deposition methods have been explored to further improve the stability of the PEMFC cathodes, and are reported in the following chapters.

F. References

1 L. Toth, *Transition metal carbides and nitrides volume 7*, 2014.

2 O. Dernovsek and J. Bressiani, *J. Mater. Sci.*, 2000, **35**, 2201–2207.

3 H. S. Kim, G. Bugli and G. Djéga-Mariadassou, *J. Solid State Chem.*, 1999, **142**, 100–107.

4 V. L. S. Teixeira da Silva, E. I. Ko, M. Schmal and S. T. Oyama, *Chem. Mater.*, 1995, **7**, 179–184.

5 J. Bernard D'Arbigny, G. Taillades, M. Marrony, D. J. Jones and J. Rozière, *Chem. Commun.*, 2011, **47**, 7950–7952.

6 Q. Wang, H. Li, L. Q. Chen and X. J. Huang, *Carbon N. Y.*, 2001, **39**, 2211–2214.

7 X. M. Sun and Y. D. Li, *Angew. Chemie-International Ed.*, 2004, **43**, 597–601.

8 V. L. S. Teixeira da Silva, M. Schmal and S. T. Oyama, *J. Solid State Chem.*, 1996, **123**, 168–182.

9 Engineers Edge, *thermal conductivity of gases chart*, 2015. (http://www.engineersedge.com/heat_transfer/thermal-conductivity-gases.htm)

10 H. G. Merkus, *Particle Size Measurements: Fundamentals, Practice, Quality*, Springer Science & Business Media, 2009.

11 J. Rouquerol, F. Rouquerol, P. Llewellyn, G. Maurin and K. S. W. Sing, *Adsorption by Powders and Porous Solids: Principles, Methodology and Applications*, 2013.

12 L. Ci, B. Wei, C. Xu, J. Liang, D. Wu, S. Xie, W. Zhou, Y. Li, Z. Liu and D. Tang, *J. Cryst. Growth*, 2001, **233**, 823–828.

13 G. G. Tibbetts, G. L. Doll, D. W. Gorkiewicz, J. J. Moleski, T. A. Perry, C. J. Dasch and M. J. Balogh, *Carbon N. Y.*, 1993, **31**, 1039–1047.

14 C. F. Miller, G. W. Simmons and R. P. Wei, *Scr. Mater.*, 2000, **42**, 227–232.

15 Z. Du, A. F. Sarofim, J. P. Longwell and C. A. Mims, *Energy & Fuels*, 1991, **5**, 214–221.

16 L. S. K. Pang, J. D. Saxby and S. P. Chatfield, *J. Phys. Chem.*, 1993, **97**, 6941–6942.

17 E. Puello-Polo and J. L. Brito, *J. Mol. Catal. A Chem.*, 2008, **281**, 85–92.

18 V. Schwartz and S. T. Oyama, *Chem. Mater.*, 1997, **9**, 3052–3059.

19 J. Moulder, W. Stickle, P. Sobol, K. Bomben, P. E. S. J. F. M. W.F. Stickle, J. Moulder, W. Stickle, P. Sobol, K. Bomben and K. D. B. J. F. M. W. F. S. P.E. Sobol, *Handbook of X-ray photoelectron spectroscopy*, Perkin Elmer Corporation, 1992.

20 M. T. Marques, A. M. Ferraria, J. B. Correia, A. M. B. do Rego and R. Vilar, *Mater. Chem. Phys.*, 2008, **109**, 174–180.

21 G. McGuire, G. Schweitzer and T. Carlson, *Inorg. Chem.*, 1973, **12**, 2450–2453.

22 E. H. Greener, D. H. Whitmore and M. E. Fine, *J. Chem. Phys.*, 1961, **34**, 1017.

23 F. Fievet, J. P. Lagier, B. Blin, B. Beaudoin and M. Figlarz, *Solid State Ionics*, 1989, **32**, 198–205.

24 I. Savych, J. Bernard d'Arbigny, S. Subianto, S. Cavaliere, D. J. Jones and J. Rozière, *J. Power Sources*, 2014, **257**, 147–155.

25 K. Wang, Z. Pan, F. Tzorbatzoglou, Y. Zhang, Y. Wang, T. Panagiotis and S. Song, *Appl. Catal. B Environ.*, 2015, **166**, 224–230.

26 H.-S. S. Oh, J.-G. G. Oh and H. Kim, *J. Power Sources*, 2008, **183**, 600–603.

27 E. Lebègue, S. Baranton and C. Coutanceau, *J. Power Sources*, 2011, **196**, 920–927.

28 A. Patterson, *Phys. Rev.*, 1939, **56**, 978.

29 J. Shackelford and W. Alexander, *CRC materials science and engineering handbook*, 2000.

30 S. Gojković, S. Zečević and R. Savinell, *J. Electrochem.*, 1998, **145**, 3716–3720.

31 H. Angerstein-Kozlowska, B. E. Conway and W. B. A. Sharp, *J. Electroanal. Chem. Interfacial Electrochem.*, 1973, **43**, 9–36.

32 B. E. Conway and H. Angerstein-Kozlowska, *Acc. Chem. Res.*, 1981, **14**, 49–56.

33 K. Kinoshita, *J. Electrochem. Soc.*, 1990, **137**, 845.

34 S. Zhang, X.-Z. Yuan, H. Wang, W. Merida, H. Zhu, J. SHEN, S. Wu and J. Zhang, *Int. J. Hydrogen Energy*, 2009, **34**, 388–404.

35 R. Borup, J. Meyers and B. Pivovar, *Chem. Rev.*, 2007, **107**, 3904–3951.

36 Y. Shao, G. Yin and Y. Gao, *J. Power Sources*, 2007, **171**, 558–566.

37 S. Kocha, Y. Garsany and D. Myers, *Testing Oxygen Reduction Reaction Activity with the Rotating Disc Electrode Technique*, 2013.

38 J. Wu, X. Z. Yuan, J. J. Martin, H. Wang, J. Zhang, J. Shen, S. Wu and W. Merida, *J. Power Sources*, 2008, **184**, 104–119.

39 A. Bard and L. Faulkner, *Electrochemical methods: Theory and applications*, John Wilney and Sons, 1980.

40 E. Gileadi and E. Kirowa-Eisner, *Corros. Sci.*, 2005, **47**, 3068–3085.

41 D. Walsh, A. Ejigu, J. Smith and P. Licence, *Phys. Chem. Chem. Phys.*, 2013, **15**, 7548–7554.

42 K. Kakinuma, Y. Wakasugi, M. Uchida, T. Kamino, H. Uchida, S. Deki and M. Watanabe, *Electrochim. Acta*, 2012, **77**, 279–284.

G. Table of Figures

Chapter III: Niobium carbide nanofibres as electrocatalyst support

A. Introduction

In a second part of the PhD project, our objective was to synthesis a niobium carbide with a nanofibrous morphology with a high surface area and a suitable porosity enabling an optimal electrocatalyst dispersion and gas accessibility[1]. Electrospinning (see chapter I paragraph C.3), was chosen for the synthesis of 1D NbC materials. Particular attention was paid to the elaboration of a synthesis route that could maintain the fibrous morphology from the electrospun precursors after thermal processing. The NbC mats were self-standing allowing the exploration of alternative electrocatalyst deposition methods.

Most of that routes reported for the synthesis of 1D nanostructured metal carbides[2–5] involve the preparation of the corresponding metal oxide that is subsequently reduced into carbide. For instance, the carburation at 1500 °C of Nb_2O_5 nanofibres obtained by electrospinning resulted in pure NbC nanofibres[4]. The synthesis delineated in this chapter follows a different pattern.

Composite nanofibres were prepared by electrospinning of a niobium precursor with a carrier polymer followed by a thermal treatment under inert atmosphere. The carbide was formed by direct carburation using the carrier polymer as carbon source. Polyacrylonitrile (PAN) has been chosen as carrier polymer for its high carbon yield (up to 56 %[6]) after stabilisation and carbonisation.

B. Synthesis and characterisation

1. Synthesis of niobium carbide nanofibres

Niobium chloride (10 $\%_{wt}$) was added to a dimethylformamide (DMF) solution of polyacrylonitrile. The resulting solution was electrospun onto a rotary drum target (Figure 1). The nanofibres with a narrow diameter distribution has been characterised by scanning electron microscopy (average value of 316 nm).

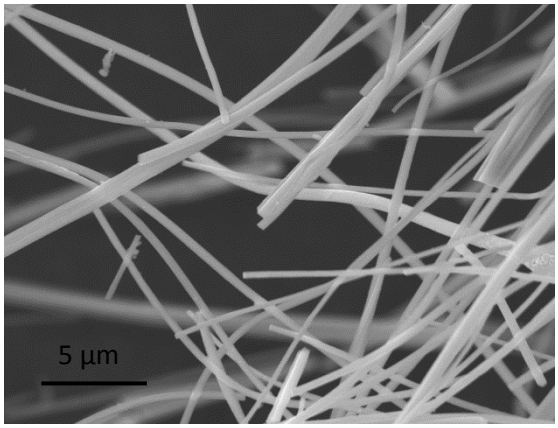

Figure 1. SEM micrograph of the electrospun material based on PAN and $NbCl_5$ displaying a fibrous morphology.

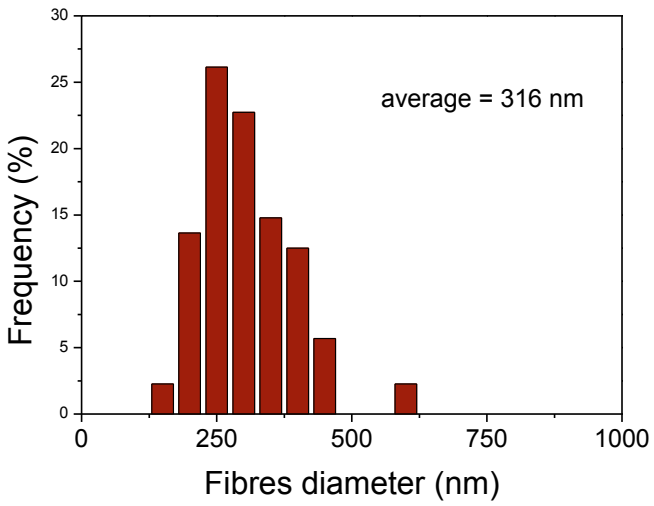

Figure 2. Diameter distribution of the as-prepared electrospun fibres.

The collected mat was directly carburated under argon at 1100 °C during 3.5 hours. The ramp of this heat treatment was optimised to improve the mechanical properties of the resulting self-standing

mat. A last step of methanation under hydrogen similar to the last step of the synthesis route to NbC/C nanostructures (chapter II paragraph B.1) was added to remove the carbon in excess.

The detailed parameters of the synthesis route are described in further details in Table 1 and in the Experimental Annex (paragraph C.2).

Table 1 Synthesis route details for the preparation of NbC nanofibres.

Step	Conditions
1. Electrospinning	PAN (7 $\%_{wt}$)/$NbCl_5$ (10 $\%_{wt}$) Solvent: DMF
2. Carburation	1h 150 °C → 1h 250 °C→ 3.5 h 1100 °C in air (0.5 °C min^{-1} / 0.5 °C min^{-1} / 5 °C min^{-1})
3. Methanation	1100 °C in H_2 (4 °C min^{-1})
4. Methanation	1100 °C in H_2 (4 °C min^{-1})

2. Structural, chemical and morphological characterisation of niobium carbide nanofibres

The chemical and structural composition of the PAN/Nb based electrospun material was characterised by powder X-ray diffraction after the carburation and methanation steps. The cubic phase of niobium carbide NbC (JCPDS reference 038 – 1364 cubic Fm – 3m) was clearly identified as the only crystalline phase (Figure 4). However the NbC phase was already present after the carburation step as evidenced by X-ray diffraction pattern (Figure 3). Carburation directly converts the PAN/$NbCl_5$ composite to niobium carbide, while methanation is needed only to remove the excess carbon.

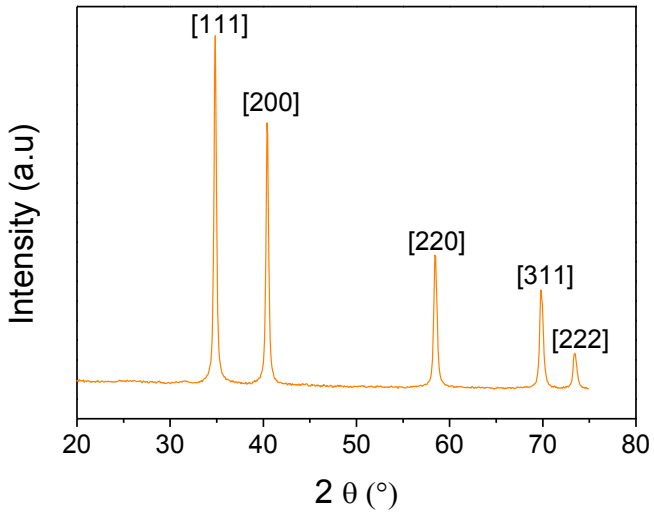

Figure 3. X-ray diffractogramm of the NbC nanofibres after carburation.

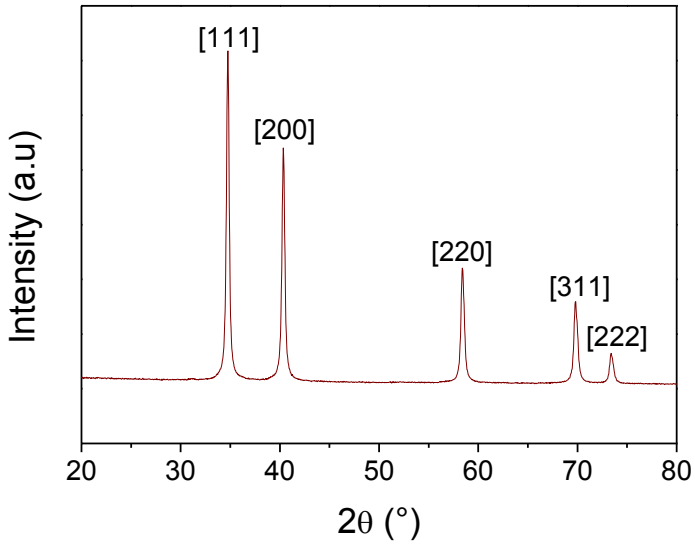

Figure 4**.** X-ray diffractogramm of the NbC nanofibres after methanation.

The crystallite sizes were calculated using the Scherrer formula for the Miller planes ([111], [200] and [220]) leading to respectively 12 nm, 12 nm and 19 nm for the nanofibres after carburation and 28, 24 and 25 nm for the nanofibres after methanation. This crystallite size increase is consistent with the grain growth caused by prolonged heat treatments.

PAN used as carbon source lead to residual carbon. The latter gave no visible X-ray diffraction pattern but needed to be quantified. Thermogravimetric analysis was used as discussed in chapter II paragraph B.2 (Figure 5) to determine the residual carbon content.

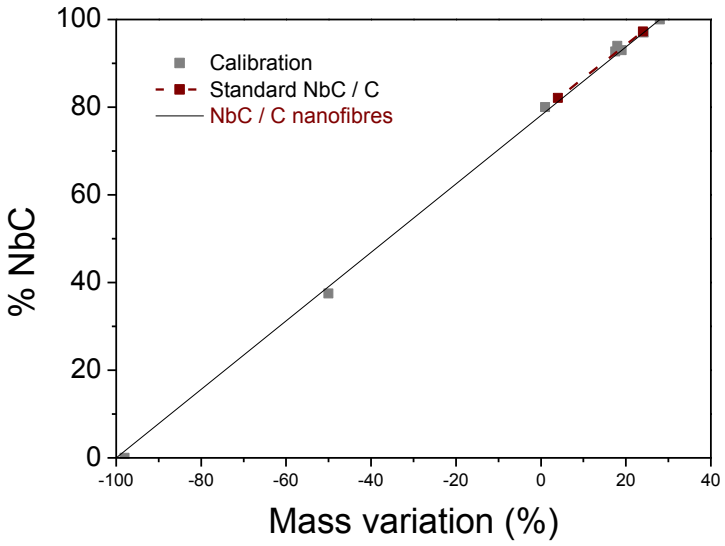

Figure 5. Calibration curve for the determination of NbC and carbon content obtained by TGA.

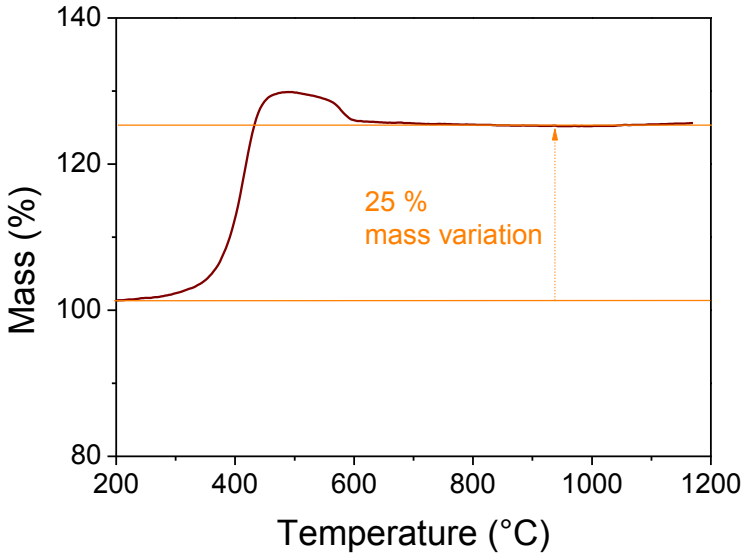

Figure 6. Thermogravimetric analysis of electrospun NbC.

While the nanofibres obtained after direct carburation contain 18 $\%_{wt}$ of residual carbon, a further step of methanation (step 4) and longer period were used to lower the residual carbon content to 3 $\%_{wt}$ (Figure 6). As for the NbC/C nanostructures this value was confirmed by CHNS elemental analysis. The CHNS elemental analysis was also used to investigate the nitrogen content of the NbC nanofibres that was inferior to 1 $\%_{wt}$. The last methanation step (step 4) was effective to remove most of the excess carbon.

After the carbon removal, the obtained materials were not self-standing anymore. The duration of the methanation was then adjusted to obtain the best compromise between the mechanical strength

and the low carbon content composition (10 $\%_{wt}$). Thus the material obtained after 1 methanation of 6 hours was selected for further analysis and characterisation. Furthermore carbon may act as binder between the NbC grains improving the flexibility of the mat.

Nb_2C or metallic Nb could also be formed during the prolonged heat treatments under reducing atmosphere. X-ray photoelectron spectroscopy was then carried out in order to verify the composition of the treated materials.

The high resolution XPS spectrum of the Nb region obtained for the nanofibres after methanation is shown in Figure 7. The peaks of 3d Nb orbital are fitted by two doublets corresponding to NbC (Nb $3d_{5/2}$= 204.07 eV and Nb $3d_{3/2}$ 206.79 eV) and Nb_2O_5 (Nb $3d_{5/2}$= 207.17 eV and Nb $3d_{3/2}$ 209.89 eV). These values match the theoretical values[7] (Nb $3d_{5/2}$= 203.7 eV for NbN[89] and Nb $3d_{5/2}$= 207.2 eV for Nb_2O_5)[10]. As it was observed and discussed for the NbC nanostructures (chapter II in the paragraph B.2), Nb_2O_5 was identified with a proportion of 64 $\%_{wt}$. Considering that XPS is a surface analysis and that Nb_2O_5 was not evidenced by XRD, it can be assumed niobium oxide is present only at the surface of the nanofibres as a thin layer. The presence of Nb_2C and metallic niobium was not observed confirming that the NbC was not further reduced during the methanations.

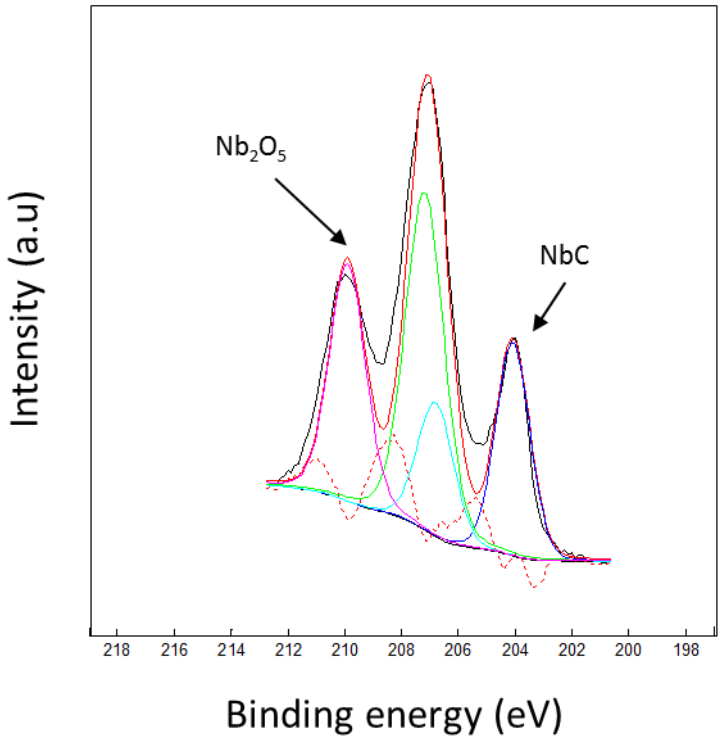

Figure 7. HR XPS spectrum of NbC/C material obtained after methanation (Nb 3d region).

3. Morphological characterisation of niobium carbide nanofibres

The SEM and TEM observations show that this 1D morphology was retained after the heat treatments steps (Figure 8, Figure 10, Figure 11 and Figure 12).

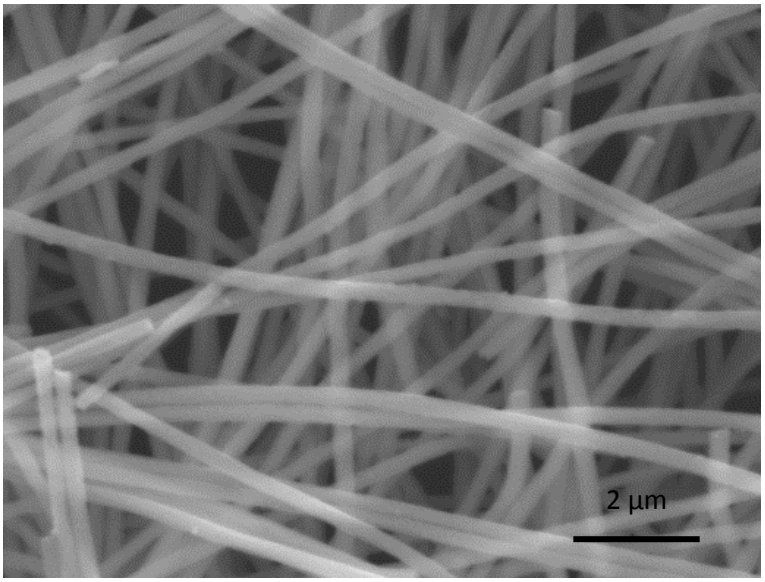

Figure 8. SEM micrograph of NbC nanofibres after methanation.

The NbC nanofibres obtained after methanation have a diameter distribution (Figure 9) between 200 nm and 600 nm with an average of 390 nm which is 25 % higher than the diameter measured directly after electrospinning (Figure 2). This diameter evolution can be explained by the NbC grain growth that occurs during the treatments at high temperature.

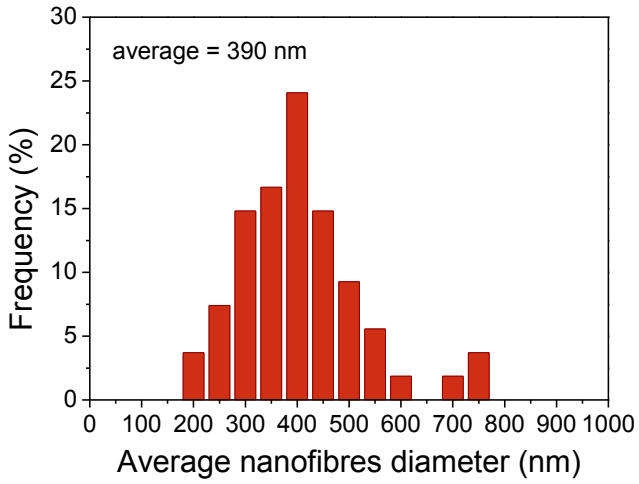

Figure 9. Diameter distribution of NbC nanofibres after methanation.

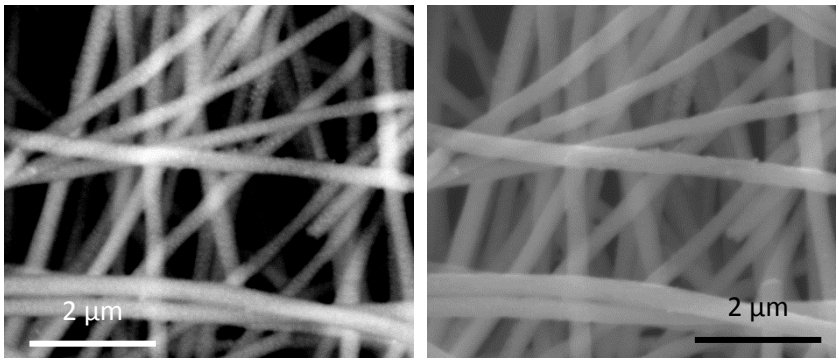

Figure 10. SEM micrograph of the NbC nanofibres displaying the NbC grains in NbC/C matrix (secondary electron (right) vs backscattered electron (left)).

Some fibres with a double or more sized diameter suggest that the heat treatment can result in the welding of nanofibres (Figure 12).

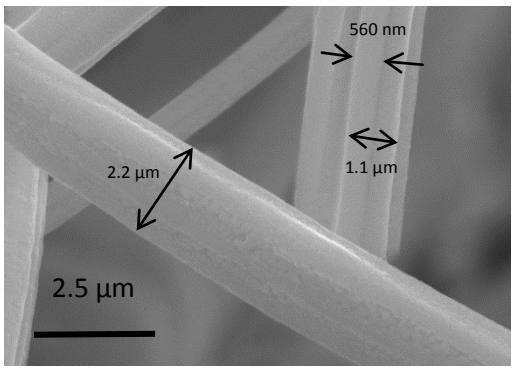

Figure 11. SEM micrograph of merged NbC fibres.

TEM observations highlight the structure of the nanofibres. Niobium carbide grains seem to be encapsulated in a carbon matrix (Figure 12). The size distribution of the niobium carbide grains composing the nanofibres is wide (Figure 13) (with an average of 23 nm). This value is in the range of the crystallite size calculated with the Scherrer formula (paragraph B.2).

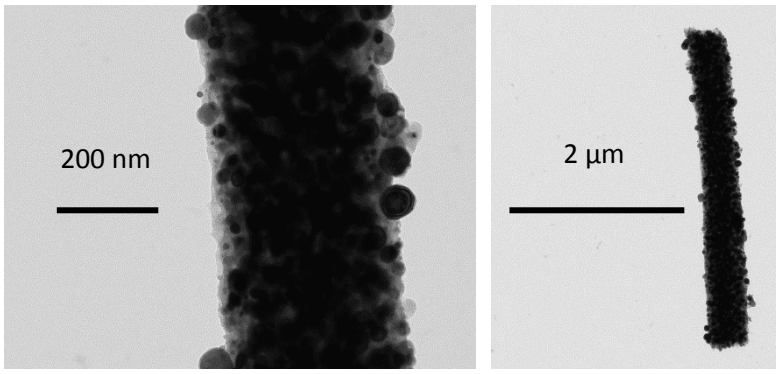

Figure 12. TEM micrographs of the NbC nanofibres.

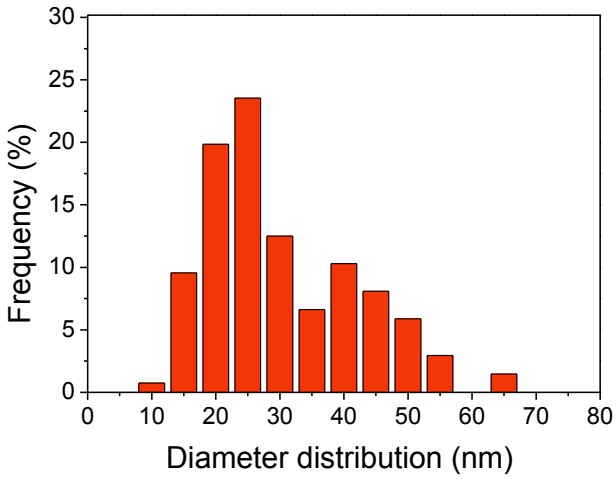

Figure 13. Size distribution of the NbC grain composing the nanofibres.

This nanostructure of NbC fibres with carbide grains embedded into residual carbon could explain their good mechanical properties making the mat self-standing.

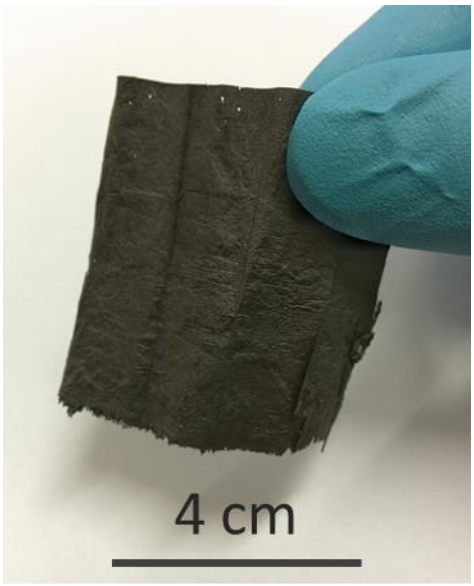

Figure 14. Self-standing mat of NbC nanofibres.

In order to compare the porosity of the NbC nanofibres with that of NbC nanostructures, nitrogen adsorption/desorption was performed. The nitrogen adsorption/desorption isotherm is of type IV with an H4 hysteresis loop (according to the IUPAC classification) (Figure 15). These types of isotherm is generally observed with complex materials containing both micropores and mesopores[11]. The calculated surface area is 80 $m^2 \cdot g^{-1}$ which is higher than that measured for smooth nanofibres with the same diameter[12]. Defects provided by the niobium grains could also contribute to the developed surface compared to smooth fibres and could be beneficial in term of electrocatalyst adhesion[13]. This phenomena was observed on Nb doped SnO_2 loose-tube nanofibres with a similar "grain like structure" that featured higher surface area (50 vs 20 $m^2 \cdot g^{-1}$) than undoped smooth SnO_2 nanofibres[14].

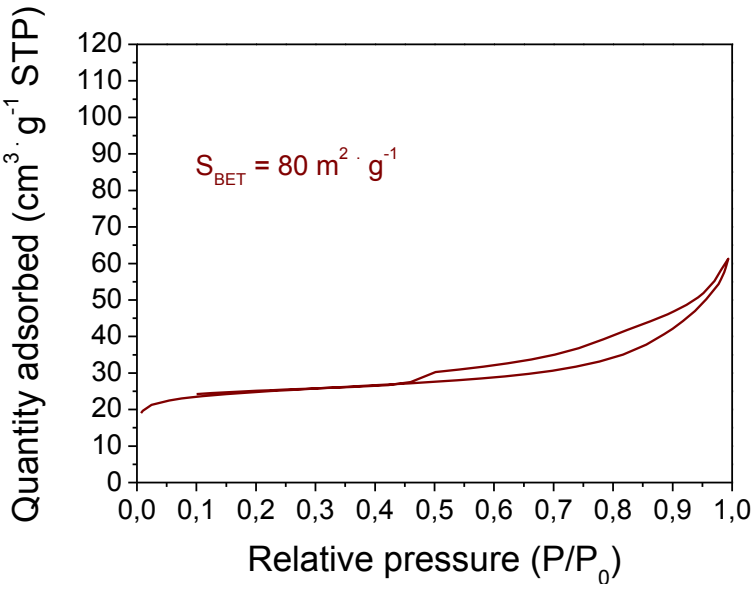

Figure 15. Nitrogen adsorption/desorption of NbC nanofibres.

C. Synthesis and characterisation of Pt supported on NbC nanofibres

1. Synthesis of Pt supported on NbC nanofibres

NbC nanofibres have been catalysed with platinum nanoparticles synthesised by the microwave assisted polyol method already described in chapter II paragraph C.1. Pt deposition was performed to reach a 35 $\%_{wt}$ platinum loading as already described for Pt/NbC nanostructures. Further experimental details are provided in the Experimental Annex (paragraph D.1).

2. Physico-chemical characterisation of Pt supported on NbC nanofibres

TEM observation showed good distribution of platinum particles onto NbC nanofibres (Figure 16). The platinum particles seem to cover the surface of the NbC nanofibres.

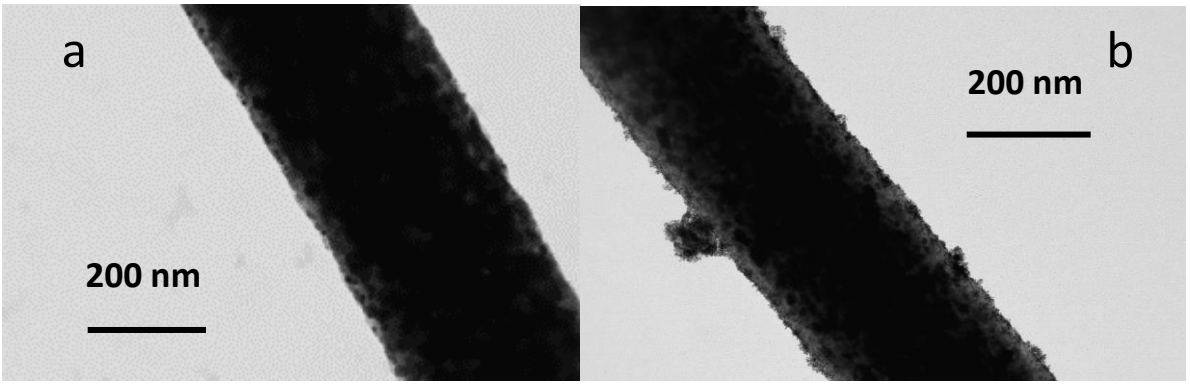

Figure 16. TEM micrograph of 15 $\%_{wt}$ Pt/NbC nanofibres before (a) and after (b) the Pt particles deposition.

TEM analysis was also performed on microtomed cross sections to confirm this observation. The platinum particles were also detected in the inner porosity of the nanofibres (Figure 17).

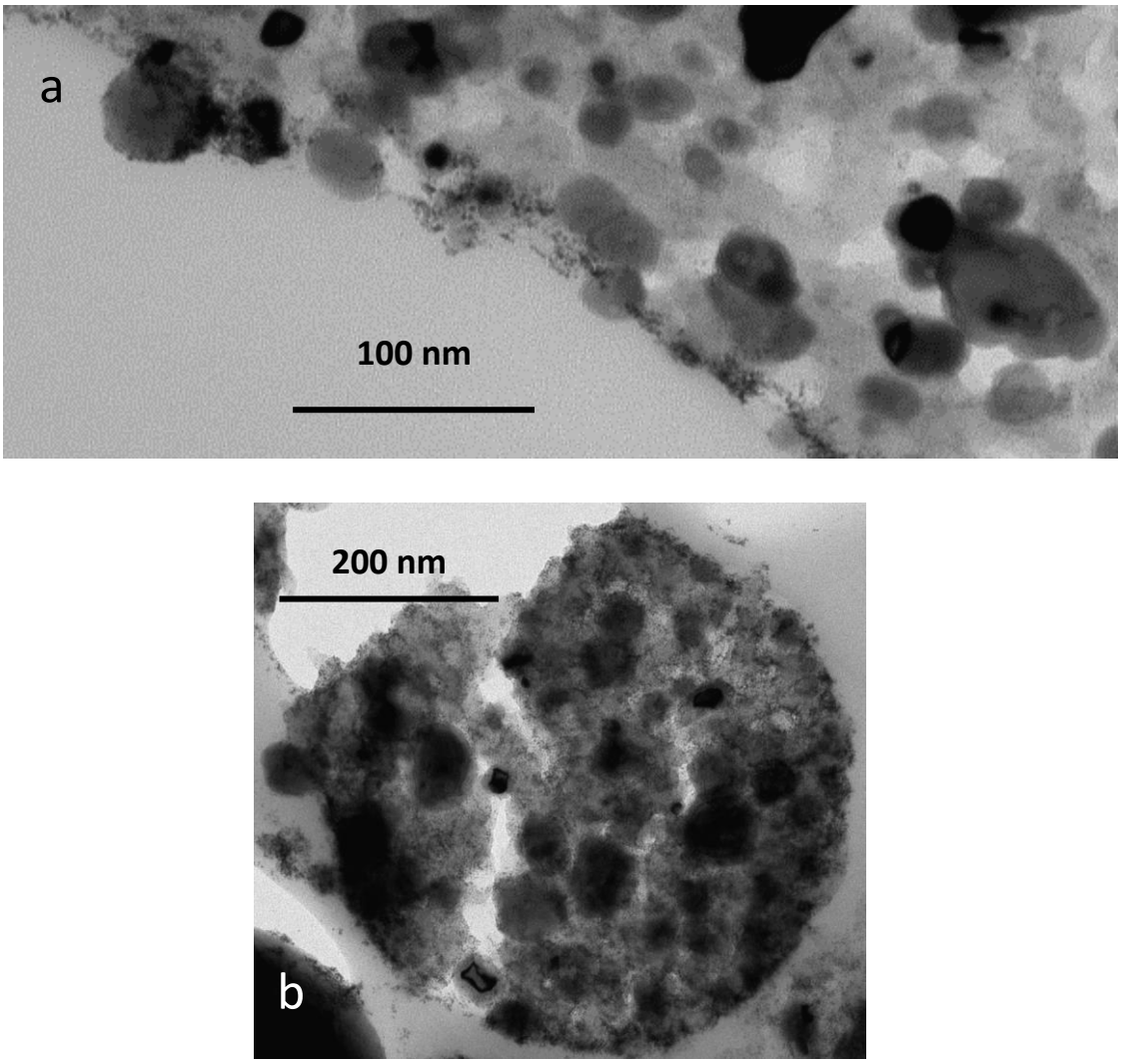

Figure 17. TEM micrograph of a microtomed section of 15 $\%_{wt}$ Pt/NbC nanofibres: transversal (a) and longitudinal (b) views.

The platinum loading on the NbC material has been evaluated by X-ray fluorescence (and further confirmed by scanning electron microscopy – energy dispersive X-ray spectroscopy (SEM-EDX). The loading was estimated in the range of 15 – 20 $\%_{wt}$. The large difference with the expected loading of 35 $\%_{wt}$. is an indication that there is a limit in the loading which can be reached owing to the surface area and the surface defects of the NbC nanofibres. This loading is lower than that which can be achieved on carbon black with specific surface areas from 250 $m^2 \cdot g^{-1}$ (Vulcan)[15] to 780 $m^2 \cdot g^{-1}$ Ketjen black EC-300[16]. Specific surface areas of carbon supports are usually higher than that of the NbC nanofibres. Nevertheless, a 15 $\%_{wt}$ loading of platinum is comparable to a 38 $\%_{wt}$ loading on a conventional carbon support taken in account the mass difference between the different atoms.

D. Electrochemical characterisation of NbC nanofibres supported Pt on rotating disk electrode

1. Electrochemical surface area

The *ex situ* electrochemical characterisation was performed on rotating disk electrode on the 15 $\%_{wt}$ Pt/NbC nanofibres and commercial 50 $\%_{wt}$ Pt/C (Alfa Aesar) for comparison. The ink formulations for the RDE as well as the procedure of the electrode preparation are described in the Experimental Annex (paragraph E.8). For comparison with a Pt/C reference electrode, the results were normalised by dividing by the platinum mass per electrode ($A \cdot g^{-1}_{Pt}$).

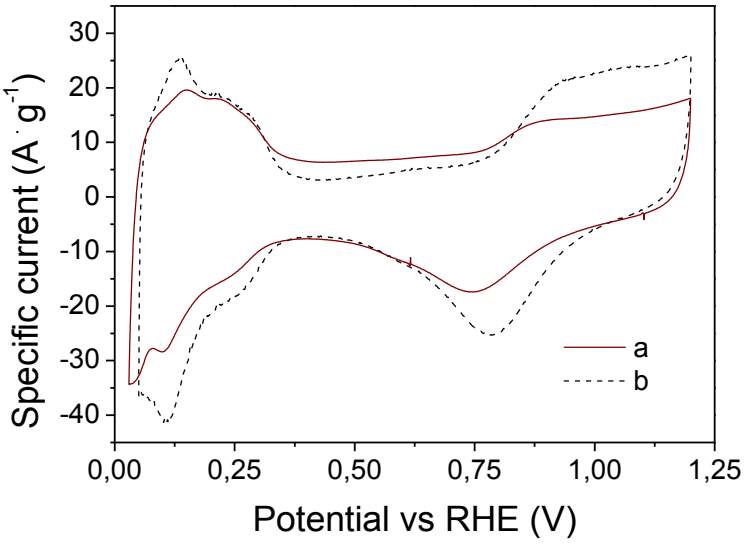

Figure 18. Cyclic voltammograms of 15 % Pt/NbC nanofibres (a) and 50 % Pt/C (b) in N_2 saturated $HClO_4$ (Alfa Aesar).

Cyclic voltammetry in N_2 saturated $HClO_4$ performed on the Pt/NbC electrode (Figure 18), shows the typical features of Pt surface (see chapter II paragraph D.1).

Platinum electrochemical surface area (ECSA) calculated by integrating the hydrogen adsorption peak was 26 $m^2 \cdot g^{-1}$. This value is significantly lower than the ECSA of 52 $m^2 \cdot g^{-1}$ obtained for the 50 $\%_{wt}$ Pt/C (Alfa Aesar) suggesting that a part of the platinum was isolated from the electrolyte. It can be assumed that the platinum particles deposited on the inner porosity of the NbC nanofibres are not active because non accessible.

2. Stability in time

The stability in time of the catalysed nanofibres was investigated by monitoring their ECSA every 100 cycles during the two accelerated stress tests previously described:

a – A preliminary AST consisting on 3,000 electrochemical cycles at 500 $mV \cdot s^{-1}$ between 0.03 V and 1.2 V vs RHE (Figure 19a).

b - A High potential AST consisting on 10,000 electrochemical cycles at 500 $mV \cdot s^{-1}$ between 0.6 V and 1.4 V vs RHE (Figure 19b).

Table 2 provides a summary of the initial ECSA and its loss after the two accelerated stress tests. The ECSA variations as a function of the number of cycles are depicted in Figure 19. After 3,000 cycles up to 1.2 V vs RHE, the ECSA decrease for the Pt/NbC nanofibres, was 20 % versus the 25 % for Pt/C.

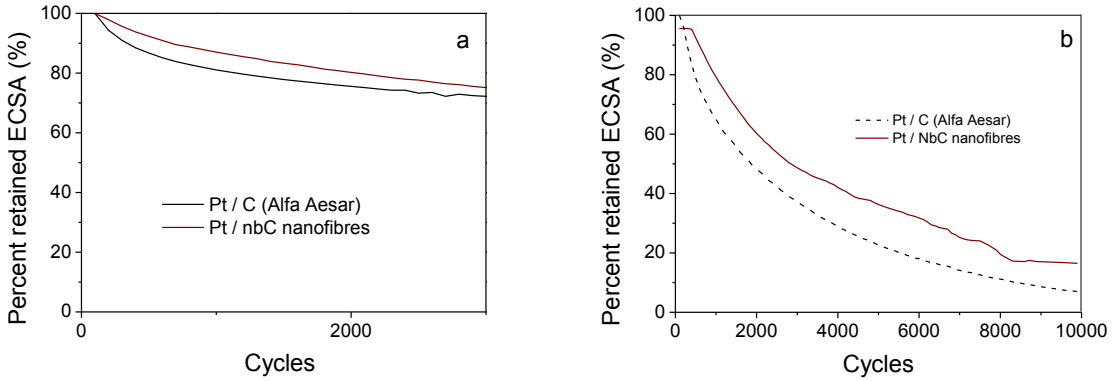

Figure 19. ECSA of the catalysed supports as a function of cycles during the accelerated stress test to 1.2 V (a) and to 1.4 V (b).

Table 2 initial ECSA and ECSA loss during the accelerated stress test to 1.4 V and 1.2 V.

	Pt loading *(%)*	***Initial ECSA*** *(m^2/g)*	***ECSA loss after 3000 cycles up to 1.2 V***	***ECSA after 3000 cycles up to 1.2 V*** *(m^2/g)*	***ECSA loss after 10000 cycles up to 1.4 V***	***ECSA after 10000 cycles up to 1.4 V*** *(m^2/g)*
Pt/NbC nanofibres	15	26	-20 %	21	-80 %	5
Pt/NbC nanostructures	20	42	-32 %	29	-70%	13
Pt/Carbon	50	52	-25 %	39	-95 %	3

The AST to 1.4 V vs RHE significantly degraded the Pt/NbC nanofibres and Pt/C electrode and their ECSA came respectively to 20 % and 5 % of the initial ECSA at the end of the test. This result indicates a higher stability for the NbC based support, as already illustrated by the Pt/NbC nanostructures (chapter II, paragraph 3.ii). A lower ECSA decrease is observed for the Pt/NbC nanofibres (-70 % vs -80 %) suggesting that the residual carbon content has an effect on the stability of the catalysed support.

3. Activity towards the oxygen reduction reaction

The catalytic activity of 20 $\%_{wt}$ Pt/NbC nanofibres towards the oxygen reduction reaction was investigated in the rotating disc electrode setup by linear sweep voltammetry in O_2 saturated $HClO_4$ 0.1 M solution. In Figure 20, the ORR polarisation curves of the catalysed NbC nanofibres and commercial 50 $\%_{wt}$ Pt/C are shown. The two curves present a similar onset potential of oxygen reduction at 1.05 V vs RHE and a similar diffusion limited current that matches the diffusion limited current (1.1 mA).

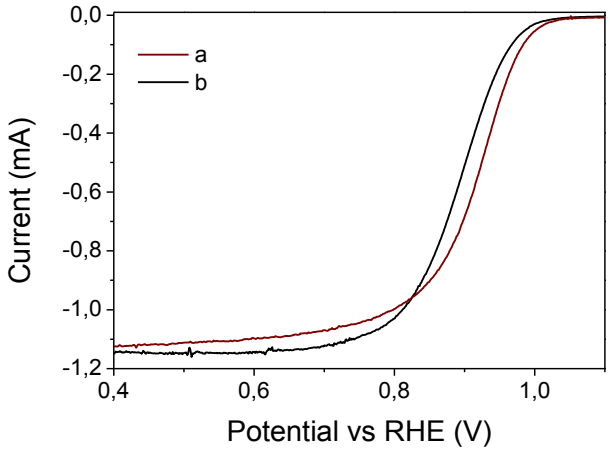

Figure 20. Linear sweep voltammetry in O_2 saturated $HClO_4$ 0.1 M solution of 20 % Pt/NbC nanofibres (a) and 50 % Pt/C (b) at 1600 rpm.

At 0.9 V the ORR mass activities calculated from the kinetic current are respectively 30 and 87 $A \cdot g^{-1}_{Pt}$ for 20 $\%_{wt}$ Pt/NbC nanofibres and 50 $\%_{wt}$ Pt/C. (Figure 21). As it was shown in previous studies[17,18], the mass activity declines with the decrease of ECSA of Pt. Therefore given the smaller ECSA of the Pt/NbC nanofibres compared to Pt/NbC nanostructures (26 vs 42 $m^2 \cdot g^{-1}$), a lower ORR mass activity is expected (30 vs 60 $A \cdot g^{-1}$). A Tafel slopes of 60 $mV \cdot dec^{-1}$ in the electron transfer control region for the two compared catalysed materials is shown in Figure 21.

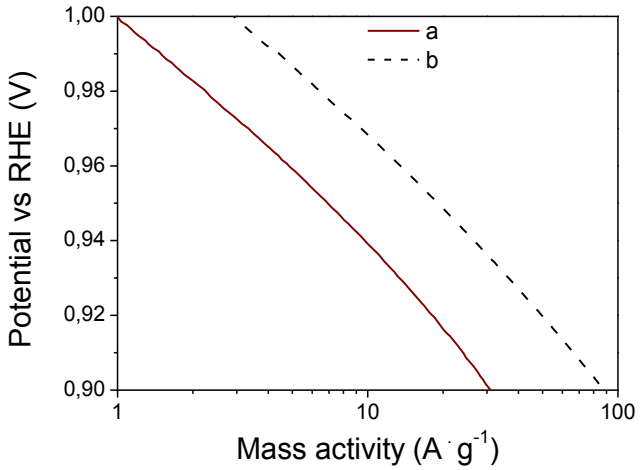

Figure 21. ORR Tafel plot for 20 $\%_{wt}$ Pt/NbC nanofibres (a) and 50 $\%_{wt}$ Pt/C (b).

Alternative deposition has been investigated so as to increase the stability and mass activity of the catalysed nanofibres. These methods and the electrochemical characterisation will be presented in the paragraph F.III.4.

E. *In situ* characterisation of Pt supported on NbC nanofibres

1. MEA Preparation

Most of the electrochemical characterisation of carbide based electrocatalysts[2,19,20] reported in the bibliography has been performed *ex situ* using rotating disk electrode. Although performance and electrochemical stability can be evaluated with RDE measurements on Pt/NbC, the preparation of a membrane electrode assembly (MEA) and the *in situ* characterisation in a single fuel cell are essential. An NbC cathode was obtained by spraying a hydro-alcoholic ink made with Nafion and Pt/NbC fibres onto a 4 cm^2 GDL. An MEA was made with this cathode, a PFSA membrane (Nafion 212 with a thickness of 50 µm) and a commercial Pt/C anode. The cathode and the anode have a Pt loading of 0.5 $mg_{Pt} \cdot cm^{-2}$. The thickness of the active layer is approximatively 15 µm.

2. Performance/Characterisation

The study of the Pt/NbC nanofibres based MEA was performed in a 4 cm^2 single PEMFC at 80 °C and 100 % RH (further details about the *in situ* characterisation are provide in the Experimental Annex in the paragraph C.3.iii). The polarisation curve is shown in Figure 22. The open circuit voltage is 938 mV and a power density of 465 $mW \cdot cm^2$ was reached at 1200 $mA \cdot cm^{-2}$ which confirms the observed low activity in RDE measurements.

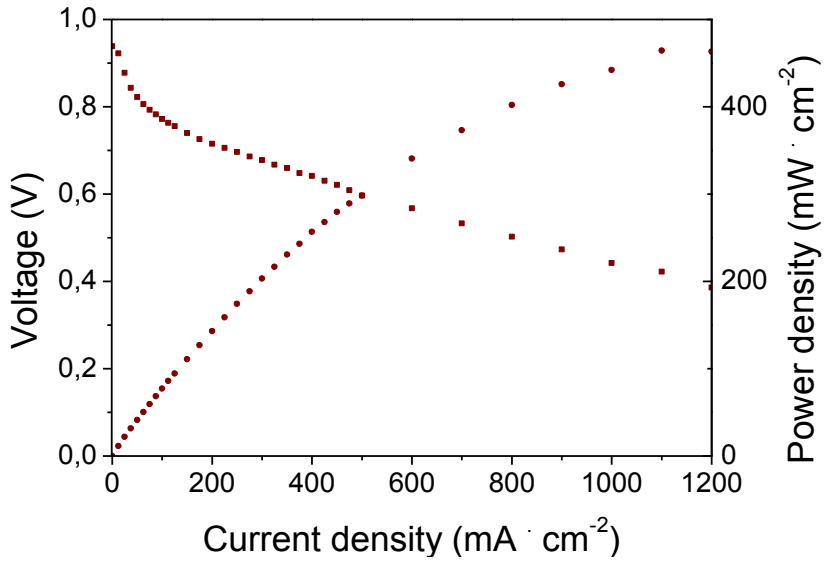

Figure 22. Polarisation curve for an MEA containing Pt/NbC nanofibres at the cathode (0.5 mg · cm^{-2}) T = 80 °C ; H_2/O_2 (1.5:2) 2 bar (abs); RH 100 %.

However no accelerated stress test was performed *in situ.* After several polarisation curves, a significant drop in performance has been observed (Figure 24). The MEA was dismounted from the cell following recording of the polarisations characteristics. As evidenced by a cross-section of this MEA after the characterisation (Figure 23), at the end of the fuel cell test the nanofibres retained their morphology however platinum particles looked not homogeneously distributed. Further investigations are required to understand the cause of this Pt agglomeration (ink preparation, issues related to the electrocatalyst adhesion onto the support, surface change in fuel cell condition).

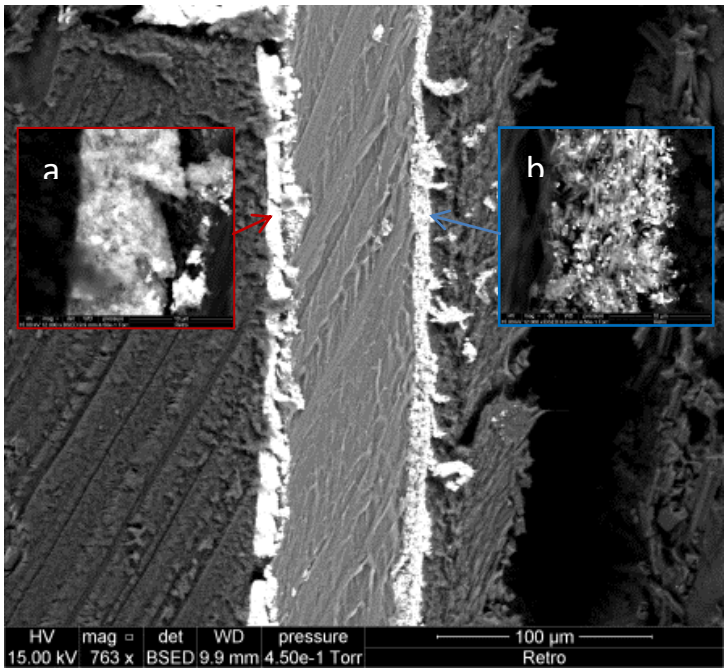

Figure 23. SEM micrograph of the membrane electrode assembly with Pt/C at the anode side (a) Pt/NbC nanofibres at the cathode side (b).

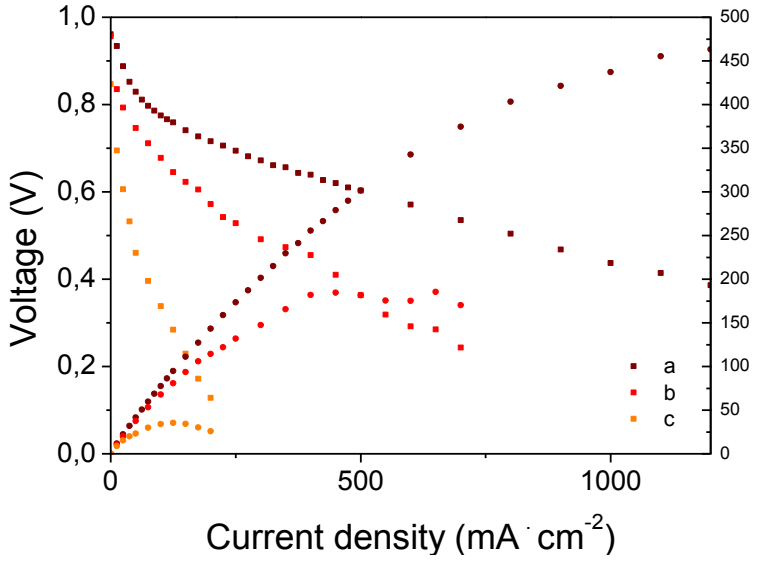

Figure 24. Polarisation curves after 12 h break in (a), after 24 h in operating conditions (b) and after 48 h in operating conditions (c) for the MEA containing Pt/NbC nanofibres at the cathode (0.5 mg · cm^{-2}) T = 80 °C ; H_2/O_2 (1.5:2) 2.0 bar (abs); RH 100%.

This preliminary test showed that the NbC nanofibres are suitable as electrocatalyst support in PEMFC cathode. Although further optimisations are required to reach the performance of commercial Pt/C electrode[21], promising results were obtained including a power density of 465 mW · cm^2.

F. Alternative electrocatalyst morphology: Pt film deposition

1. Introduction

Recent approaches have been developed in which platinum is deposited as thin, contiguous and conformal films, the so-called *extended platinum surfaces* for PEMFC applications. This 2D morphology minimises the surface of unused platinum as well as the contribution from edge and corner sites (coordinatively unsaturated) that occur in a conventional Pt nanoparticulate catalyst[22]. As illustrated by several examples in Figure 25 (nanostructured thin film catalyst developed by 3M[23], Pt nanotubes formed by chemical vapour deposition by Papandrew et al.[26] and a reference of Pt on carbon with high surface area[27]), these approaches are providing for a much higher ORR specific activity than is possible with the conventional 3 – 4 nm particulate catalysts[23–25]. As long as a sufficiently thin coating can be deposited, such that the platinum mass based surface area is high enough, then it will be possible to increase mass activity significantly beyond that which is possible with just further development of the current nanoparticulate approach[28,29].

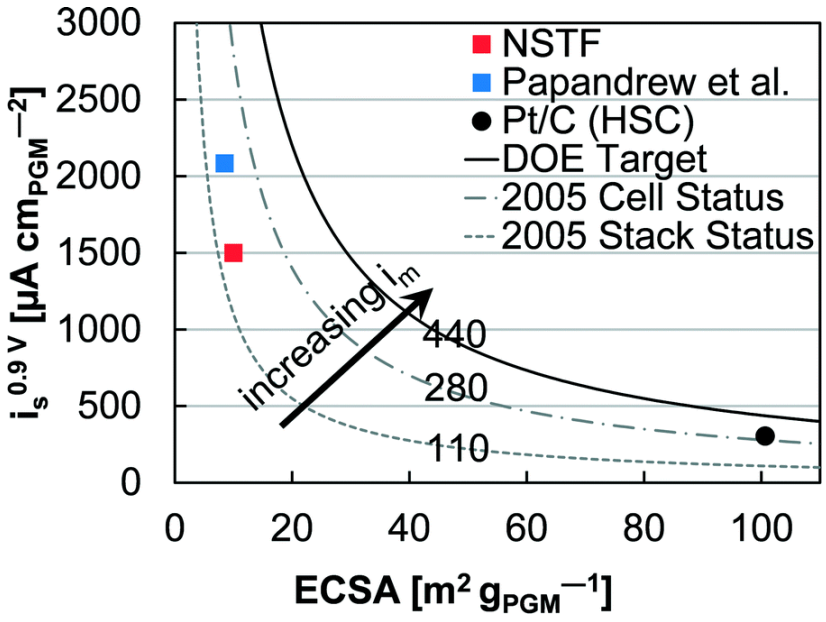

Figure 25. Surface area and specific ORR activity of nanostructured thin film catalyst developed by 3M[23], Pt nanotubes formed by chemical vapour deposition by Papandrew et al.[26] and a reference of Pt on carbon with high surface area[27]. The numbers on the 2005 PEM fuel cell status and DOE target lines are the mass activities (i_m, mA mg_{PGM}^{-1}).

In addition to the specific and mass activities, platinum contiguous thin film electrocatalysts would be beneficial for the durability of the electrode[24]. The sintering would be energetically unfavourable and the oxide-dissolution mechanism leading to Pt loss would be also significantly reduced. A Pt shell

structure would also provide protection to the support preventing the corrosion of the residual carbon in the NbC nanofibres[25,30]. Furthermore thank to this 2D nanostructured film, platinum will form an "interconnected" network with the support that will make it less prone to detachment[31]. A schematic representation explaining the high activity and stability of Pt film electrocatalysts is depicted in Figure 26. This interconnected network will reduce the risk of ohmic loss[32] by increasing the contact surface area with the support and by assisting the electron transfer ensured by the substrate.

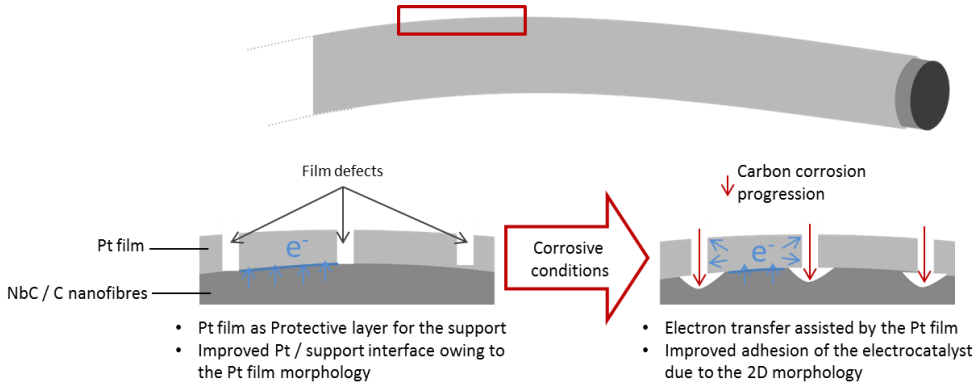

Figure 26. Schematic representation of the electron transfer and durability of Pt film electrocatalysts.

The preparation of NbC nanofibres was optimised to retain the mechanical strength of the corresponding mat, which was thus free-standing. Therefore, the electrodeposition method developed for the preparation of extended platinum surfaces presented in this part has been performed in a conventional three-electrode cell using the self-standing support to be coated as working electrode.

2. Copper underpotential deposition and Cu - Pt exchange by galvanic displacement

Underpotential deposition (UPD) is a method of deposition of metal adatoms at a potential less negative than their reversible Nernst potential for the reduction of the metal. This electrochemical method has already been used for the formation of different metal monolayers aiming at various surface architectures[33]. A wide range of UPD systems associating a metal substrate (such as Pt, Pd, Rh, Ir, Ru, Au, Ag) and an adsorbed metal (such as Cu, Ag, Cd, Hg, Pb, Sn ,Ge, Bi, As) have been studied[34]. In this context, Cu UPD[35–37] is a known technique to coat metal substrates including gold coated carbon electrodes[38] or nanoparticles[34] with a monolayer of copper which can be replaced by platinum. The exchange is performed by spontaneous galvanic displacement in a second step. This strategy was employed in the context of PEMFC electrodes development to take advantage of the

high specific activity associated with extended layers of platinum while improving the active surface area.

It has been shown in theoretical and experimental studies of Cu UPD on gold and platinum that the shift from the reversible Cu^{2+} reduction potential depends on the surface of the substrates (0.18 V on gold 0.44 V on Pt)[33]. Therefore the potential at which Cu UPD deposition can be performed on the NbC nanofibres had to be investigated. Cu UPD conditions (applied potential and duration) on NbC nanofibres were studied following a protocol developed for the deposition of Cu on a gold surface[36,37]. The used copper precursor was a $CuCl_2$ solution at acidic pH. The amount of copper deposited was calculated by integrating the Cu stripping peak (Figure 27). The experiment was repeated on the same support with a range of potentials and times.

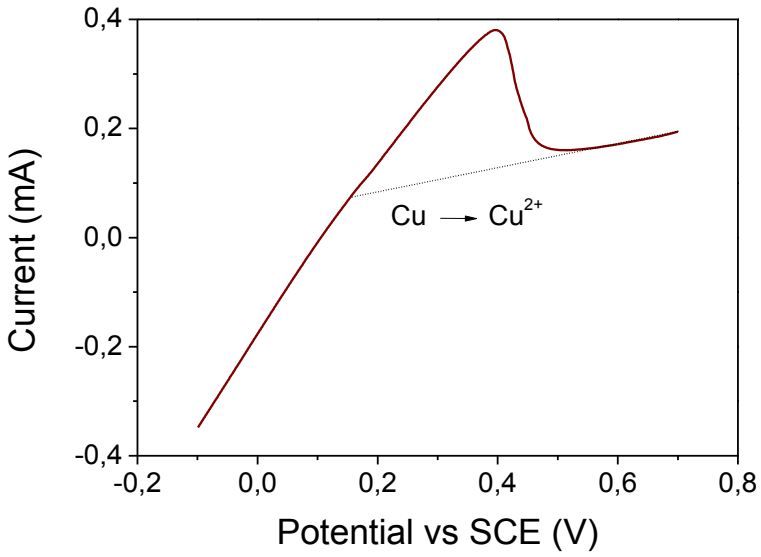

Figure 27. Currents obtained for the oxidation of the copper layer formed onto NbC at different potentials in a $CuCl_2$ solution (0.001 M) adjusted to pH 4 at 25 °C.

In Figure 28, the slope change suggests that the bulk deposition occurs at potential below -0.1 V vs SCE. This limit potential for the UPD deposition is lower than the Nernst potential (0.01 V vs SCE) due to the electronic configuration and crystalline structures of the substrate.

In our experiment, a progressive increase of the amount of deposited copper (Figure 29) was observed instead of a clear plateau in the UPD potential region. This progressive UPD behaviour could be explained by the presence of different types of sites active towards the Cu UPD on the surface of the NbC nanofibrous substrate (NbC, C, different crystal planes, different structural defects). Each of these would become active at a specific potential. In order to choose a suitable potential, the amount of deposited copper was monitored overtime at different fixed deposition

potentials. At - 0.1 V vs SCE, a saturation of charge and of Cu coverage has been reached confirming that the selected potential led to negligible bulk deposition behaviour. At this potential, the deposited amount of copper reached a plateau meaning that copper was selectively deposited onto the active sites and that the copper growth on copper was negligible (Figure 29). This plateau was no more visible for an electrodeposition at - 0.2 V vs SCE reinforcing the hypothesis of the bulk behaviour deposition at lower potentials. The deposition time was set to 250 seconds which is the time required for the saturation to be reached.

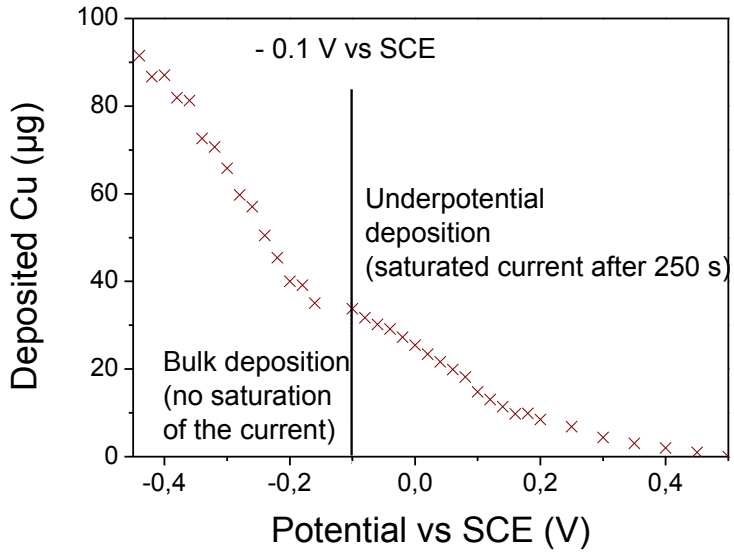

Figure 28. Amount of copper deposited as a function of the potential.

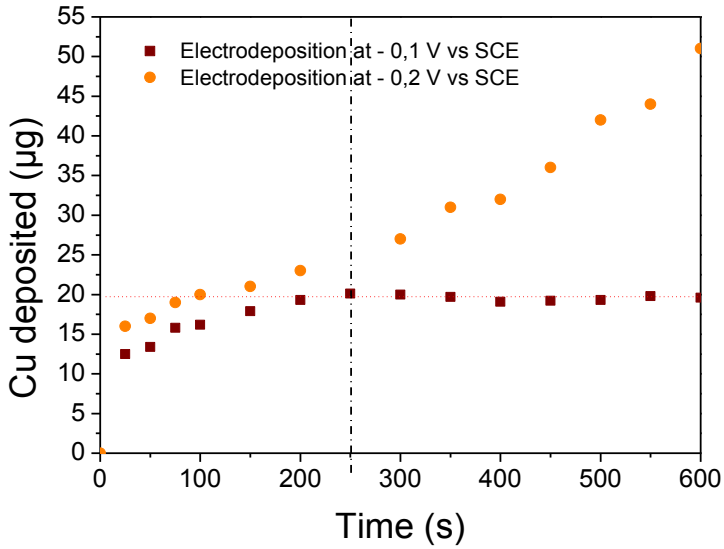

Figure 29. Amount of copper obtain with different underpotential deposition times.

The deposited copper film was used as a sacrificial layer to form a platinum film by galvanic displacement (1)[39]. To promote the exchange, the latter was performed in a chloroplatinic solution (H_2PtCl_6 0.002 M, HCl 0.05 M) at 80 °C for 1 hours.

$$2\ Cu + PtCl_6^{2-} \rightarrow 2\ Cu^{2+} + 6\ Cl^- + Pt \qquad \textbf{(1)}$$

Platinum was identified by cyclic voltammetry in N_2 saturated 0.1 M $HClO_4$ (Figure 30) and by SEM EDX while no trace of copper was present on the voltammogram proving that the exchange successfully occurred. The SEM observations disclosed that the mat was not covered by a continuous film but rather by discontinuous platinum submicron objects (Figure 31). A hypothesis would be that the electrodeposition conditions resulted in the growth of copper islands on the sites that are preferable for the UPD and a continuous film coverage could not be achieved. On the other hand, the galvanic displacement method demands that charge balance is maintained during the process, therefore there is a limit in the amount of material which is deposited.

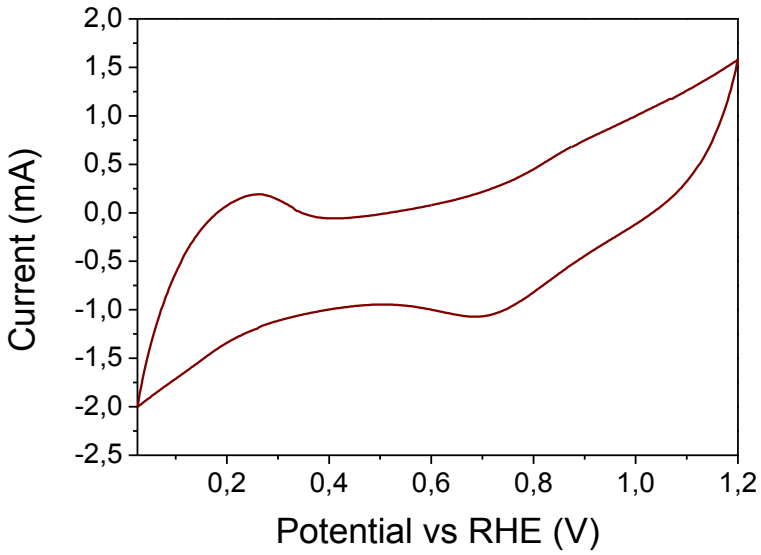

Figure 30. Cyclic voltammogram of NbC nanofibres covered by Pt submicron objects obtained after Cu deposition and platinum exchange by galvanic displacement.

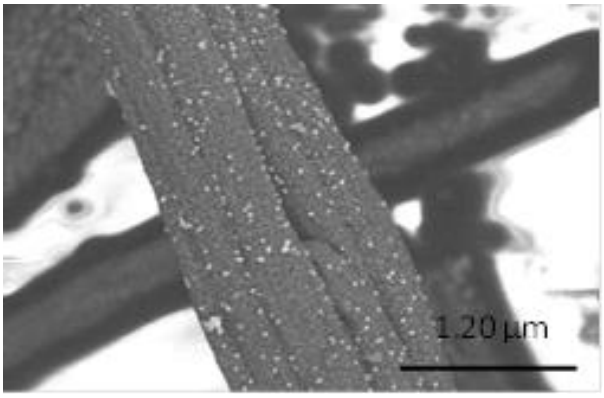

Figure 31. BE-SEM of NbC nanofibres, covered by Pt submicron objects obtained after Cu UPD deposition and platinum exchange by galvanic displacement.

A SEM micrograph of the NbC nanofibres after Cu UPD deposition and Pt galvanic displacement is shown in Figure 31. Pt submicron objects identified by EDX are homogeneously distributed on the substrate. The size distributions of these platinum objects are reported in Figure 32. The thickness of these objects has not been characterised.

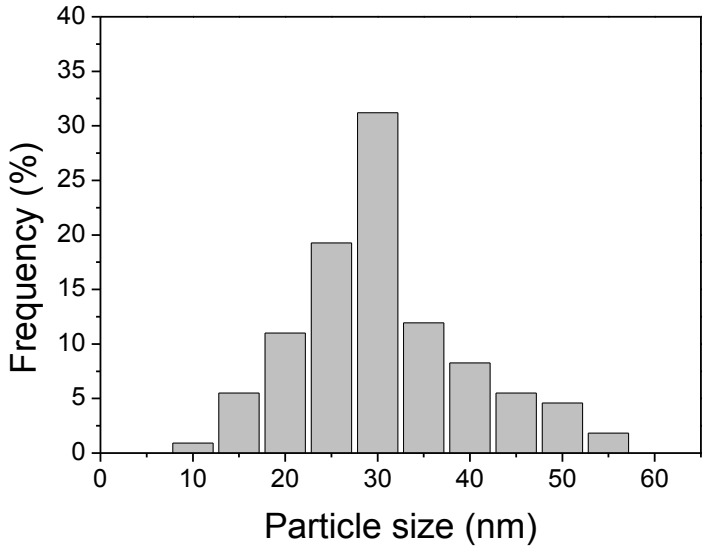

Figure 32. Size distribution of the Pt particles / islands obtained by potential under deposition and galvanic displacement.

A possible solution to improve the coverage would be repeating the Cu deposition and its displacement with Pt. However a supplementary UPD copper layer would preferably cover platinum instead of the bare support[40,41]. Repeating this 2-step process will consequently lead to a 3D growth of the platinum objects instead of the expected 2D growth resulting in a thin layer. For these reasons, it was decided to explore another electrodeposition method consisting on the direct electrodeposition of platinum on the NbC nanofibres.

3. Direct Pt electrodeposition

i. Synthesis

In 2012 a self-terminating electrodeposition process[42] has been proposed to control the growth of platinum. This process consists on the reduction of $PtCl_4^{2-}$ from the electrolyte precursor solution (K_2PtCl_4, 0.003 M). The specificity of this technique is to select a potential at which the platinum reduction is quenched by a saturated surface coverage of underpotential deposited hydrogen in order to achieve a Pt monolayer on the gold electrode. The surface can be reactivated by oxidizing the underpotential deposited hydrogen (H_{upd}). With these periodically pulsed potentials, it is possible to grow a Pt film layer by layer. The following part describes the results obtained by adapting the self-terminating electrodeposition process for the Pt catalysation of NbC nanofibrous self-standing mat. 20 cycles between -0.8 and 0.4 V vs SCE were carried out in a 3-electrode cell (Figure 33).

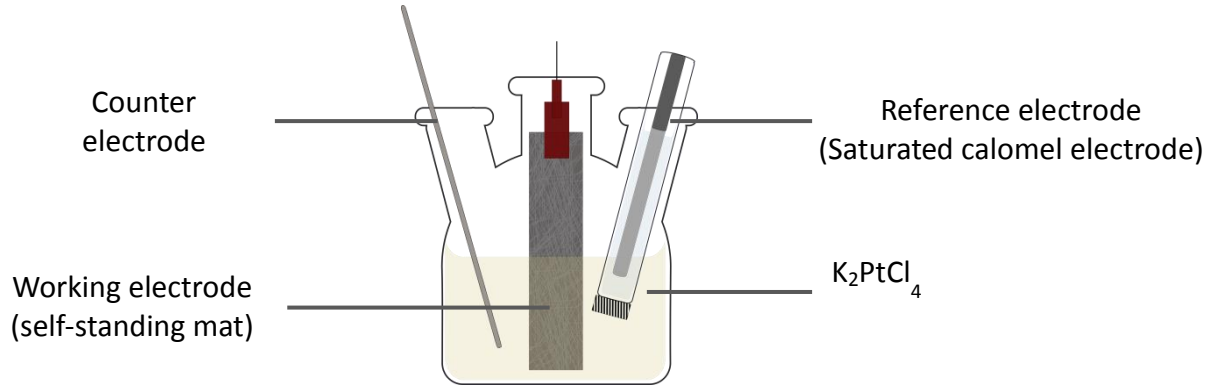

Figure 33. Pt Electrodeposition setup used for the Pt electrodeposition of the NbC nanofibres self-standing mat.

In order to improve the wettability of the hydrophobic NbC mat in the K_2PtCl_4 solution and to assist the penetration of the solution into the mat, it was dipped overnight in nitric acid solution before the electrodeposition.

ii. Morphological characterisation

Electron microscopies were performed to investigate the morphology of the electrodeposited platinum. SEM analysis of the NbC nanofibres surface has been performed before and after the catalysation (Figure 34). The smooth surface of nanofibres was covered by a rough layer of platinum. the reported layer by layer mechanism[42] that was achieved for the formation of an atomically smooth film could not be repeated on NbC nanofibres as shown in Figure 34.

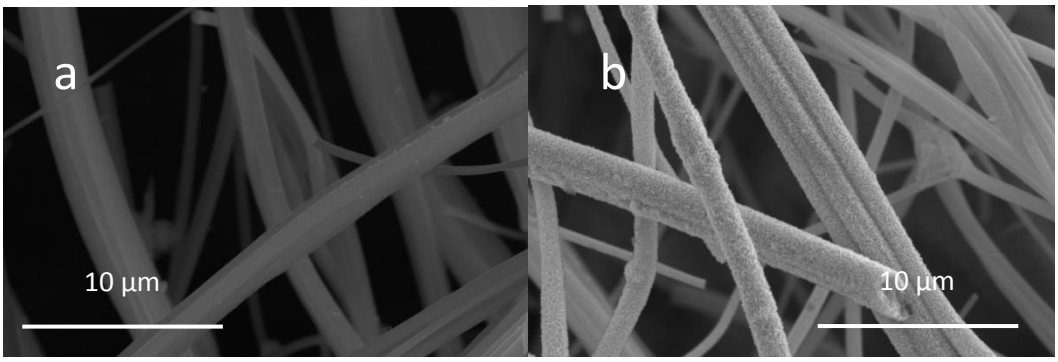

Figure 34. SEM micrographs of NbC nanofibres: naked (a) and catalysed by Pt electrodeposition (b)

It can be seen in Figure 34 that the deposition was not homogeneous through the mat thickness (Figure 36), resulting in an increasing gradient of thickness of the platinum layer from the core of the NbC nanofibres mat (region A) to the fibres on the surface of the mat (region B) (Figure 35).

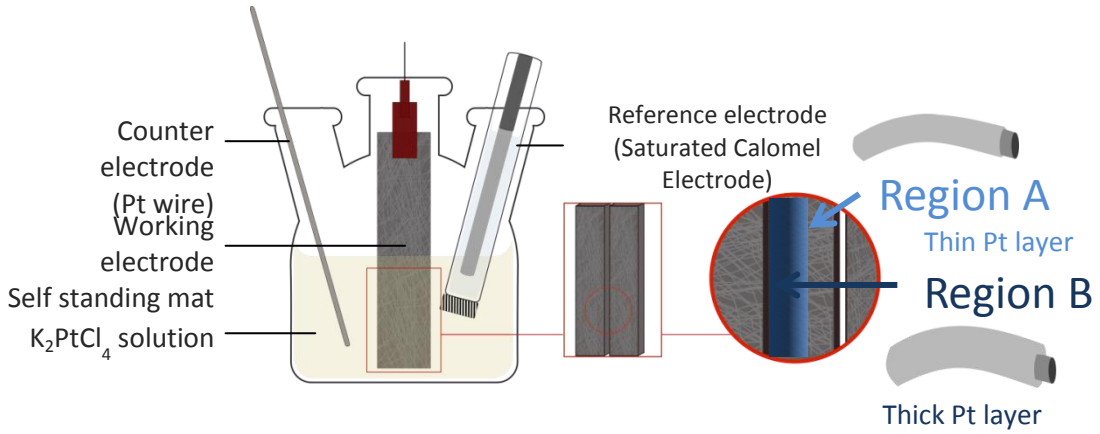

Figure 35. Setup for Pt electrodeposition on self-standing NbC nanofibres mat leading to different thickness of Pt.

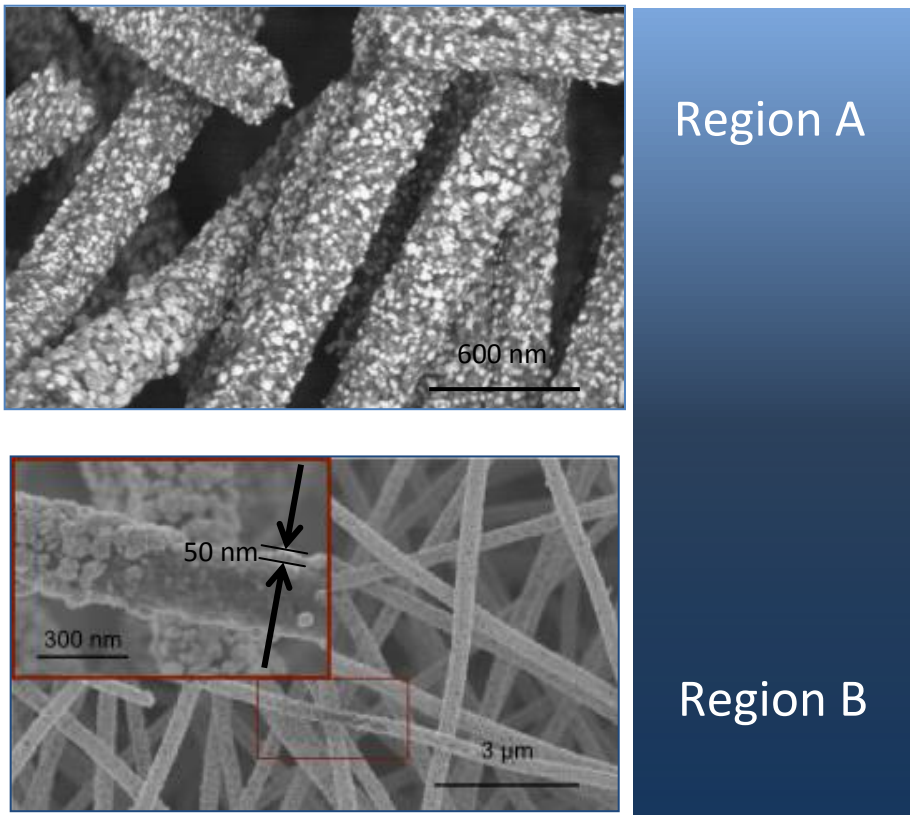

Figure 36. SEM micrograph of NbC nanofibres catalysed by electrodeposited from the core to the surface of the self-standing mat (zone A to B).

The nanofibres in the core of the mat (region A) were covered by Pt aggregates (Figure 36), with an average size of 35 nm (two dimensional). The size distribution is presented in Figure 38. Closer to the surface of the mat, a platinum network similar to a film was observed (area B) with an apparent thickness of 50 - 80 nm thickness.

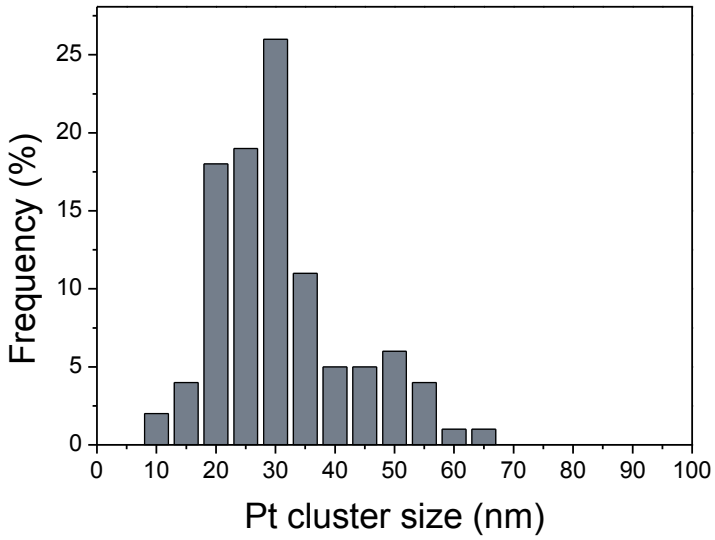

Figure 37. Size distribution of the Pt aggregates obtained by electrodeposition in region A.

In particular, a “flake” structure has grown on the nanofibres (Figure 38). This particular morphology could be attributed to the H_2 formed on platinum at low potential. These morphology heterogeneities can be explained by the diffusion of the precursor solution through the NbC nanofibres mat, leading to gradient of solution concentration.

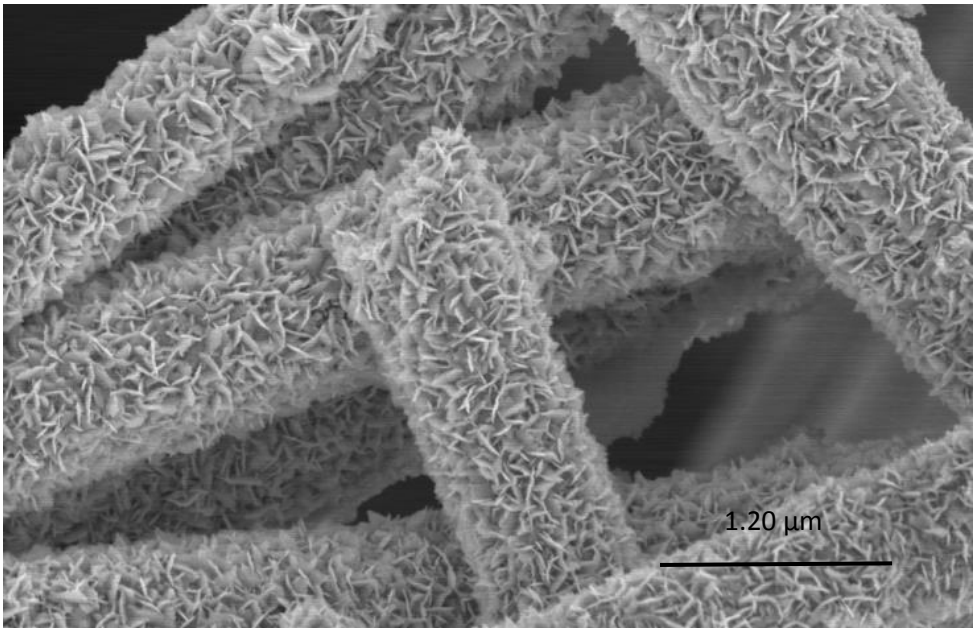

Figure 38. SEM micrograph of NbC nanofibres catalysed by electrodeposited in the outside of the self-standing mat (zone B).

Although the sample preparation by ultra-microtome partially detached and destroyed the Pt layer, the TEM observations of cross section suggest that these islands, conformal film or "flake morphology" are made of smaller Pt particles (Figure 39) with a large distribution (2 – 6 nm) (Figure 40).

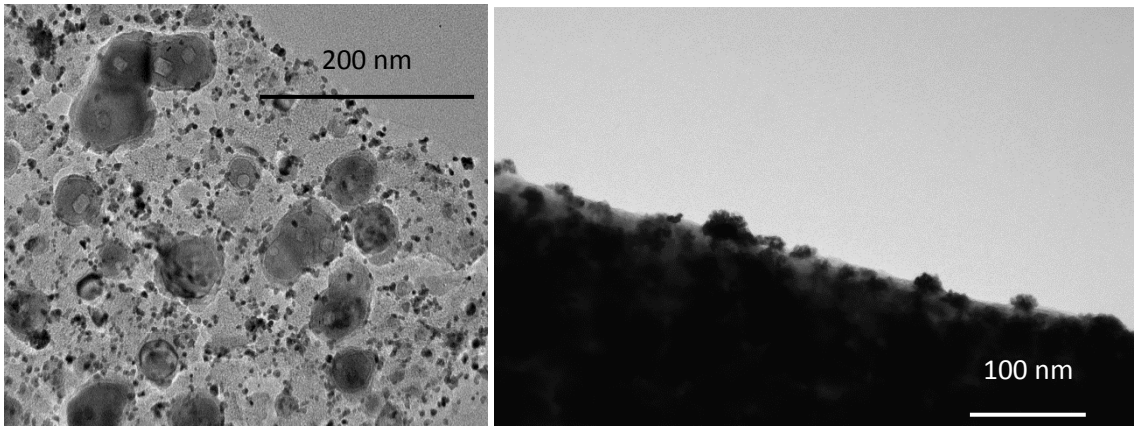

Figure 39. TEM micrograph of NbC nanofibres catalysed by electrodeposited on the self-standing NbC nanofibres mat.

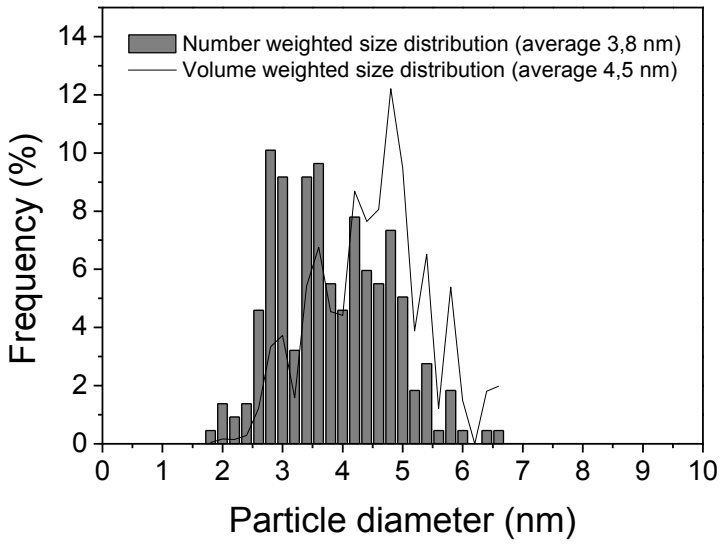

Figure 40. Size distribution of the Pt particles composing the Pt layer electrodeposited on NbC nanofibres mat.

TEM observation associated with an EDX elemental mapping confirmed the chemical composition of this shell and its conformal continuous morphology (Figure 41). It also discloses the presence of platinum in the NbC nanofibres core. The platinum particles filling the inner porosity of the nanofibres may not be accessible if the micropores are blocked by the further electrodeposited Pt. In

the electrochemical cell, the trapped platinum will be isolated from the electrolyte which could result in an ECSA and an ORR activity decrease.

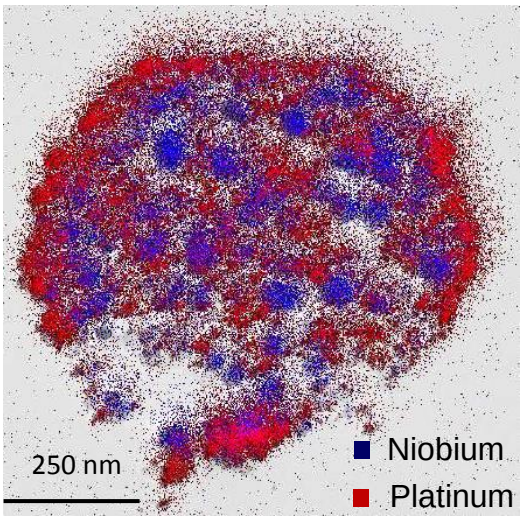

Figure 41. TEM observation of a transversal cross section with an EDX mapping of NbC nanofibres catalysed by Pt electrodeposition.

The platinum loading was investigated by X-ray fluorescence. The result, 20 $\%_{wt}$ Pt onto NbC fibres, was confirmed by SEM - EDX analysis and used for mass activity calculation.

iii. Electrochemical characterisation

The peaks characteristic of hydrogen adsorption and desorption typical of the noble metal are observed on the cyclic voltammogram at a low scan rate (2 $mV \cdot s^{-1}$) (Figure 42). The exact ECSA value could not been calculated from this CV because the immersed part of the mat could not be estimated accurately. Therefore the amount of platinum in contact with the solution could not be determined. Nevertheless the active platinum surface obtained by integrating the hydrogen adsorption peak was significant enough (corresponding to a platinum surface of the immersed part of 1115 cm^2) to be monitored during the accelerated stress test to 1.4 V vs RHE performed to investigate the electrochemical stability of the catalysed support.

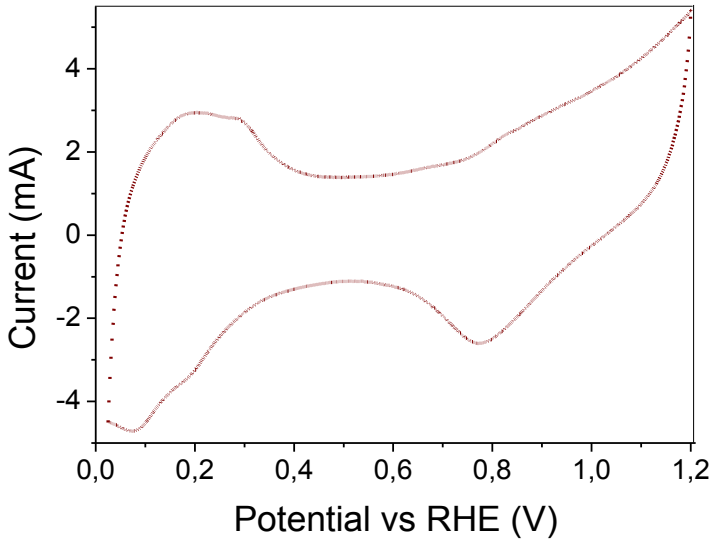

Figure 42. Cyclic voltammogram of the NbC nanofibres self-standing mat catalysed by electrodeposition in N_2 saturated $HClO_4$.

The stability of the catalysed nanofibres obtained after electrodeposition has been characterised with the accelerated stress test previously described (chapters II and III paragraph D.2). The ECSA decreases to 70 % of the initial value after 10,000 cycles between 0.6 and 1.4 V vs RHE. This is to be compared to the similar stability test performed on the nanoparticles of Pt supported on NbC nanofibres and the Pt/C reference (leading to respectively 20 % and 5 % of the initial ECSA values after the accelerated stress test)(Figure 43). The electrochemical stability enhancement achieved by modifying the electrocatalyst morphology seems to be conclusive.

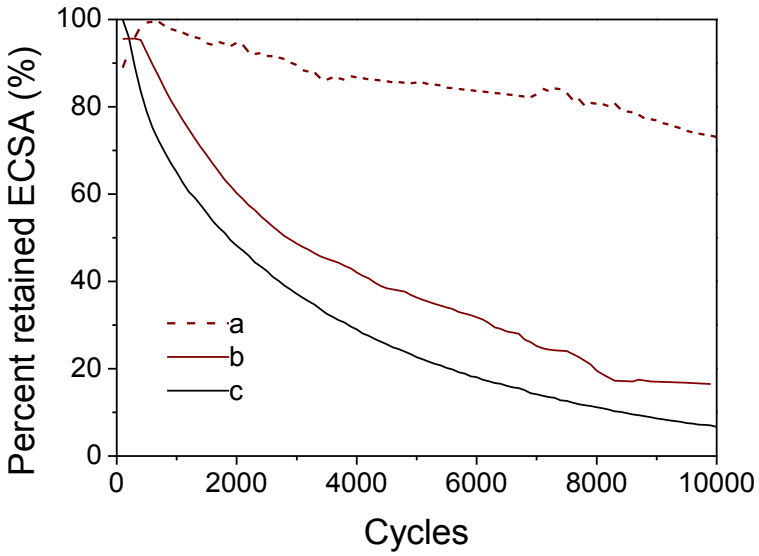

Figure 43. ECSA as a function of cycles for the NbC nanofibres self-standing mat catalysed by electrodeposition of Pt (a) compared to NbC nanofibres catalysed with Pt particles synthesised by polyol (b) and a reference Pt/C (c).

It has to be noticed that the AST was not performed on a thin disk electrode as it is usually carried out for other catalysed supports because the ink preparation requires vigorous sonication which could detach the Pt particles from the support. However, in order to measure the ECSA and to study the ORR electrocatalytic activity of the electrodeposited platinum the preparation of an ink and sonication was necessary. The ECSA 25 $m^2 \cdot g^{-1}_{Pt}$ measured for the electrodeposited Pt is similar to the 26 $m^2 \cdot g^{-1}_{Pt}$ calculated for the NbC nanofibres loaded with Pt nanoparticles and is lower than the 52 $m^2 \cdot g^{-1}_{Pt}$ obtained with the commercial reference 50 $\%_{wt}$ Pt/C (Figure 44).

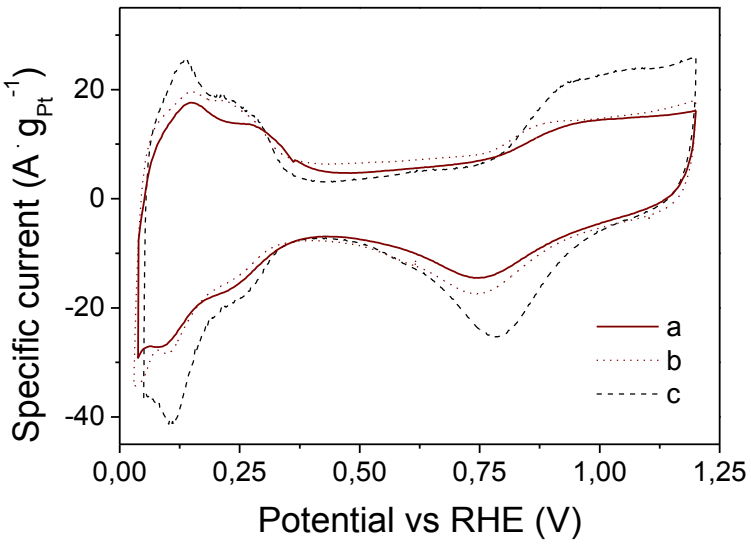

Figure 44. Cyclic voltammetry of the NbC nanofibres catalysed by electrodeposition of Pt (a) compared to NbC nanofibres catalysed by Pt particles (b) and a reference Pt/C (c).

As for catalysation with polyol nanoparticles, it can be assumed that the platinum electrodeposited on the inner porosity of the NbC nanofibres is not active because the pores are blocked by platinum particles on the surface of the nanofibres. This problem might be solved by further optimising the electrodeposition protocol in order to obtain thinner Pt layer that would retain the open porosity of the NbC nanofibres (Figure 45).

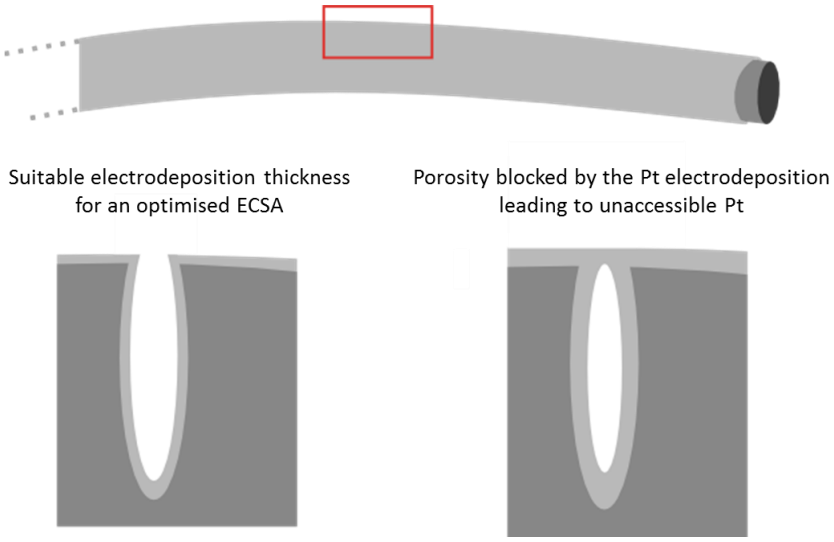

Figure 45. Influence of the Pt electrodeposited thickness on the accessible platinum amount.

The catalytic activity towards ORR was investigated by the linear sweep voltammetry in O_2 saturated in a 0.1 M $HClO_4$ solution as described in chapter II (paragraph D.3) and compared to the results obtained with NbC nanofibres loaded with Pt particles obtained by polyol and a reference Pt/C (Figure 46). The onset potentials of the ORR are 1.05 V vs RHE for the three catalysed supports. The NbC nanofibres catalysed by electrodeposited Pt present a lower limited diffusion current that can be explained by the difficulty to obtain a smooth and thin electrode with this material.

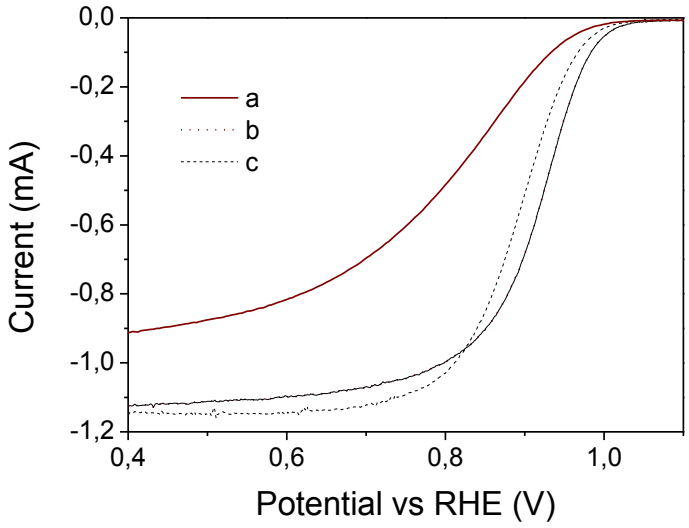

Figure 46. ORR Polarisation curves of the NbC nanofibres catalysed by electrodeposition of Pt (a) compared to NbC nanofibres catalysed by Pt particles (b) and a reference Pt/C (c).

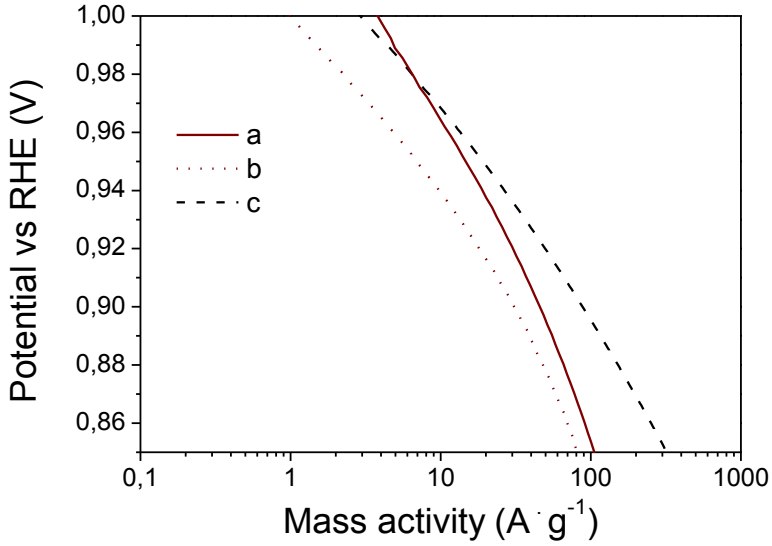

Figure 47. ORR Tafel plot for the NbC nanofibres self-standing mat catalysed by electrodeposition of Pt (a) compared to NbC nanofibres catalysed by Pt particles (b) and a reference Pt/C (c).

The ORR Tafel plots are shown for the NbC nanofibres are presented in Figure 47 , the mass activity of the 20 $\%_{wt}$ Pt/NbC nanofibres catalysed by electrodeposition is slightly higher than that of the same support loaded with Pt nanoparticles obtained by the chemical route. The ORR mass activities at 0.9 V were 45, 30 and 87 $A \cdot g^{-1}_{Pt}$ for the Pt/NbC catalysed by electrodeposition, for the NbC loaded with 20 $\%_{wt}$ Pt particles synthesised by polyol method and commercial reference 50 $\%_{wt}$ Pt/C, respectively.

G. Conclusion and perspectives

This chapter describes an electrospinning based synthesis route for the elaboration of NbC porous fibres with an average diameter of 400 nm with a unique structure consisting of NbC grains in a residual carbon matrix. This material possesses a high surface area of 80 $m^2 \cdot g^{-1}$ and mechanical properties leading to self-standing mats. In order to compare it with the other NbC materials prepared during this PhD work, the nanofibres were catalysed with identical Pt particles synthesised using the microwave assisted polyol method. The approach developed in the first chapter to characterise the NbC nanostructures was followed and further extended to the *in situ* characterisation in a single fuel cell unit. A power density of 465 $mW \cdot cm^2$ was reached at 1,200 $mA \cdot cm^{-2}$ by using an NbC fibrous cathode, further optimisation of the MEA preparation is required to reach the performance of Pt/C electrodes (960 $mW \cdot cm^2$ at 1,200 $mA \cdot cm^{-2}$)[21].

An exploratory work concerning platinum electrodeposition to catalyse this material was carried out aiming the formation of a thin conformal layer of Pt with high specific activity and improved stability. This method could benefit from the nanofibrous mat morphology and be directly applied to the self-standing NbC electrodes. A self-terminating electrodeposition process developed to control the growth of platinum films was optimised for the NbC mats leading to different Pt morphologies (flake-like structures, shells and islands). This deposition process resulted in a material with an outstanding stability assessed by an accelerated stress test to 1.4 V vs RHE. A possible explanation of this enhanced stability would be that the strong adhesion to the NbC grains of the support. TEM observations demonstrated that these electrodeposited Pt structures are made of platinum nanoparticles -with an average diameter of 4.6 nm. The mass activity of the electrodeposited Pt on NbC nanofibres is 45 $A \cdot g^{-1}_{Pt}$ which is slightly above the 30 $A \cdot g^{-1}_{Pt}$ obtained for the same NbC nanofibres loaded with pre-synthesised Pt particles for a similar ECSA (25 vs 26 $m^2 \cdot g^{-1}$), suggesting that the specific activity was improved. The optimisation of the self-terminating process is in progress in order to reduce and homogenise the thickness of the deposited platinum layer.

H. References

1 K. Lee, J. Zhang, H. Wang and D. P. Wilkinson, *J. Appl. Electrochem.*, 2006, **36**, 507–522.

2 X. S. Zhou, Y. J. Qiu, J. Yu, J. Yin and S. Gao, *Int. J. Hydrogen Energy*, 2011, **36**, 7398–7404.

3 H. S. Kim, G. Bugli and G. Djéga-Mariadassou, *J. Solid State Chem.*, 1999, **142**, 100–107.

4 K. Nakane, M. Morinaga and N. Ogata, *J. Mater. Sci.*, 2013, **48**, 7774–7779.

5 Y. Xia, P. Yang, Y. Sun, Y. Wu and B. Mayers, *Adv. Mater.*, 2003, **15**, 353–389.

6 S. K. Nataraj, K. S. Yang and T. M. Aminabhavi, *Prog. Polym. Sci.*, 2012, **37**, 487–513.

7 K. D. B. J. F. M. W. F. S. P.E. Sobol, *Handbook of X-ray Photoelectron Spectroscopy*, Perkin Elmer Corporation, 1992.

8 M. T. Marques, A. M. Ferraria, J. B. Correia, A. M. B. do Rego and R. Vilar, *Mater. Chem. Phys.*, 2008, **109**, 174–180.

9 C. Wagner, A. Naumkin and A. Kraut-Vass, in *NIST Standard Reference Database*, 2003, vol. 3.3.

10 G. McGuire, G. Schweitzer and T. Carlson, *Inorg. Chem.*, 1973, **12**, 2450–2453.

11 J. Rouquerol, F. Rouquerol, P. Llewellyn, G. Maurin and K. S. W. Sing, *Adsorption by Powders and Porous Solids: Principles, Methodology and Applications*, 2013.

12 B. Ding, H. Kim, C. Kim, M. Khil and S. Park, *Nanotechnology*, 2003, **14**, 532–537.

13 Y. Shao, J. Liu, Y. Wang and Y. H. Lin, *J. Mater. Chem.*, 2009, **19**, 46–59.

14 S. Cavaliere, S. Subianto, I. Savych, M. Tillard, D. J. Jones and J. Rozière, *J. Phys. Chem. C*, 2013, **117**, 18298–18307.

15 E. Antolini, *Appl. Catal. B Environ.*, 2009, **88**, 1–24.

16 J. Speder, A. Zana, I. Spanos, J. J. K. Kirkensgaard, K. Mortensen, M. Hanzlik and M. Arenz, *J. Power Sources*, 2014, **261**, 14–22.

17 M. Nesselberger, S. Ashton, J. C. Meier, I. Katsounaros, K. J. J. Mayrhofer and M. Arenz, *J. Am. Chem. Soc.*, 2011, **133**, 17428–33.

18 H. A. Gasteiger, S. S. Kocha, B. Sompalli and F. T. Wagner, *Appl. Catal. B Environ.*, 2005, **56**, 9–35.

19 Y. Wang, S. Q. Song, V. Maragou, P. K. Shen and P. Tsiakaras, *Appl. Catal. B-Environmental*, 2009, **89**, 223–228.

20 Y. Zhao, Y. Wang, X. Cheng, L. Dong, Y. Zhang and J. Zang, *Carbon N. Y.*, 2014, **67**, 409–416.

21 I. Savych, S. Subianto, Y. Nabil, S. Cavaliere, D. Jones and J. Rozière, *Phys. Chem. Chem. Phys.*, 2015, **17**, 16970 – 16976.

22 S. M. Alia, Y. S. Yan and B. S. Pivovar, *Catal. Sci. Technol.*, 2014, **4**, 3589–3600.

23 E. E. Parsonage and M. K. Debe US pat. 5,338,430 A, 1994.

24 N. Kristian and X. Wang, *Electrochem. commun.*, 2008, **10**, 12–15.

25 S. M. Alia, S. Pylypenko, K. C. Neyerlin, D. A. Cullen, S. S. Kocha and B. S. Pivovar, *ACS Catal.*, 2014, **4**, 2680–2686.

26 A. B. Papandrew, R. W. Atkinson, G. A. Goenaga, D. L. Wilson, S. S. Kocha, K. C. Neyerlin, J. W. Zack, B. S. Pivovar and T. A. Zawodzinski, *ECS Trans.*, 2013, **50**, 1397–1403.

27 S. S. Kocha, J. W. Zack, S. M. Alia, K. C. Neyerlin and B. S. Pivovar, *ECS Trans.*, 2013, **50**, 1475–1485.

28 R. M. Darling and J. P. Meyers, *J. Electrochem. Soc.*, 2003, **150**, A1523A1527.

29 R. Borup, J. Meyers, B. Pivovar, Y. S. Kim, R. Mukundan, N. Garland, D. Myers, M. Wilson, F. Garzon, D. Wood, P. Zelenay, K. More, K. Stroh, T. Zawodzinski, J. Boncella, J. E. McGrath, M. Inaba, K. Miyatake, M. Hori, K. Ota, Z. Ogumi, S. Miyata, A. Nishikata, Z. Siroma, Y. Uchimoto, K. Yasuda, K.-I. Kimijima and N. Iwashita, *Chem. Rev.*, 2007, **107**, 3904–51.

30 S. Chen, Z. Wei, X. Qi, L. Dong, Y.-G. Guo, L. Wan, Z. Shao and L. Li, *J. Am. Chem. Soc.*, 2012, **134**, 13252–5.

31 C. T. Campbell, *Surf. Sci. Rep.*, 1997, **27**, 1–111.

32 R. R. Adzic, J. Zhang, K. Sasaki, M. B. Vukmirovic, M. Shao, J. X. Wang, A. U. Nilekar, M. Mavrikakis, J. A. Valerio and F. Uribe, *Top. Catal.*, 2007, **46**, 249–262.

33 V. Sudha and M. Sangaranarayanan, *J. Phys. Chem. B*, 2002, **106**, 2699–2707.

34 H. Tang, J. H. Chen, M. Y. Wang, L. H. Nie, Y. F. Kuang and S. Z. Yao, *Appl. Catal. A Gen.*, 2004, **275**, 43–48.

35 D. Zhao and B.-Q. Xu, *Angew. Chemie*, 2006, **118**, 5077–5081.

36 Y. Yu, Y. Hu, X. Liu, W. Deng and X. Wang, *Electrochim. Acta*, 2009, **54**, 3092–3097.

37 M. H. Hölzle, U. Retter and D. M. Kolb, *J. Electroanal. Chem.*, 1994, **371**, 101–109.

38 M. Khosravi and M. K. Amini, *Int. J. Hydrogen Energy*, 2010, **35**, 10527–10538.

39 S. R. Brankovic, J. X. Wang and R. R. Adžić, *Surf. Sci.*, 2001, **474**, L173–L179.

40 I. Bakos, S. Szabó and T. Pajkossy, *J. Solid State Electrochem.*, 2011, **15**, 2453–2459.

41 E. Herrero, L. Buller and H. Abruna, *Chem. Rev.*, 2001, **101**, 1897 – 1930.

42 Y. Liu, D. Gokcen, U. Bertocci and T. P. Moffat, *Science*, 2012, **338**, 1327–30.

I. Table of Figures

Chapter IV: Niobium carbide nanotubes as electrocatalyst support

A. Introduction

The results described in chapter III on NbC nanofibres functionalisation show that 1 D nanostructured materials are valuable in terms of their specific surface area and adapted porosity. However residual amorphous carbon cloaks the niobium carbide grains in NbC nanofibres as in the NbC nanostructures (chapter II), and this residual carbon is oxidized under high voltage conditions, leading to degradation of the material. Further, the microporous character of this residual carbon might not provide the required accessibility of the gas to the catalyst. We are convinced that an NbC material with less residual carbon would lead to a more durable support.

This chapter presents the development of a 1 D nanostructured material with internal porosity that is expected to increase the electrocatalyst dispersion and improve gas accessibility to the platinum active sites. These features would be beneficial for the elaboration of efficient catalyst layers and allowing decrease of the platinum loading in an MEA without sacrificing cell performance[1].

Over the past 25 years, nanotubes have become something of a symbol in nanomaterials and nanotechnology research, with the advent in particular of carbon nanotubes in 1991 by Iijima[2] et al. and of inorganic (WS_2) nanotubes by Tenne[3]. This has led to intense experimental and theoretical research on hollow 1 D nanostructures[4]. In 2000 Mishra et al. indicated in their study of optical limiting behaviour of a carbon nanotube suspension that the high electrochemically accessible surface area of porous nanotube arrays, combined with their mechanical properties and high electronic conductivity, makes them attractive as electrodes for energy conversion devices[5].

B. Synthesis and characterisation

1. Synthesis of niobium carbide nanotubes

Ammonium niobate oxalate (ANO) $(NH_4)_3[NbO(C_2O_4)_3].2H_2O$ was chosen as niobium precursor because of its high solubility in water. Polyvinylpyrrolidone (PVP) was the carrier polymer used to adjust the viscosity of the solution. ANO/PVP composite fibres were prepared using an electrospinning setup (Figure 1). Further details are provided in the Experimental Annex (paragraph A.3).

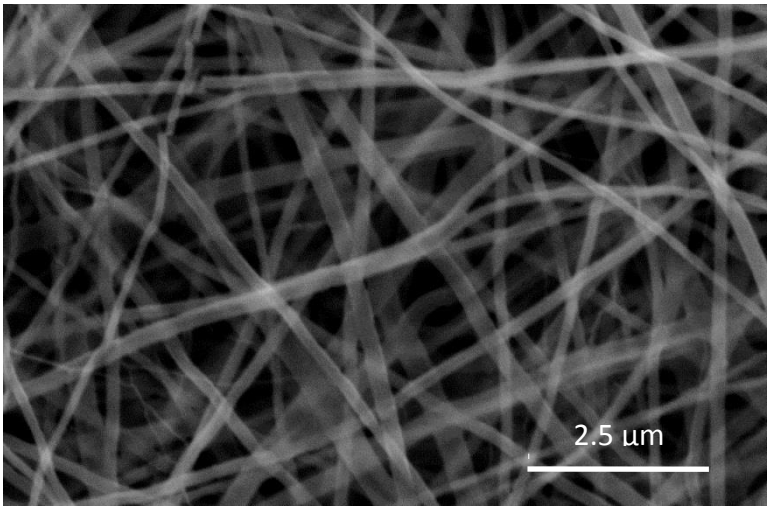

Figure 1. SEM micrograph of the ANO/PVP composite nanofibres.

Thermogravimetric analysis to 1000 °C in air (Figure 2) was performed to determine suitable temperature and time to remove the PVP carrier polymer. The weight loss between 25 and 150 °C was attributed to the solvent evaporation (water and ethanol). The main weight loss between 150 and 600 °C was assigned to PVP decomposition. No significant mass changes were observed at higher temperatures. Based on these observations, ANO/PVP composite fibres were thermally treated in air at 600 °C for 3 h to remove the carrier polymer and allow the transformation to Nb_2O_5.

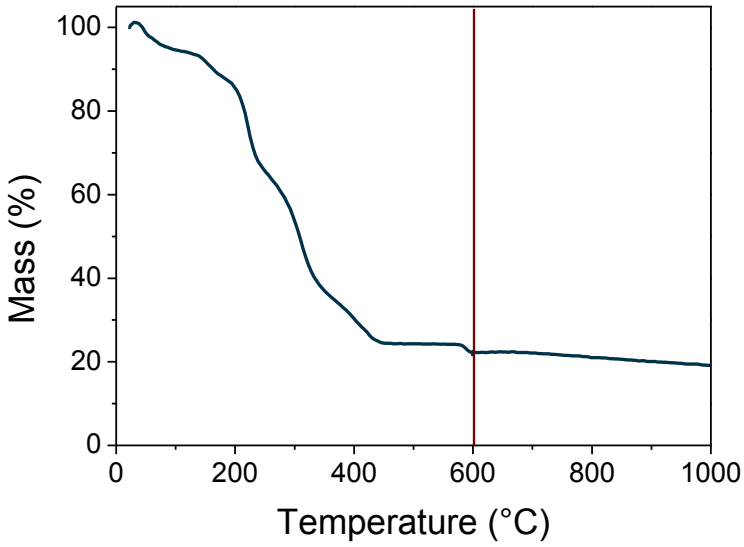

Figure 2. Thermogravimetric analysis of the fibres after the electrospinning step showing the end of the oxidation of PVP (red line).

The X-ray diffraction pattern of the material recovered after calcination at 600 °C is shown in Figure 3. Hexagonal niobium pentoxide[6] (ref 028-0317 hex PE) was identified as being the main crystalline phase present. The remaining lines were attributed to traces of monoclinic Nb_2O_5 (ref 037-1468 Mono P2). The diffraction lines are identified according to their Miller indices in Figure 3. No peak matching eventual residual carbon (25, 43 and 44 °2θ corresponding to [002], [100] and [101] Miller planes) derived from the carrier polymer was visible, nor any pronounced halo of X-ray scattering, that could have indicated the presence of amorphous carbon.

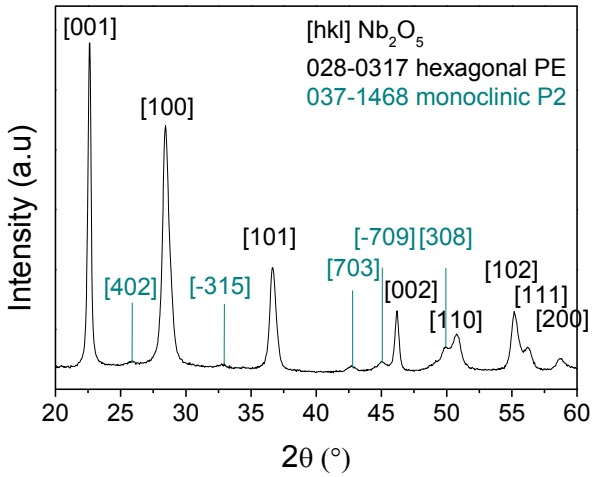

Figure 3. X-ray diffractogramm of the Nb_2O_5 material obtained after the calcination at 600 °C with Miller indices.

The Nb_2O_5 fibres recovered from the previous calcination step were then carburated by heating to 1100 °C at 4 °C·min^{-1} in 10 % CH_4/H_2 mixture gas at a total flow rate of 100 mL·min^{-1}. This reaction was carried out in a Temperature Programmed Reduction (TPR) furnace so as to use the Thermal Conductivity Detector (TCD) in order to stop the experiment after the total conversion of Nb_2O_5 to NbC. The successive reactions were monitored by following the thermal conductivity of the gas furnace (Figure 4).

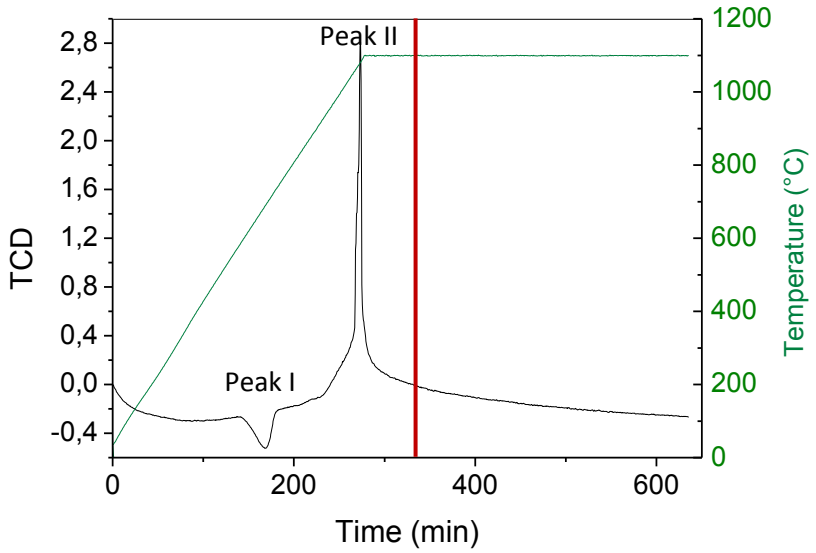

Figure 4. Carburation of Nb_2O_5 nanofibres at 1100 °C in 10 % CH_4/H_2 showing the evolution of the thermal conductivity. (The red bar indicates the time the reaction was stopped).

A study of the kinetics of the reaction of the conversion of niobium oxide into its carbides[7] describes that Nb_2O_5 is reduced in methane/hydrogen through the two following consecutive reactions:

$$\mathbf{Nb_2O_{5\,(s)} + H_{2\,(g)} \rightarrow 2NbO_{2\,(s)} + H_2O_{\,(g)}} \quad (1)$$

$$\mathbf{NbO_{2\,(s)} + 3CH_{4\,(g)} \rightarrow NbC_{\,(s)} + 2CO_{\,(g)} + 6H_{2\,(g)}} \quad (2)$$

The peaks visible on TCD can be clearly correlated with the above reactions (1) & (2) by using the thermal conductivities of the corresponding gas (Table 1).

Table 1 Thermal conductivity of gases involved in Nb_2O_5 reduction (these values increase with temperature).

Gas	H_2	CH_4	CO	H_2O
Thermal conductivity W/(m·K) values at 25 °C	0.168	0.030	0.0232	0.016

H_2 thermal conductivity is one order of magnitude higher than that of the other gases involved in the carburation of niobium oxide (CH_4, CO, H_2O) and is mainly responsible for the variation of the signal. Two different events occurred at 600 and 1100 °C during the carburation. The weaker one corresponds to a decrease in thermal conductivity (peak I). The significantly more intense signal corresponds to an increase in thermal conductivity (peak II). Peak (I) matches the consumption of H_2 during the reaction (1), while peak (II) is attributed to the reaction (2). The increase of thermal conductivity corresponds thus to the hydrogen release that occurs during the NbC formation reaction from NbO_2. Based on these observations, it was decided to stop the reaction after the occurrence of peak (II), i.e. after a 180 minutes dwell at 1100 °C (Figure 4).

The conversion of Nb_2O_5 into NbC can also be achieved at lower temperature by increasing the time of the dwell, for instance at 900 °C for 17 hours [8,9]. Investigations were made to determine the effect of the dwell duration at 1100 °C. For instance, by increasing the duration of this step to 6 hours, NbC hollow fibres were obtained with larger grain sizes, leading to nanotubes “with porous walls” or “pea-pod like” nanotubes (Figure 5).

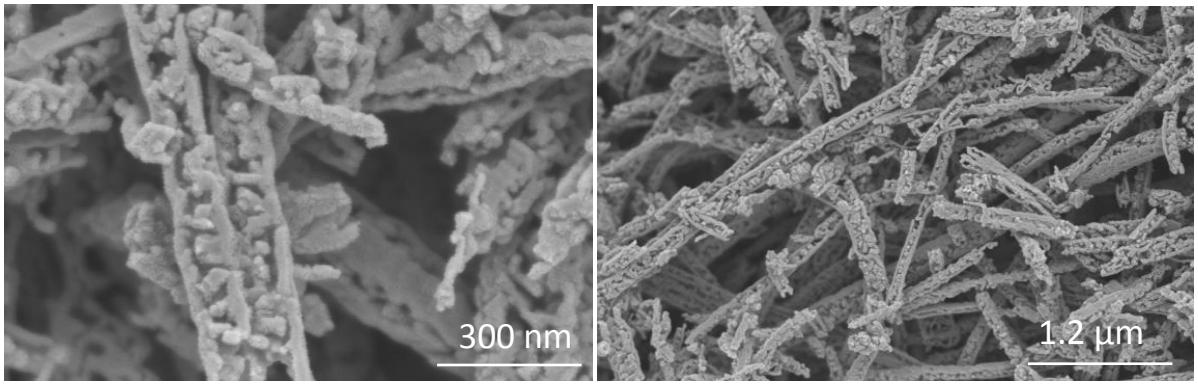

Figure 5. SEM micrographs of “pea-pod like” nanotubes obtained after 6 h heat treatment at 1100 °C.

The duration of the dwell at 1100 °C was finally fixed to 3 hours to obtain the targeted hollow fibrous morphology. With these optimised carburation conditions, the grain size growth does not cause a discontinuity in the morphology of the materials. The chosen process conditions are summarised in Table 1.

Table 1. NbC nanotubes synthesis route details.

Step	Conditions
Electrospinning	PVP (13 %)/ANO (19.5 %) Solvent: H_2O/EtOH (50/50 volume) Voltage 15 kV; flow rate 0.2 mL · h^{-1}; drum rotation 300 rpm
Calcination	1h 150 °C → 1h 250 °C→ 3 h 600 °C in air (ramp up 0.5 °C min^{-1} / 0.5 °C min^{-1} / 5 °C min^{-1})
Carburation	180 min at 1100 °C in CH_4/H_2 (ramp up 4 °C min^{-1})

2. Characterisation of the chemical and structural composition of niobium carbide 1D nanostructured material

The structure of the material recovered after carburation was characterised by powder X-ray diffraction, Figure 6. Niobium carbide NbC (ref 038 – 1364 cubic Fm – 3m) was identified as the only crystalline phase, with no other non-assigned diffraction lines that could have corresponded to unreacted Nb_2O_5, other niobium carbide compositions (Nb_2C) or niobium metal.

The crystallite sizes were calculated with the Scherrer formula with the [111], [200] and [220] Miller plans leading to respectively 12 nm, 12 nm and 13 nm. Considering that a grain composing the wall can contain several crystallites, this calculation is consistent with the TEM observations of 19 nm average sized grains (paragraph B.3).

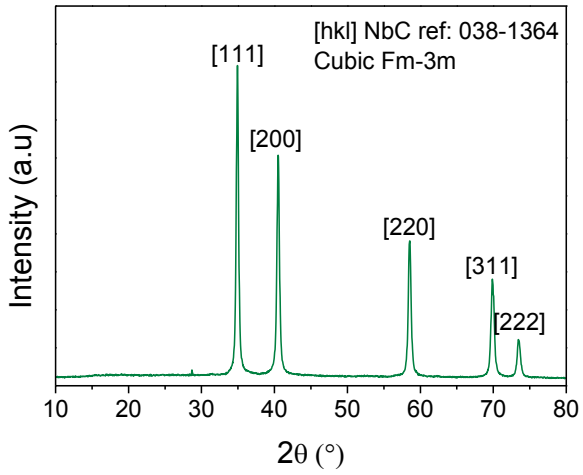

Figure 6. X-ray diffractogramm of the NbC material obtained after the carburation step.

Although the carbon of the carrier polymer is completely removed by calcination in step 2, carbon could also be formed during the carburation step by decomposition of CH_4 at high temperature as previously described by Teixeira da Silva et al. in their study of the conversion of niobium oxide to niobium carbide in methane[9].

The quantification of any residual carbon was investigated by thermogravimetric analysis (Figure 7). The same calibration relation was used as previously for the characterisation of NbC nanostructures and NbC nanofibres that correlates the mass variation with the NbC/C ratio. The TGA of electrospun NbC materials displays an overall mass gain that corresponds to NbC/C = 96/4 (Figure 7 and Figure 8).

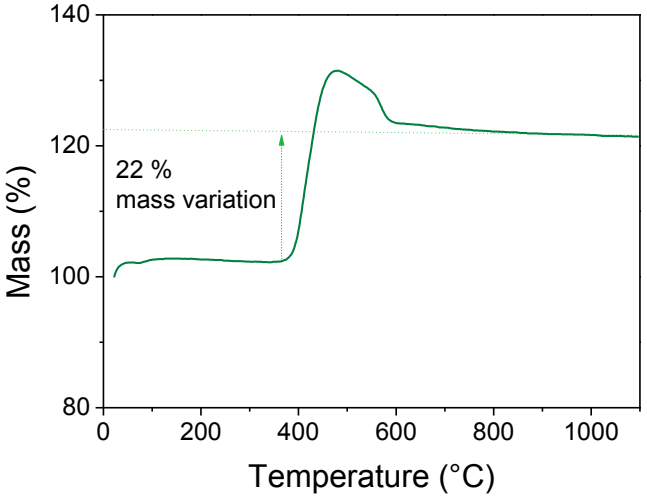

Figure 7. Thermogravimetric analysis of synthesised NbC/C 1D nanostructured material after carburation (step 3).

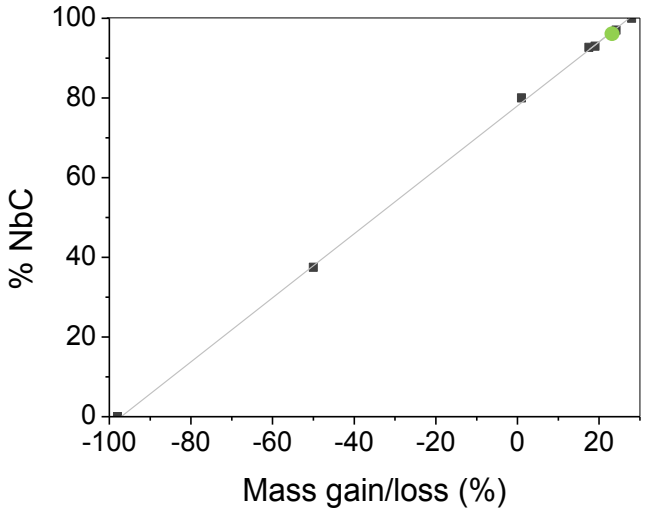

Figure 8. Calibration curve for the determination of residual carbon content in NbC samples by TGA.

The total carbon content was also determined by CHNS elemental analysis. This method provided a value of 16 $\%_{wt}$ of carbon in the material, corresponding to 5 $\%_{wt}$ of non-carbide carbon. This result is very similar to that obtained with the TGA calibration.

As for the previously synthesised NbC/C nanostructures and nanofibres (chapters II and III), the NbC NbC/C 1D nanostructured material were characterised by XPS spectroscopy. Figure 9 shows the XPS spectrum in the Nb 3d region. Given the theoretical values of the 3d Nb_{NbC} (Nb $3d_{5/2}$= 203.7 eV for NbC[10] and Nb $3d_{5/2}$= 207.2 eV for Nb_2O_5[11]), the peaks were fitted by two doublets (Nb $3d_{5/2}$= 204.52 and Nb $3d_{3/2}$ 207.24 eV) and Nb_2O_5 (Nb $3d_{5/2}$= 208.06 and Nb $3d_{3/2}$ 210.78). The integration of these peaks suggests that 60 % of surface niobium is present as niobium oxide. However, since no diffraction lines characteristic of niobium oxide are visible in the X-ray diffractogram of the carburated sample, it is assumed that niobium oxide is only present at surface and not in the bulk, as it was the case for the NbC nanostructures and nanofibres (chapters II and III). No traces of metallic niobium or diniobium carbide Nb_2C could be observed in the XPS spectrum.

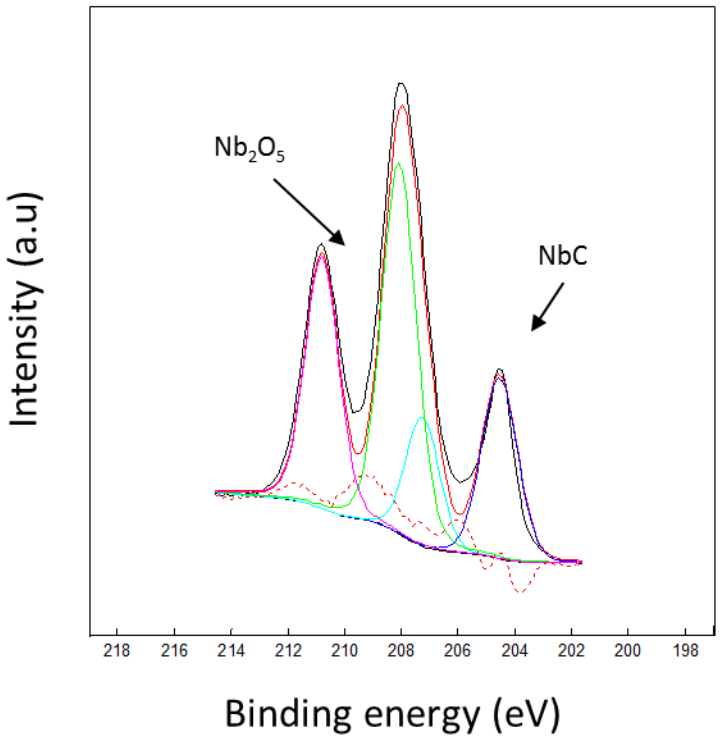

Figure 9. Nb 3d region of the XPS spectrum of NbC/C 1D nanostructured material.

The XPS signals of residual carbon, 1s C_{carbon} = 284.91 eV, and carbon as carbide (1s $C_{carbide}$ =283.25 eV) also identified in the XPS spectra are in good agreement with reported ranges of values: 284 – 285 eV for free carbon, and 281 – 283 eV for carbide carbon[12]. Other signals from carbon in other environments (carbonate, alcohols) were also observed: 1s $C_{carbonates}$ = 290.21 eV and 1s $C_{alcohol}$ = 286.8 eV, in agreement with literature values of 289 – 291 eV and 286 – 287 eV, respectively.

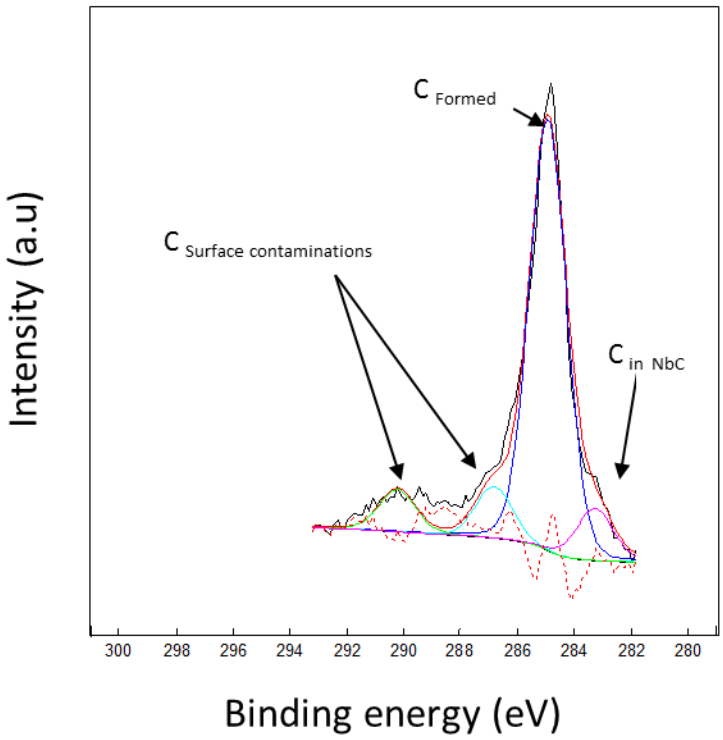

Figure 10. C 1s region of the XPS spectrum of of NbC/C 1D nanostructured material obtained after carburation.

The C 1s peaks of residual carbon and NbC carbon were integrated, however the result suggests that 86 % of the total amount of carbon is residual carbon. The XRD diffractogram displays evidence neither for an amorphous carbon component nor the carbon pattern (25, 43 and 44 °2θ matching the [002], [100] and [101] Miller planes). Furthermore, the literature highlights the difficulty of quantification of carbon by XPS, and certainly this value seems overestimated. Further investigation of the surface of this material by high resolution TEM was carried out, Figure 11. This micrograph shows the presence of graphene layers encapsulating some of the grains comprising the NbC support, which provides an explanation for the high amount of carbon on the NbC surface detected by XPS. This observation was coupled with X-ray emission detection and the presence of carbon and niobium was confirmed. Graphene has been investigated as a support for Pt and accelerated ageing tests have been performed[13]. The stability through accelerated stress test reported in this study (resulting in an ECSA decrease after 10,000 voltage cycling up to 1.4 V vs RHE that was significantly reduced compared to that of a Pt/C reference (69 % vs 95 % decrease) suggested that the presence of graphene layers will not compromise the stability of NbC/C 1D nanostructured material (paragraph D.2). Furthermore, given the low total amount of carbon in the material it can be concluded that its core is free of residual carbon.

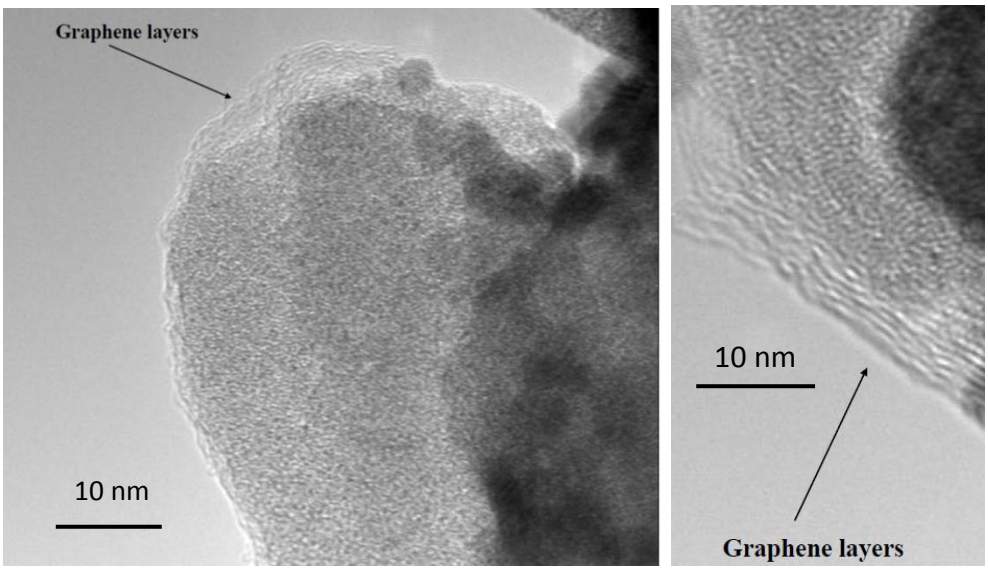

Figure 11. High resolution TEM micrographs of NbC/C 1D nanostructured material.

To conclude, the XPS analysis has identified the presence of Nb_2O_5, and also shown the existence of residual carbon at the surface of the characterised support. These results are consistent with the compositional analysis by TGA, elemental analysis and XRF. The surface carbon was identified by high resolution TEM as being in the form of graphene layers. One way to reduce the amount of excess carbon formed during NbC preparation may be to carry out the synthesis with lower concentrations of methane. In this case it should be considered that longer reaction times or higher temperatures might be required and that lower values of surface area might result. Finally, no XPS signals were observed for Nb_2C or metallic niobium, in agreement with the results from XRD.

3. Morphological characterisation of niobium carbide nanotubes

The morphology of the electrospun carburated materials was characterised by scanning electron microscopy. A 1D nanomaterials with hollow cores and porous walls is shown in Figure 12.

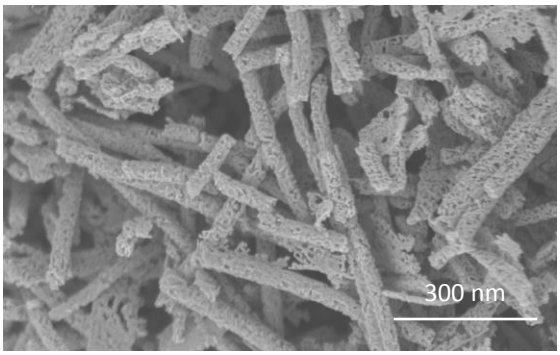

Figure 12. SEM micrograph of the carburated Nb_2O_5 displaying hollow cores.

The tubular morphology was confirmed by cross-sectional TEM observation (Figure 13) showing a hollow core. Furthermore, the walls of the hollow fibres appear themselves to be porous.

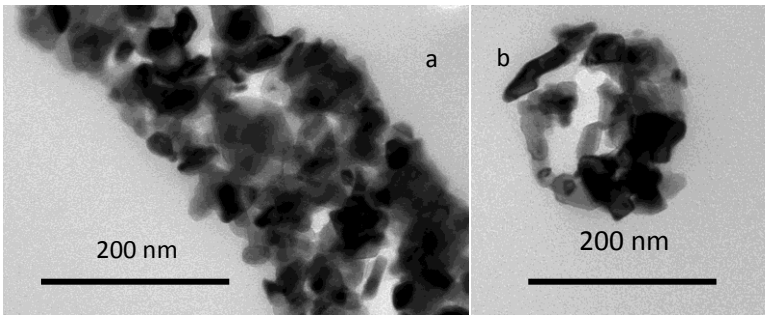

Figure 13. TEM micrograph of a microtomed section of the NbC nanotubes: transversal (a) and longitudinal (b) observations.

An average external diameter of 160 nm for the NbC nanotubes was measured from several SEM micrographs (Experimental Annex paragraph C.1.i). This value and the size distributions are close to that of the Nb_2O_5 nanofibres obtained after calcination, and of ANO/PVP composite nanofibres obtained directly after electrospinning (Figure 16a, 16b and 16c).

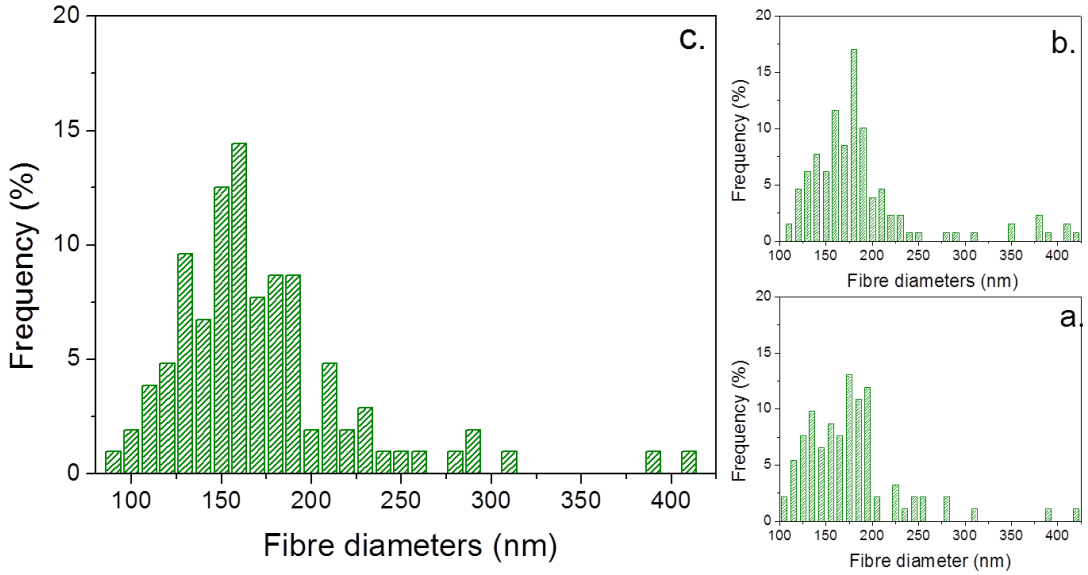

Figure 14. Diameter distribution of as-prepared ANO/PVP composite nanofibres (a), calcined nanofibres (b) and carburated nanotubes (c).

These nanotubes are composed of edgy grains with a size distribution in the range of 5 - 30 nm (Figure 14).

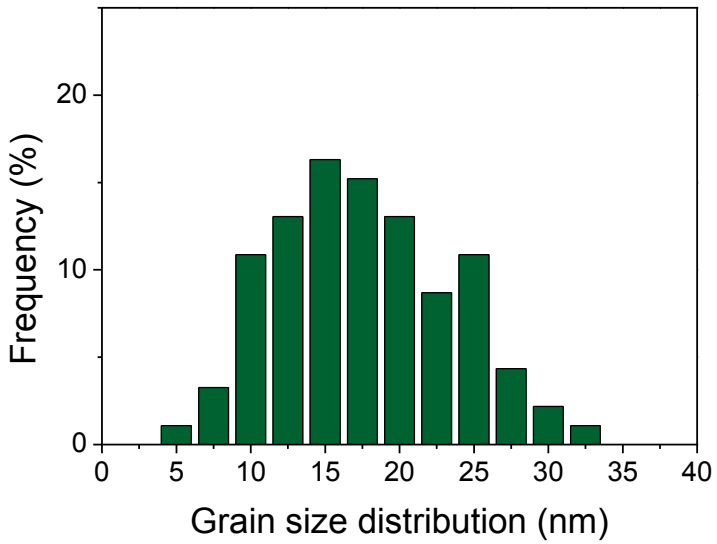

Figure 15. Size distribution of the grain composing the nanotubes obtained by TEM observations.

It is interesting to notice that the materials before carburation were a mixture of Nb_2O_5 solid fibres and ribbons (Figure 9). The latter, of width greater than 400 nm (reported in the diameter distribution Figure 16a, 16b and 16c), could be the result of a merging of nanofibres or of a collapse of some nanofibres during the electrospinning due to fast solvent evaporation from the precursor solution at the surface of liquid jet. A similar effect was reported for tailored ribbon-like SnO_2 prepared by Huang et al.[14]. These authors suggested that this type of morphology has a higher tolerance to bending than usual cylindrical nanofibres which contributes to a better flexibility that could allow easier handling of a self-standing mat. However, nanofibres of cylindrical shape allow more inter-fibre macroporosity which is a requirement for gas diffusion and water transport through the catalyst layer. The observed mixture of ribbons and fibres obtained after calcination could be beneficial in this respect by providing a compromise between enhanced mechanical strength (ribbons) and suitable macroporosity (fibres). No flat or dense 1D nanostructures were observed as final morphology of the NbC nanotubes.

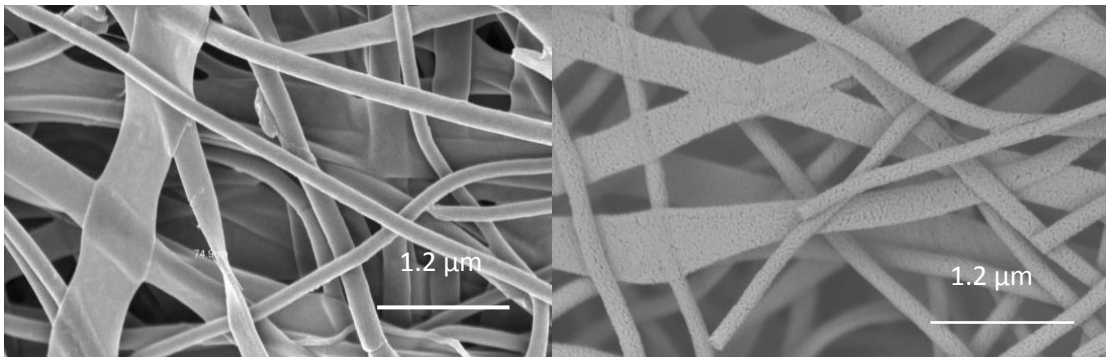

Figure 16. SEM micrograph of Nb_2O_5 nanofibres and ribbons.

The fibre diameter distribution profiles of the materials obtained after electrospinning, calcination and carburation are shown in Figure 16 are similar. The few flat ribbons present after calcination led, like the nanofibres, to nanotubes morphologies albeit with a larger external diameter. Despite the previously described grain size evolution, no significant increase in the external diameter of the nanotubes was observed.

The surface area and porosity characteristics were investigated by N_2 adsorption/desorption. The corresponding isotherm (Figure 17a) displays hysteresis of type H3 generally associated with slit shaped pores that match the edged particles that form the nanotubes[15,16]. The obtained BET specific surface area of 28 $m^2 \cdot g^{-1}$ is lower than that of the other niobium carbide based materials described in this thesis (chapters II and III). Although the NbC nanostructures and the NbC nanotubes have a similarly low carbon contents (respectively 3 $\%_{wt}$ and 4 $\%_{wt}$), these two support materials present significantly different surface areas. This difference could be due to the presence of carbon as

graphen layer in the case of the NbC nanotubes. However, the high developed intra-tubes and inter-tubes porosity may be more suitable. On the isotherms in the low relative pressure region, the nitrogen quantity adsorbed is lower than for the NbC nanofibres (chapter III paragraph B.2) suggesting a smaller microporous volume (pores diameter smaller than 2 nm) for the NbC nanotubes than for the NbC nanofibres. Furthermore, the hysteresis of type H3 is typical for the intergranular porosity, also visible on the TEM micrographs, and resulting in mesoporosity and macroporosity that are required for the electrocatalyst particles deposition. A distribution of the pore size was calculated by Barett-Joyner-Halenda (BJH) analysis using the desorption branch of the isotherm (Figure 17b).

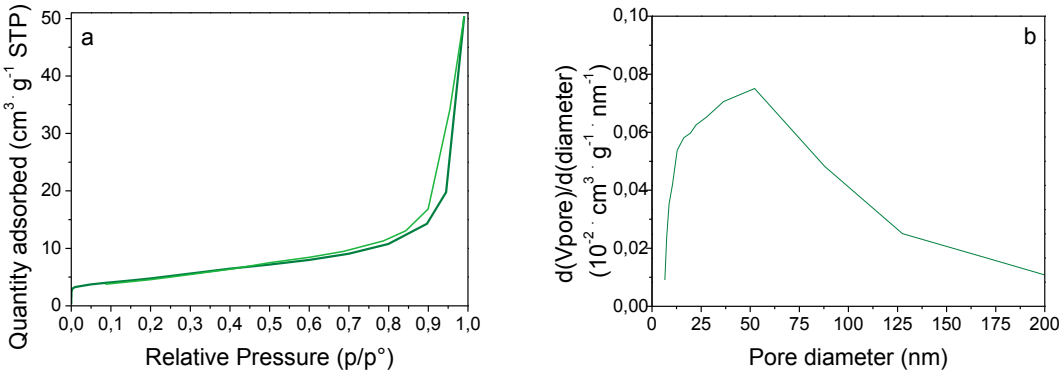

Figure 17a. N_2 adsorption / desorption isotherm obtained for NbC nanotubes.
b. Pore size distribution obtained by BJH analysis assuming cylindrical pores for the NbC nanotubes.

The calculated surface area is in the same range as that of carbon nanofibres prepared by electrospinning with various heat treatments reported by Liu et al. in their review (20 $m^2 \cdot g^{-1}$ for carbonisation at 1500 °C)[17] or Savych et al. (36 $m^2 \cdot g^{-1}$ for a 1100 °C carbonisation)[18].

C. Preparation and characterisation of Pt supported on NbC nanotubes

1. Synthesis of Pt supported NbC nanotubes

The microwave assisted polyol method developed to prepare Pt nanoparticles to load NbC nanostructures and nanofibres was used for the NbC nanotubes. The targeted Pt loading was 35 $\%_{wt}$. Further details are provided in chapter II (paragraph C.1) and in the Experimental Annex (paragraph D.1.).

2. Physico-chemical characterisation of Pt supported NbC nanotubes

SEM and TEM were used to observe the supported nanoparticles, and the micrographs are reproduced in Figures 18 and 19, and Figure 20 respectively. It may be seen that the Pt particles are homogeneously dispersed on the surface of the NbC nanotubular supports. Their average diameter of 3.1 nm is confirmed (see distribution in chapter II paragraph C.2).

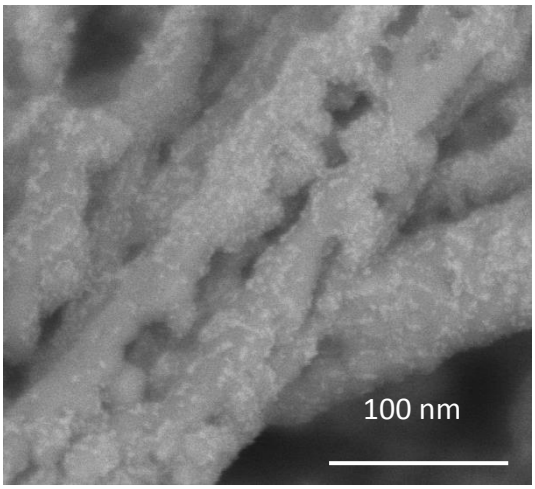

Figure 18. SEM (BSE mode) micrograph of NbC nanotubes catalysed with Pt nanoparticles.

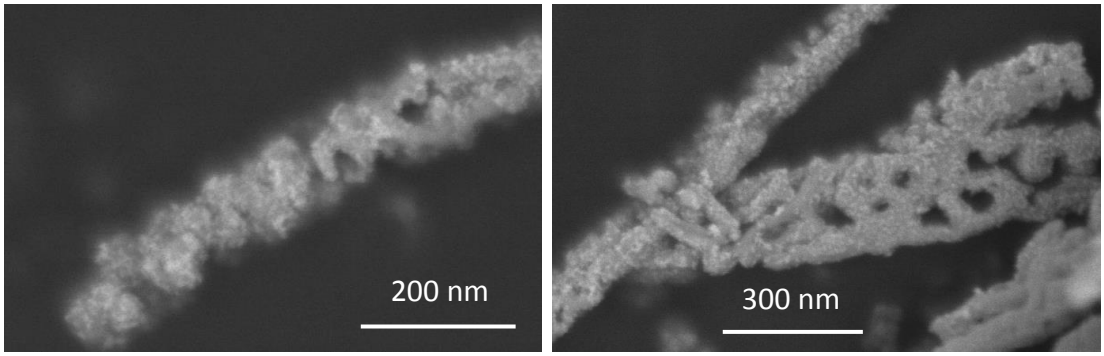

Figure 19. SEM (BSE mode) micrographs of the NbC nanotubes catalysed with Pt nanoparticles.

Platinum and niobium carbide were discriminated one from the other by using SEM in the back scattered electron (BSE) mode (Figure 18), which shows a good distribution of the platinum nanoparticles (brighter due to their higher electron density compared to the support) onto the internal and external surface of the NbC nanotubes. This observation is confirmed by the TEM micrographs (Figure 20), showing the complete and homogeneous coverage of the tubes by the nanocatalysts.

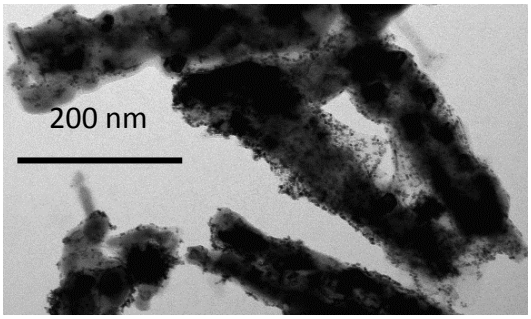

Figure 20. TEM micrograph of 30 $\%_{wt}$ Pt/NbC nanotubes catalysed with Pt nanoparticles.

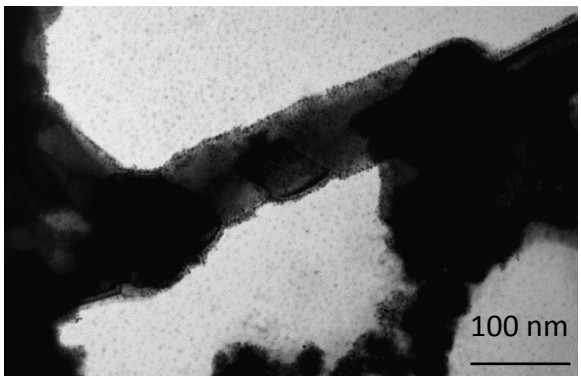

Figure 21. TEM micrographs of 50 $\%_{wt}$ Pt/NbC nanotubes nanoparticles.

Pt loading on NbC nanotubes has been evaluated by X-ray fluorescence (XRF) by using a calibration with standards prepared from commercial platinum black and niobium carbide previously described (chapter I paragraph C.2). The results are given in Table 2 for the two different targeted Pt loadings. The difference between the targeted and the effective loading increases with the targeted loading, suggesting that there is a loading limit owing to the surface area and wettability of the support. Scanning electron microscopy – energy dispersive X-ray spectroscopy (SEM-EDX) was also performed on the same materials and the results are also shown in Table 2. The two different methods led to very similar results and it may be concluded that 30 $\%_{wt}$ is a suitable Pt loading for the NbC nanotubes.

Table 2. Targeted and effective Pt loadings onto NbC nanotubes evaluated by XRF and SEM-EDX.

	Pt deposition 1	Pt deposition 2 (High loading)
Targeted Pt loading	35 $\%_{wt}$	50 $\%_{wt}$
Evaluated by XRF	30 $\%_{wt}$	43 $\%_{wt}$
Evaluated by SEM – EDX	30 $\%_{wt}$	41 $\%_{wt}$

For the same targeted loading of 35 $\%_{wt}$, Pt loading on NbC was higher (30 $\%_{wt}$) than on the previously described supports (20 $\%_{wt}$ onto Pt/NbC nanostructures and nanofibres - chapters II and III). Highly Pt loaded supports were prepared with the aim of enabling use of thinner catalyst layers for the MEA, that should favour lower resistivity and mass transport and therefore enhance *in situ* performance[20]**.** However, when an even higher platinum loading was targeted (50 $\%_{wt}$), it was observed in SEM that the NbC nanotubes were covered by more than one layer of platinum particles (Figure 21). Not only would the embedded platinum particles be less accessible in a catalyst layer, but also it was seen that some platinum particles agglomerated in voids between the nanotubes, and were not attached to the support. Given the different mass of niobium and carbon, the 50 $\%_{wt}$ Pt loading on a NbC support is comparable to a 75 $\%_{wt}$ for a Pt/C electrocatalyst. After this last observation and calculation, it was decided to use NbC nanotubes with 30 $\%_{wt}$ Pt loading.

D. Electrochemical characterisation of NbC nanotubes supported Pt on rotating disc electrode

1. Electrochemical surface area

Electrochemical characterisation of Pt/NbC nanotubes and a commercial 50 $\%_{wt}$ Pt/C (Alfa Aesar) was carried out using a rotating disk electrode. The ink formulations for the RDE as well as the procedure of the electrode preparation are described in the Experimental Annex (paragraph C.3.i). The cyclic voltammograms recorded at 50 $mV \cdot s^{-1}$ in N_2 saturated $HClO_4$ is displayed in Figure 22, where the current density has been normalised to the amount of platinum on the electrode. Reduction and oxidation peaks in the three typical regions of a voltammogram of Pt in acidic medium (hydrogen adsorption/desorption region, double layer region and oxide formation and reduction region) arise at the same potential than previously described in chapter II (paragraph D.1). The electrochemical surface area (ECSA) of the platinum catalyst was calculated by integrating the peak corresponding to desorption of hydrogen from the Pt sites[21,22].

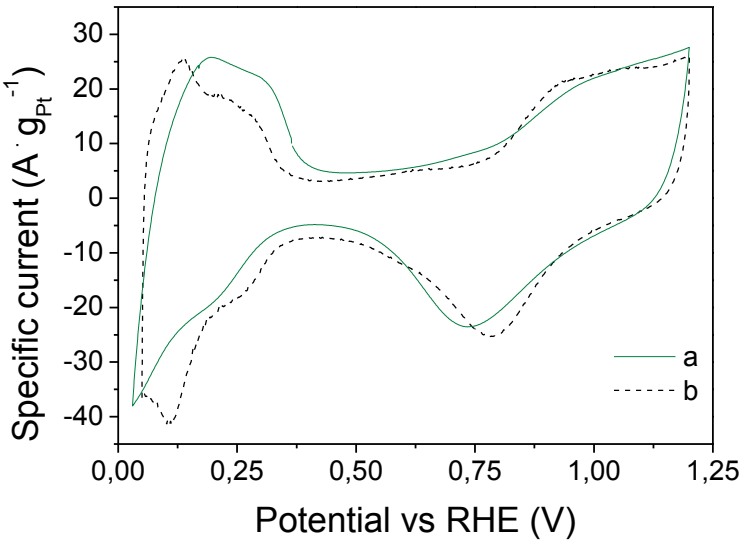

Figure 22. Cyclic voltammetry in N_2 saturated $HClO_4$ of 30 $\%_{wt}$ Pt/NbC nanotubes (a) and 50 $\%_{wt}$ Pt/C (b).

The electrochemical surface area of the 30 $\%_{wt}$ Pt on NbC nanotubes was 43 $m^2 \cdot g^{-1}$. This value is similar to that of Pt on NbC nanostructures and is comparable with the ECSA of 52 $m^2 \cdot g^{-1}$ of 50 $\%_{wt}$ Pt/C. A similar ECSA has been obtained for Pt on a niobium carbide-nitride support: using platinum particles of similar size (3 – 4 nm) to those in this work and a slightly higher loading (40 $\%_{wt}$ vs 30 $\%_{wt}$), Stamatin et al. obtained an ECSA of 49 $m^2 \cdot g^{-1}$. The ink formulation used in the present work as well as the preparation of the electrode were adapted from what is typically used for Pt/carbon and

care was taken to obtain a uniform and thin layer. However, it is difficult to prepare a suspension with catalysed nanofibrous materials because the energy required during the sonication process can lead to Pt particles detachment[23]. Therefore, a compromise between the uniformity of the thin film used as electrode and a soft ink preparation process was required.

2. Stability over time

The stability of the Pt/NbC nanotubes was investigated by applying the two accelerated stress tests to 1.2 V and 1.4 V vs RHE described previously in chapters II and III paragraph D.2:

a – A preliminary AST consisting on 3,000 electrochemical cycles at 500 $mV \cdot s^{-1}$ between 0.03 V and 1.2 V vs RHE (Figure 23a).

b - A High potential AST consisting on 10,000 electrochemical cycles at 500 $mV \cdot s^{-1}$ between 0.6 V and 1.4 V vs RHE (Figure 23b).

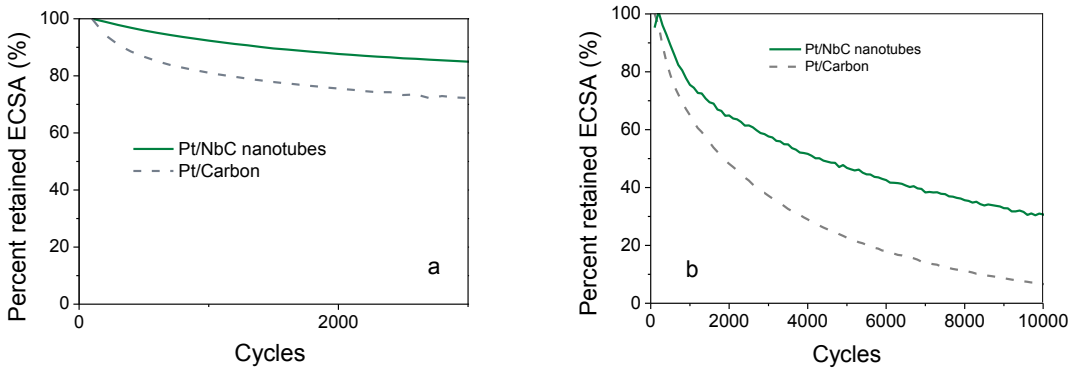

Figure 23. ECSA evolution for Pt/C and Pt/NbC nanotubes as a function of voltage cycling to 1.2 V (a) and to 1.4 V (b).

Table 3 provides a summary of the initial ECSA and its loss after voltage cycling. It may be seen that after 3,000 cycles up to 1.2 V the ECSA decreased by 12 % for the Pt/NbC nanotubes, while for the Pt/C material it decreased by 25 %. After voltage cycling, the ECSA of Pt/NbC nanotubes is the same of Pt/carbon (38 $m^2 \cdot g^{-1}$) after cycling.

Table 3. ECSA and ECSA loss of Pt/C and Pt/NbC nanotubes after voltage cycling to 1.4 V and 1.2 V.

	Pt loading *(%)*	***Initial ECSA*** *(m^2/g)*	***ECSA loss after 3000 cycles up to 1.2 V***	***ECSA after 3,000 cycles up to 1.2 V*** *(m^2/g)*	***ECSA loss after 10,000 cycles up to 1.4 V***	***ECSA after 10,000 cycles up to 1.4 V*** *(m^2/g)*
Pt/NbC nanotubes	30	43	-12 %	38	-69 %	25
Pt/Carbon	50	52	-25 %	39	-95 %	2.6

Voltage cycling up to 1.4 V for 10,000 cycles better differentiates the stability of the two supports. Under these conditions, the ECSA of Pt/C and Pt/NbC are reduced by 95 % and 69 % respectively. Pt/NbC nanotubes ECSA far exceeds that of Pt/carbon at the end of the AST (25 vs 3 $m^2 \cdot g^{-1}$) indicating that Pt/NbC nanotubes have greater stability to high voltages than Pt/carbon. The ECSA decrease can be explained by the various phenomena occurring simultaneously and already described in chapter II: degradation of the support leading to detachment of platinum particles, Pt dissolution and reprecipitation, Pt migration, agglomeration and Ostwald ripening. The significantly different results obtained when applying the two different voltage cycling protocols suggests that the better stability of 30 $\%_{wt}$ Pt/NbC nanotubes can be attributed to the higher electrochemical corrosion resistance of the NbC nanotubes support. This result suggests that the thin Nb_2O_5 layer revealed by XPS analysis possibly protects the support from further oxidation. Carbon identified as graphene layers at the surface can also explain the stability of the NbC nanotubes since graphene is less subject to corrosion[13] than the amorphous carbon identified in NbC nanostructures and nanofibres supports (The ECSA are reduced respectively by 70 % and 80 % after the 10,000-cycle AST up to 1.4V)(Figure 24)(chapters II and III).

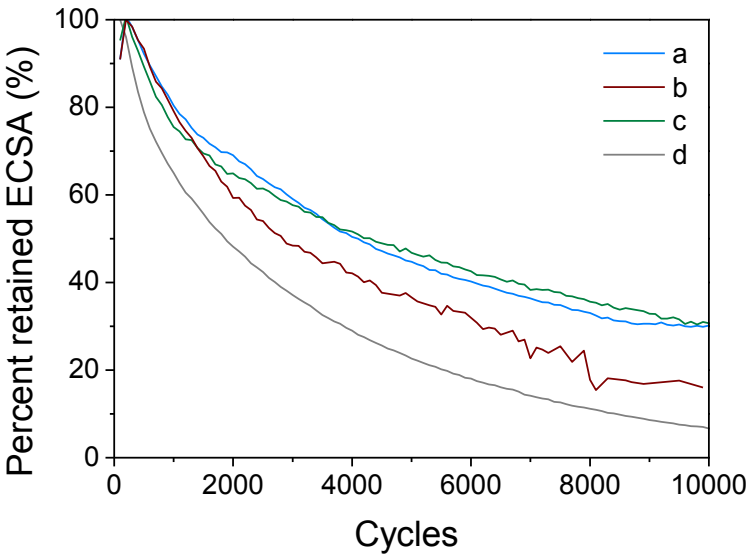

Figure 24. ECSA evolution for Pt/NbC nanostructures (a), Pt/NbC nanofibres (b), Pt/NbC nanotubes (c) and Pt/C (d) as a function of voltage cycling to 1.4 V.

3. Activity towards the oxygen reduction reaction

The ORR activity of Pt/NbC nanotubes was determined by linear sweep voltammetry in O_2 saturated $HClO_4$ 0.1 M solution in the rotating disk electrode setup. Figure 25 shows the voltammogram obtained for 30 $\%_{wt}$ Pt/NbC nanotubes and 50 $\%_{wt}$ Pt/C at 20 mV $\cdot$ s^{-1} and 1600 rpm after the subtraction of the background obtained in N_2 saturated electrolyte. A similar onset potential (1.05 V vs RHE) was observed for Pt/NbC nanotubes and Pt/C. The three typical zones described in chapter I (paragraph D.3) were observed on the voltammogram and the kinetic contribution of the current was isolated with the Koutecky-Levich equation in order to calculate the mass activities.

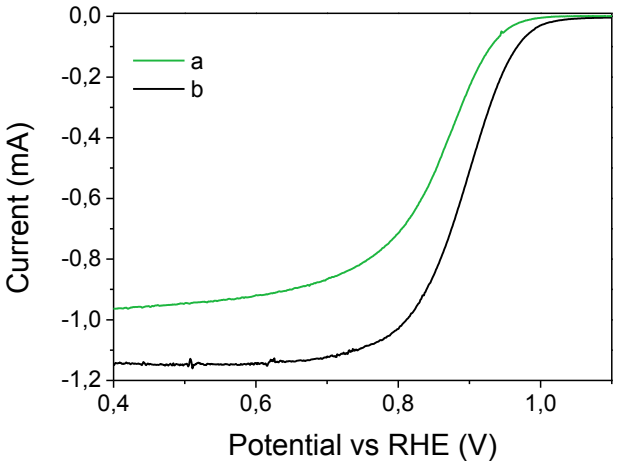

Figure 25. Polarisation curves at 1600 rpm for O_2 reduction on 30 $\%_{wt}$ Pt/NbC nanostructures (a) and 50 $\%_{wt}$ Pt/C (b).

The Tafel plot[34] is provided in Figure 26 where it may be seen that the ORR mass activities at 0.9 V are 72 and 87 $A \cdot g^{-1}_{Pt}$ for 30 $\%_{wt}$ Pt/NbC nanotubes and 50 $\%_{wt}$ Pt/C, respectively. The Tafel slope in the electron transfer control region (53 $mV \cdot dec^{-1}$) is very close to the theoretical Tafel slope of 60 $mV \cdot dec^{-1}$ [21,24].

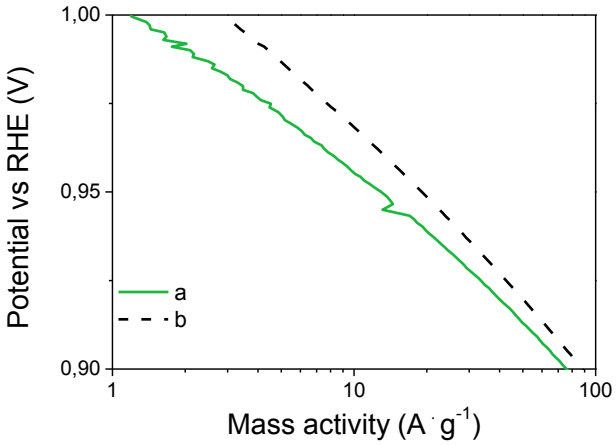

Figure 26. ORR Tafel plot for 30 $\%_{wt}$ Pt/NbC nanotubes (a) vs 50$_{wt}$ % Pt/C (b).

E. *In situ* characterisation of Pt supported on NbC nanotubes

1. MEA Preparation

A NbC based cathode was prepared by spraying a hydro-alcoholic ink made with Nafion and 30 $\%_{wt}$ Pt/NbC nanotubes onto a 4 cm^2 GDL. The cathode Pt loading was 0.2 $mg_{Pt} \cdot cm^{-2}$ (i.e. lower than the 0.5 $mg_{Pt} \cdot cm^{-2}$ used with the Pt/NbC nanofibres). The NbC cathode was associated with a commercial anode and a PFSA membrane to prepare a MEA (Experimental Annex paragraph C.3.ii). This MEA has been characterised *in situ* in a single fuel cell.

2. Performance/Characterisation

The characterisation of the Pt/NbC nanotubes MEA was performed in a 4 cm^2 single PEMFC at 80 °C and 100 % RH. The obtained polarisation curve is shown in Figure 27. The open circuit voltage is 920 mV and a maximum power density of 433 $mW \cdot cm^{-2}$ is obtained at 1200 $mA \cdot cm^{-2}$. These values are slightly lower but in the same range as the maximum density power and total resistance obtained for the Pt/NbC nanofibres based MEA (chapter III paragraph E.2) prepared with more than twice its Pt loading. These power densities could be further improved by optimising the electrode preparation.

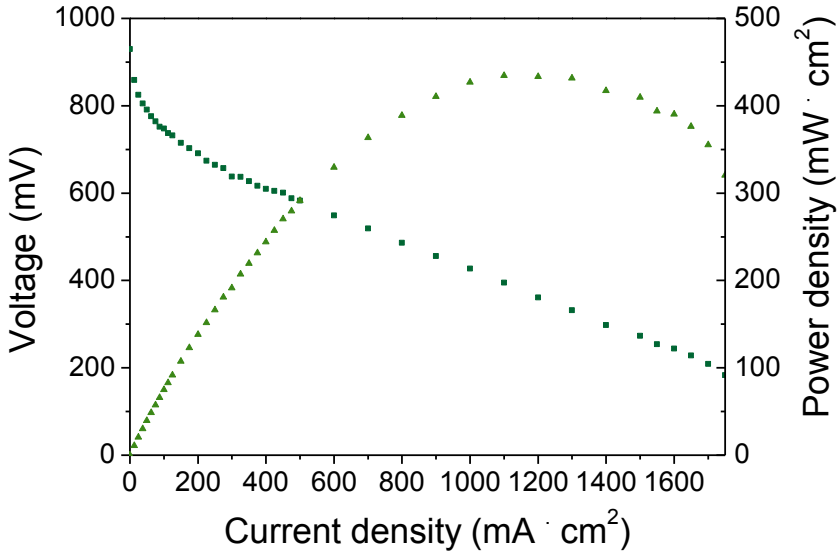

Figure 27. Polarisation curve for Pt/NbC nanotubes (0.2 $mg_{Pt} \cdot cm^{-2}$) T = 80 °C ; H_2/O_2 (1.5:2) 2.0 bar (abs); RH 100 %.

The MEA was dismounted from the cell following recording of the polarisation characteristics, and a cross-section was observed by SEM, presented in Figure 28. As expected, owing to the decrease in platinum loading (0.2 vs 0.5 $mg_{Pt} \cdot cm^{-2}$), a thinner catalyst layer can be observed than the Pt/NbC nanofibres based MEA (5 µm vs 15 µm).

The micrograph shows that the nanotube morphology was retained after electrode preparation, MEA hot-pressing and fuel cell operation. No *in situ* accelerated stress test was performed, however Pt particles appear agglomerated on the cathode side. The understanding of the reason for this catalyst degradation (ink preparation, issues related to the electrocatalyst adhesion onto the support, surface change in fuel cell conditions) requires further investigations.

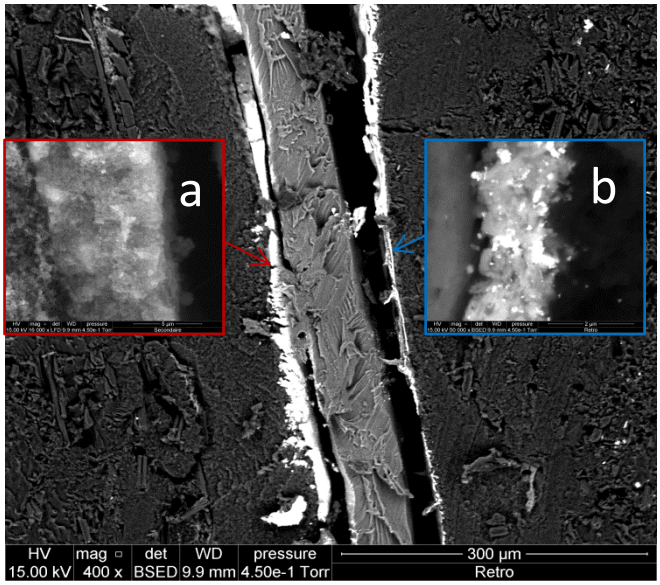

Figure 28. SEM micrograph of the membrane electrode assembly with Pt/C at the anode side (a) Pt/NbC nanotubes at the cathode side (b).

F. Conclusion and perspectives

A synthesis route for the elaboration of niobium carbide nanotubes with porous walls has been developed. It consists of three steps: electrospinning of ammonium niobate oxalate (as niobium precursor) and PVP (as carrier polymer) composite, calcination in air to remove the carrier polymer and form niobium oxide fibres, and carburation to convert niobium oxide to carbide. The fibre morphology evolves during the carburation step probably due to the grain growth, and nanotubular NbC is recovered having a residual carbon amount of 5 $\%_{wt}$. Pt nanoparticles were prepared using the microwave-assisted polyol method and deposited on nanotubular NbC. Electrochemical characterisation indicated that the ECSA of Pt on NbC is slightly lower, but similar to that of commercial Pt on carbon. Following voltage cycling the ECSA of Pt on NbC undergoes less reduction than that of Pt/C, and the final ECSA values are also significantly higher than that of Pt/C, which indicates that the NbC support material is more stable and corrosion resistant. A preliminary fuel cell measurement on a membrane electrode assembly comprising a cathode incorporating Pt/NbC (no added carbon) has shown that electrocatalysts of this type, incorporating supports of novel composition and morphology, are suitable. However, much work remains to optimise the ink composition in order to show the real potential of Pt/NbC cathode electrocatalysts. The stability of the NbC based MEA must also been assessed *in situ*, especially with accelerated stress tests mimicking the PEMFC operating conditions leading to higher cathode degradation (e.g. start-up/shut-down cycles).

Electrospinning provides the possibility to obtain self-standing mats as demonstrated in chapter IV. Further optimisation of the NbC nanotubes synthesis is required to obtain the suitable mechanical strength for them to be handled as a self-standing film. The exploratory work on electrodeposition carried out with NbC nanofibres as well as other thin layer deposition techniques (e.g. ALD) could be transposed to such self-standing NbC nanotubes mat electrodes.

The achieved morphology providing with hierarchical intra-tubes and inter-tubes porosity is also a driving force to adapt this synthesis route for the development of other transition metal carbides. For instance, the preparation of 1 D nanostructured tungsten carbide is envisaged, due to a possible synergistic effect towards the ORR catalysis (chapter I). Work for the development of catalysed WC nanofibrous materials is in progress.

G. References

1 X. Leimin, L. Shijun, Y. Lijun and L. Zhenxing, *Fuel Cells*, 2009, **9**, 101–105.

2 S. Iijima, *Nature*, 1991, **354**, 56–58.

3 R. Tenne, L. Margulis, M. Genut and G. Hodes, *Nature*, 1992, **360**, 444–446.

4 C. N. R. Rao, A. Govindaraj, G. Gundiah and S. R. C. Vivekchand, *Chem. Eng. Sci.*, 2004, **59**, 4665–4671.

5 S. R. Mishra, H. S. Rawat, S. C. Mehendale, K. C. Rustagi, A. K. Sood, R. Bandyopadhyay, A. Govindaraj and C. N. R. Rao, *Chem. Phys. Lett.*, 2000, **317**, 510–514.

6 L. K. frevel and H. W. Rinn, *Anal. Chem.*, 1955, **27**, 1329–1330.

7 F. A. O. Fontes, J. F. De Sousa, C. P. Souza, M. B. D. Bezerra and M. Benachour, *Chem. Eng. J.*, **175**, 534–538.

8 H. S. Kim, G. Bugli and G. Djéga-Mariadassou, *J. Solid State Chem.*, 1999, **142**, 100–107.

9 V. L. S. Teixeira da Silva, E. I. Ko, M. Schmal and S. T. Oyama, *Chem. Mater.*, 1995, **7**, 179–184.

10 M. T. Marques, A. M. Ferraria, J. B. Correia, A. M. B. do Rego and R. Vilar, *Mater. Chem. Phys.*, 2008, **109**, 174–180.

11 G. McGuire, G. Schweitzer and T. Carlson, *Inorg. Chem.*, 1973, **12**, 2450–2453.

12 V. L. S. Teixeira da Silva, M. Schmal and S. T. Oyama, *J. Solid State Chem.*, 1996, **123**, 168–182.

13 Y. Shao, S. Zhang, C. Wang, Z. Nie, J. Liu, Y. Wang and Y. Lin, *J. Power Sources*, 2010, **195**, 4600–4605.

14 S. Huang, H. Wu, M. Zhou, C. Zhao, Z. Yu, Z. Ruan and W. Pan, *NPG Asia Mater.*, 2014, **6**, e86.

15 M. Thommes, *Chem. Ing. Tech*, 2010, **82**, 1059.

16 G. Leofanti, M. Padovan, G. Tozzola and B. Venturelli, *Catal. Today*, 1998, **41**, 207–219.

17 C.-K. Liu, K. Lai, W. Liu, M. Yao and R.-J. Sun, *Polym. Int.*, 2009, **58**, 1341–1349.

18 I. Savych, J. Bernard d'Arbigny, S. Subianto, S. Cavaliere, D. J. Jones and J. Rozière, *J. Power Sources*, 2014, **257**, 147–155.

19 K. Wang, Z. Pan, F. Tzorbatzoglou, Y. Zhang, Y. Wang, T. Panagiotis and S. Song, *Appl. Catal. B Environ.*, 2015, **166**, 224–230.

20 L. Xiong and A. Manthiram, *Electrochim. Acta*, 2005, **50**, 3200–3204.

21 S. Gojković, S. Zečević and R. Savinell, *J. Electrochem.*, 1998, **145**, 3716–3720.

22 D. A. J. Rand and R. Woods, *J. Electroanal. Chem. Interfacial Electrochem.*, 1972, **36**, 57–69.

23 R. A. Caruso, M. Ashokkumar and F. Grieser, *Colloids Surfaces A Physicochem. Eng. Asp.*, 2000, **169**, 219–225.

24 E. Gileadi and E. Kirowa-Eisner, *Corros. Sci.*, 2005, **47**, 3068–3085.

H. Table of Figures

General Conclusion

The objective of this thesis was to develop corrosion resistant support materials that can potentially replace carbon and improve the durability of the PEMFC cathodes. Among alternative electrocatalyst supports, niobium carbide was selected for its high electronic conductivity, and high chemical and electrochemical stability. Three different synthesis routes were developed leading to different morphologies. NbC nanostructured powder were synthesised from a hydrothermal synthesis route resulting in the structuration of microspheres. This synthesis method allowed tuning the porosity of the material leading to high specific surface area (65 $m^2 \cdot g^{-1}$). 1D nanostructured materials were elaborated by associating the electrospinning technique with different heat treatments. NbC nanotubes with porous walls were obtained by carburation under methane of niobium oxide nanofibres, while NbC nanofibres were obtained by direct carburation of a niobium salt/carrier polymer composite. The latter were obtained as self-standing nanofibrous mats.

The obtained materials were characterised using various techniques including SEM, TEM, XRD, XPS, N_2 adsorption/desorption and electric conductivity measurements. Particular attention was focused on determination of NbC materials. The presence of Nb_2O_5 on the surface was identified by X-ray photoelectron spectroscopy. The presence and amount of residual carbon was determined and confirmed by combining different analytical methods. When required, the syntheses were adapted in order to minimise the amount of residual carbon. Platinum particles of average diameter 3.3 nm were synthesised by a microwave-assisted polyol method and deposited onto each type of NbC support. The electrochemical properties of the catalysed supports including their electrochemical surface area, their electrochemical stability through voltage cycling accelerated stress tests and their ORR electrocatalytic activities were determined *ex situ* on rotating disk electrodes and compared to those of a commercial Pt/C based electrocatalyst. It was concluded that the most promising materials are the catalysed NbC nanofibres and nanotubes and they were also characterised *in situ* in a single fuel cell unit.

The stability of the ECSA to voltage cycling of the NbC materials is higher to different degrees compared to the Pt/C reference. This indicates that the chosen composition is a good candidate and demonstrates the influence of the composition morphology on the electrocatalytic properties. Among the different types of NbC morphology, NbC nanotubes presented the lowest ECSA decrease on voltage cycling to 1.4 V (70 % for the NbC nanotube; 95 % for the Pt/C reference) with an ORR mass activity close to that of Pt/C (72 $A \cdot g^{-1}$ at 0.9 V vs RHE for NbC; 87 $A \cdot g^{-1}$ at 0.9 V vs RHE for the Pt/C reference). The advantage of following a two-step process (previous synthesis of the nanoparticles and subsequent deposition onto the supports) as described in this thesis allows use of

the exact same type of particles in order to compare the supports. The investigation of a “one pot” synthesis and deposition of the Pt particles is a single step process planned which may allow a better electrocatalyst adhesion onto the support resulting in further stability improvement.

To fully take advantage of the self-standing mat morphology of electrospun NbC fibres, exploratory investigation was undertaken on direct electrodeposition onto these mats used as electrodes. This led to the deposition of a network of platinum which is characterised by outstanding electrochemical stability. One remaining objective is to obtain NbC nanotubes also in self-standing form in order to transpose this work to the most promising materials synthesised. Catalyst ink preparation with nanofibres is challenging, not the least because of the amount of energy required to obtain a suspension that can affect the electrocatalyst/support adhesion. This limitation is relevant to the RDE measurements as well as the *in situ* characterisation in a single fuel cell unit. In this respect, a catalysed self-standing support with the appropriate thickness and porosity would provide adapted morphology for their direct *in situ* characterisation in an MEA. Although much further work is required on MEA preparation the preliminary *in situ* characterisation carried out in this work constitutes proof of concept of the use of NbC 1D nanostructured materials as electrocatalyst supports for PEMFC cathodes. Future *in situ* characterisation must also include accelerated stress tests to assess the stability of the catalysed support in PEMFC operating conditions. A study of any evolution of Nb_2O_5 (observed by XPS in the as prepared sample surface) during the *in situ* characterisation is planned which will further provide information on the chemical and electrochemical stability of the NbC composition.

Further investigation with larger material amounts featuring industrial catalysation processes and MEA preparation (Johnson Matthey Fuel Cells) are on-going. The development of carbide supports was recently extended to self-standing mats of WC 1D nanofibres by adapting the synthesis used for NbC nanotubes. The study of this material and its catalysation by atomic layer deposition of platinum is in progress.

Experimental Annex

A. Material preparation

1. NbC nanostructures synthesis

1 g of ammonium niobate oxalate (ANO) $(NH_4)_3[NbO(C_2O_4)_3].2H_2O$ purchased by Sigma Aldrich (99.99 %) previously dissolved in 1.4 mL of milli-Q water $(18\ M\Omega \cdot cm)$ was mixed with a solution of 0.666 g of glucose (Fluka, 99.5%) in 2 mL of ethanol. ANO and glucose blend was sealed in an autoclave for 12 hours at 170 °C. The sample was dried overnight at 80 °C. The resulting powder was heated at 1100 ° C in argon for 3 hours. The residual carbon was then removed by methanation through three heat treatments to 1100 °C under hydrogen in a temperature programmed reduction (TPR) furnace so as to monitor the amount of carbon removed with the TCD signal of a Micromeritics ASAP 2010 Chemi system)

Table 1. Synthesis route to NbC/C.

Step	Conditions
Hydrothermal synthesis	12 h 170 °C in autoclave
Carburation	3 h 1100 °C in Ar (2 °C/min)
Methanation	2h 1100 °C in H_2 (4 °C/min)

2. NbC nanofibres synthesis

0.450 g of polyacrylonitrile (PAN, Mw 150, 000, Sigma Aldrich) were dissolved in 6 g of anhydrous dimethylformamide (Sigma Aldrich, 99.8 %) (DMF) ($7\%_{wt}$). 0.760 g of niobium chloride (Sigma Aldrich, 99 %) ($10\ \%_{wt}$) were then added and the mixture was stirred overnight to obtain a clear solution. Fibres were prepared from the prepared solution by a conventional electrospinning setup (Spraybase setup), which consists of a high voltage power supply and a syringe with a stainless steel needle. A drum rotating at 300 rpm was used as the target. The electrospinning process was carried out at a fixed voltage of 14 kV, at a distance of 10 cm between the drum and the needle and at a flow rate of $0.25\ mL \cdot h^{-1}$. Fibres were collected from the rotary drum target and carburated under argon at 1100 °C during 3.5 h in a tubular furnace. This heat treatment features 2 dwells of 1 hour at 150 °C and at 250 °C. The last step of this synthesis route consisted in a methanation to remove the excess carbon and was performed with a heating ramp up to 1100 °C under hydrogen in the TPR furnace. The synthesis parameters are summarised in Table 2.

Table 2. NbC nanotubes synthesis route details.

Step	Conditions
Electrospinning	PAN (7 $\%_{wt}$) / $NbCl_5$ (10 $\%_{wt}$) Solvent: DMF
Carburation	1h 150 °C → 1h 250 °C→ 3.5 h 1100 °C in air (ramp up 0.5 °C min^{-1} / 0.5 °C min^{-1} / 5 °C min^{-1})
Methanation	1100 °C in H_2 (ramp up 4 °C min^{-1})

3. NbC nanotubes synthesis

1.8 g of ammonium niobate oxalate (ANO) $(NH_4)_3[NbO(C_2O_4)_3].2H_2O$ (Sigma Aldrich (99.99 %) were dissolved in 5 g of distilled water and mixed with 4 g of ethanol containing 0.660 g of polyvinylpyrrolidone (PVP, Mw 1,300,000, Sigma Aldrich). The ANO (20 $\%_{wt}$)/PVP (7 $\%_{wt}$) mixture was stirred until a clear solution was obtained. The corresponding fibres were electrospun (Spraybase setup) at 0.2 $mL \cdot h^{-1}$ under a voltage of 15 kV at a needle-target distance of 10 cm. The collected ANO-PVP composite fibres were oxidized in air at 600 ° C for 3 h to remove the carrier polymer and form Nb_2O_5 fibres. The latter were then heated at 4 °C $\cdot$ min^{-1} to 1100 °C in 10 % CH_4/H_2 mixture gas at a total flow rate of 100 $mL \cdot min^{-1}$. The carburation was carried out in a temperature programmed reduction furnace so as to stop the experiment after the total conversion of Nb_2O_5 to NbC. The successive reactions were monitored with the TCD signal of a Micromeritics ASAP 2010 Chemi System. Table 3 shows the detailed synthesis steps.

Table 3. NbC nanotubes synthesis route details.

Step	Conditions
Electrospinning	PVP (13 %)/ANO (19.5 %) Solvent: H_2O/EtOH (50/50 volume) Voltage 15 kV; flow rate 0.2 $mL \cdot h^{-1}$; rotary drum 300 rpm
Calcination	1h 150 °C → 1h 250 °C→ 3 h 600 °C in air (ramp up 0.5 °C min^{-1} / 0.5 °C min^{-1} / 5 °C min^{-1})
Carburation	180 min at 1100 °C in CH_4/H_2 (ramp up 4 °C min^{-1})

B. Electrocatalyst synthesis and deposition

1. Microwave assisted Polyol method

70 mg of hexachloroplatinic acid (H_2PtCl_6. $6H_2O$, 99.9 % Alfa Aesar) were dissolved in 50 mL of ethylene glycol (99.5 %, Fluka) and the pH adjusted to 11 using a 1 M NaOH solution (98 %, Sigma Aldrich) in ethylene glycol. The resulting solution was heated at 120 °C for 6 minutes in a microwave reactor (MiniFlow 200SS Sairem). A suspension containing 40 mg of the NbC nanotubes in 5 mL ethylene glycol was added to the as-synthesised Pt nanoparticle suspension and the pH was adjusted to 4 in order to improve the adhesion of the electrocatalyst onto the support. After gentle stirring for 24 hours, the product was recovered by filtration, washed with milli-Q water and ethanol and dried overnight at 80 °C. A heat treatment at 160 °C for one hour was carried out as an activation step to remove ethylene glycol from the nanoparticle surface.

2. Electrodeposition

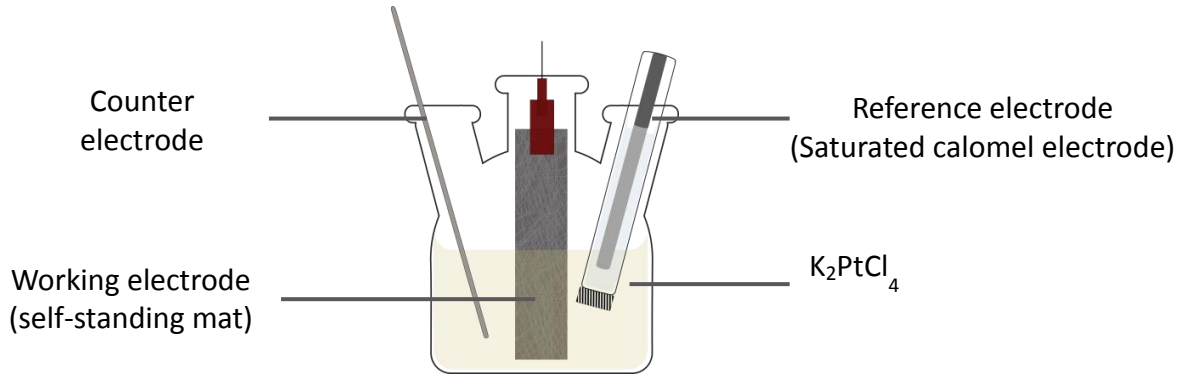

Figure 1. electrodeposition setup.

Electrodeposition were performed in a 3-electrode cell (Pt wire as counter electrode, saturated calomel electrode as reference electrode and the self-standing mat of the NbC material to catalyse as working electrode) and a Bio-Logic SP-150 potentiostat (Figure 1). Copper underpotential deposition (UPD) was performed in a copper solution ($CuCl_2$ (Sigma Aldrich, 97 %), 0.001 $mol \cdot L^{-1}$) with NaCl (0.1 $mol \cdot L^{-1}$) at -0.100 V vs SCE during 30 minutes. Linear sweep from different UPD deposition potentials to 0.8 V vs SCE were recorded so as to calculate the amount of deposited copper. The direct electrodeposition of platinum particles was performed in a K_2PtCl_4 solution (0.003 $mol \cdot L^{-1}$) and NaCl solution (0.5 $mol.L^{-1}$) prepared by dissolving K_2PtCl_4 (Sigma Aldrich, 99 %) and NaCl (VWR, 99.9 %) in deionized water (the pH of the solution was adjusted to 4 with HCl (VWR, 37 %). The material was catalysed by 10 cycles consisting on switching between - 0.9 V vs SCE for 10 seconds and at 0.4 V vs SCE for 30 minute (rest time).

3. Galvanic displacement

Galvanic displacement was used to exchange copper that was deposited by UPD onto niobium carbide with platinum. In that case, the previously copper coated self-standing mat was soaked in a chloroplatinic solution (H_2PtCl_6 0.002 mol·L^{-1}, HCl 0.05 mol·L^{-1}) at 80 °C for 1 hour. Afterwards, the sample was rinsed 4 times in deionised water.

C. Characterisation

1. Morphological characterisation

i. Electron microscopies

The morphology of the material was observed using a Hitachi S-4800 Scanning electron microscope (SEM), FEI Quanta FEG 200 and equipped with energy-dispersive spectroscopy analysis (EDX) and JEOL 1200 EXII transmission electron microscope (TEM) operating at 120 kV, equipped with a CCD camera SIS Olympus Quemesa (11 million pixels). For SEM observation, samples were prepared by dusting the SEM stub with the material to analyse. For TEM analyses, samples were suspended in isopropanol and sonicated before deposition onto carbon-coated copper grids. The diameters of the Pt nanoparticles, diameters of the fibres and diameters of the grains were determined by measuring at least 100 selected particles using the Image J software.

For a more accurate identification of the composition of nanostructured material, an elemental mapping was achieved using Tecnai F20 Transmission Electron Microscope operating at 200 kV with a 30 and 50 µm and a bright-field imaging mode using CCD high magnification lattice resolution imaging mode and CCD dark-field (Z-contrast) imaging in scanning mode using an off-axis annular detector compositional analysis by X-ray emission detection in the scanning mode.

ii. Nitrogen adsorption/desorption

With the purpose of calculate the main textural parameters of a porous material, such as specific surface area, nitrogen adsorption and desorption at -196 °C (77 K) were measured using a Micromeritics ASAP 2020 apparatus after outgassing overnight at 130 °C. The specific surface area was calculated using the Brunauer-Emmett-Teller (BET) equation[2], taking 0.162 nm^2 as the cross-sectional area of one N_2 molecule.

2. Compositional and structural characterisation

i. X-Ray Diffraction

Patterns of the synthesised support were recorded at room temperature in Bragg-Brentano configuration using a PANAlytical X'pert diffractometer, equipped with a hybrid monochromator, operating with CuK_α radiation (λ = 1.541 Å), and using a step size of 0.1° 2θ within the 2θ domain from 10 to 80 °.

The crystallite size composing the platinum particles and the NbC support were calculated with the Scherrer formula (1) applied on the broadened peaks matching the plans [111], [200] and [220] of Pt nanoparticles or of the NbC supports.

$$L = K \lambda / (\beta obs - \beta instr) \cos(\theta) \quad \textbf{(1)}$$

L = Cristallite size (nm)
l = wavelength of the radiation (nm)
K = Scherrer constant 0.94
βobs = observed FWHM (radian)
βinstr = instrumental broadening (radian)

ii. Thermogravimetric analysis

Thermogravimetric analysis, (TGA) measures of the mass variation of a sample when is exposed to temperature changes in a controlled atmosphere. This variation can be either positive or negative (mass gain or loss). Registration of these changes will provide with information about the sample decomposition with temperature. In this work, TGA (Netzsch STA 409 PC apparatus) was used to determine the amount of residual carbon (i.e. $C_{residual}$ weight to the total weight of niobium carbide + $C_{residual}$) by heating up to 1100 °C in air at 4 °C·min^{-1}. TGA was also performed in air up to 1000 °C at 10 °C · min^{-1} on composite ANO/PVP electrospun nanofibres in order to determine characteristic weight loss profiles and polymer decomposition temperature.

iii. Elemental analysis

Carbon contents in the support have been confirmed by an elemental analyser Thermo FLASH EA 1112. This equipment works by high temperature flash combustion in continuous flow, which allows to quantify with precision the amount of carbon, hydrogen, nitrogen and sulphur (CHNS) present in the samples.

iv. X-ray photoelectron spectroscopy

X-ray photoelectron spectroscopy was performed using a Physical Electronics PHI 5700 spectrometer with a non-monochromatic Mg Kα radiation (300 W, 15 kV, hv = 1253.6 eV) as excitation source. Spectra were recorded at a 45° take-off angle by a concentric hemispherical analyser operating in the

constant pass energy mode at 25.9 eV, using a 720 µm diameter analysis area. Powdered solids were mounted on a sample holder without adhesive tape and kept overnight in a high vacuum chamber before they were transferred inside the analysis chamber of the spectrometer. Each region was scanned with several sweeps until a good signal to noise ratio was observed. The pressure in the analysis chamber was maintained below 10^{-7} Pa. PHI ACCESS ESCA-V6.0 F and Multipak 8.2b software packages were used for acquisition and data analysis. A Shirley type background was subtracted from the signals. Recorded spectra were always fitted using Gauss–Lorentz curves in order to determine the binding energy of the different element core levels more accurately. The accuracy of the binding energy (BE) values was within ±0.1 eV.

v. X-ray fluorescence

X-ray fluorescence (XRF) analysis performed with a PANalytical Axios Max spectrometer fitted with a Rh (4kW) tube in order to investigate the NbC/C and Pt/NbC ratios. Omnian software and LiF200 crystal have been used for these analyses. The samples were prepared by grinding 50 mg of the support with 25 mg of H_3BO_3 to facilitate the formatting of the pellet. The recovered powder was then placed in a cavity in the H_3BO_3 matrix subsequently pressed, in order to obtain a pellet of 32 mm diameter with scanned surface of circa 12 mm. The same protocol was followed to prepare five standard samples using commercial NbC (Alfa Aesar) and carbon Vulcan XC 72 R to obtain a calibration lines. This protocol was also used to prepare five standard samples with Pt black (Alfa Aesar) and commercial NbC (Alfa Aesar) in order to investigate the Pt loading obtain after the Pt particles synthesized by polyol. Pt/Nb ratio was determined by X-ray fluorescence using two calibrations with standards made by mixing carbon Vulcan XC 72 R and commercial niobium carbide.

3. Electrochemical characterisation

i. *Ex situ* characterisation

The electrochemical analyses were carried out in a three-electrode cell comprising a glassy carbon disk electrode with surface area of 0.196 cm^2 (working electrode), a reversible hydrogen electrode (RHE, reference electrode), a platinum wire (counter electrode), and a Bio-Logic SP-150 potentiostat (Figure 2).

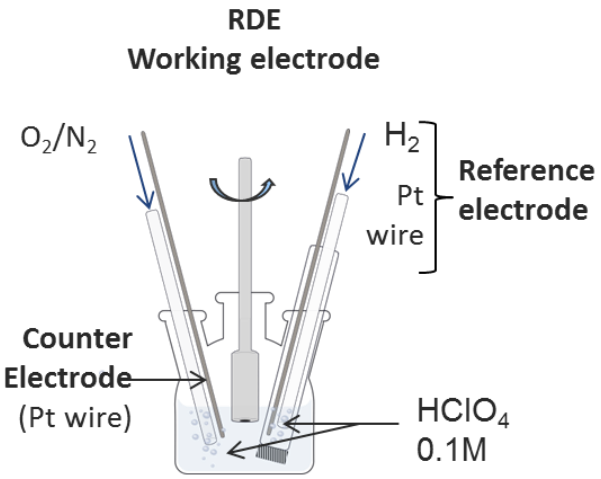

Figure 2. RDE setup used for the *ex situ* electrochemical characterisation.

The inks were prepared by adding the catalysed support (in isopropanol (Sigma Aldrich, 99.8 %)/H_2O) (4/1). The mixture was sonicated until a homogeneous suspension was obtained. 1.5 $\%_{wt}$ of a 5 $\%_{wt}$ Nafion solution was added at the end before a last sonication. The working electrode was prepared by depositing 5 µL of the dispersion on the rotation disk (The solvent was evaporated by spin coating in air). The amount of catalysed support was adapted given the effective Pt loading in order to load the disk electrode with an amount of platinum in the range of 10 – 20 µg of platinum (5.10^1 – 10^2 µg $\cdot$ cm^{-2}). Prior to the electrochemical characterisation, the 0.1 mol $\cdot$ L^{-1} $HClO_4$ solution (prepared from the trace select perchloric acid for ultra-trace analysis (sigma Aldrich, 67-72 %) was saturated with nitrogen and 100 cyclic voltammetry were performed between 0.05 and 1.2 V vs RHE as activation step. The ECSA was evaluated from the hydrogen adsorption peaks (between 0.05 - 0.4 V vs RHE), assuming a hydrogen adsorption charge of 210 µC $\cdot$ cm^{-2} for the electroactive Pt surface. Cyclic voltammetry was performed at 50 mV $\cdot$ s^{-1} between 0.05 and 1.2 V vs RHE or at 500 mV $\cdot$ s^{-1} between 0.6 -1.4 V vs RHE respectively for the determination of the ECSA or as cycles of the accelerated stress test. The investigation of the electrocatalytic activity towards the ORR was performed on rotating disk electrode (RDE) at 1600 rpm, linear sweep at 20 mV $\cdot$ s^{-1} between 0.05 and 1.2 V vs RHE were recorded in oxygen and nitrogen saturated $HClO_4$ in order to subtract the background.

ii. *In situ* characterisation

Prior to the assembly, Nafion 212 membranes with 50 µm thickness were treated using the following procedure: they were immersed in a 3 $\%_{v/v}$ H_2O_2 solution (30 $\%_{wt}$, Carlo Erba Reagents), which was then stirred for 1 h at 100 °C. After washing with water, the membranes were immersed in a 50 $\%_{w/w}$ solution of HNO_3 (65 $\%_{wt}$, Sigma Aldrich), which was then stirred for 30 min at room temperature. Finally, the membranes were washed, immersed in a 1 mol $\cdot$ L^{-1} solution of H_2SO_4 (95 $\%_{wt}$, Sigma Aldrich) for 1 h at 100 °C. After such treatments, the membranes were rinsed and stored in plastic

bags. A hydro-alcoolic ink with 15 % of Nafion and 85 % of the catalysed support previously sonicated for at least 1 hour was sprayed on a 4 cm^2 gas diffusion layer (GDL) (Sigracet S10 BC) targeting platinum loadings of 0.5 $mg_{Pt} \cdot cm^{-2}$ for the nanofibres and 0.2 $mg_{Pt} \cdot cm^{-2}$ for the nanotubes and a Nafion loading of 0.5 $mg \cdot cm^{-2}$ (loadings were controlled by weight). This cathode was associated with a commercial Pt/C sigracet S10 BC (0.5 $mg_{Pt} \cdot cm^{-2}$) on the anode side. MEA was assembled by pressing the electrodes and membrane at 140 °C for 2 min at 6.8 10^7 Pa. The MEA was then incorporated in the fuel cell setup using fluorinated ethylene propylene (FEP) gaskets at 10 - 15 % compression in order to prevent leakage of the reactants. The MEA break-in step was performed prior to the actual tests at 0.5 $A \cdot cm^{-2}$ overnight at 80 °C. H_2 and O_2 were bubbled through milli-Q water, which was heated at 80 °C. The humidity of the reactant gases was maintained at 100 % RH for both cathode and anode sides for all MEAs. Polarisation curves and impedance measurements were carried out under H_2/O_2 (using a 1.5/2 stoichiometry) by setting the current density and measuring the cell potential. Tests were performed under the pressure of 1 bar (2 bar absolute pressure).

4. Electrical conductivity

Pellets of 12 mm in diameter and of 250 - 600 µm thick were obtained by using a cylindrical die and then compressed using a manual hydraulic press during 5 minutes at 3.4 10^8 Pa. The thickness of the pellet was measured using a micrometer caliper. The electrical conductivity of the obtained pellets was measured using Van der Pauw method with an in-house developed conductivity cell. In order to achieve a suitable cohesion of the pellet, 20 % of Nafion (5 $\%_{wt}$ dispersion Aldrich) was added as a binder to the sample was added. The obtained mixture was oven dried at 80 °C overnight.

5. Chemical stability in acid

The chemical stability was investigated by measuring the mass loss of the material after 24 hours at 80 °C in acid (1 M H_2SO_4). A sample of 1 g was added to 100 mL of 1 M sulphuric acid. The mixture was heated up to 80 °C in a round bottomed flask fitted with a reflux condenser. After 24 hours the acid was diluted in water and centrifuged. The washing water was removed and deionized water was added to clean the sample. This washing procedure was repeated 4 times until a neutral pH was obtained. The solid was then dried overnight at 100 °C and the resulting solid sample was weighted. X-ray diffraction was also performed before and after the test to confirm that no structural change occurred during the acid treatment.

GLOSSARY

1D, 2D, 3D: 1-dimensional, 2-dimensional, 3-dimensional

ANO: ammonium niobate oxalate

ALD: atomic layer deposition

AST: accelerated stress test

CNT: carbon nanotubes

COOR: CO oxidation reaction

DMF: dimethylformamide

EDX: energy dispersive x-ray spectroscopy

ECSA: electrochemical surface area

ED: electrodeposition

FE SEM: field emission scanning electron microscopy

HOR: Hydrogen oxidation reaction

MOR: Methanol oxidation reaction

ORR: oxygen reduction reaction

PAN: polyacrylonitrile

PUF: polyureaformamide

PVA: polyvinylalcohol

PVP: polyvinylpyrrolidone

PGM: platinum group metal

RDE: rotating disk electrode

RHE: reversible hydrogen electrode

SCE: saturated calomel electrode

SEM: scanning electron microscopy

TMC: transition metal carbide

TCD: thermal conductivity detector

TEM: transmission electron microscopy

TGA: thermogravimetric analysis

TPR: temperature programmed reduction

UPD: under potential deposition

XRD: X-ray diffraction

Abstract

One pivotal issue to be overcome for the widespread adoption of Proton exchange membrane fuel cells (PEMFC) is the stability overtime. In this context, This PhD project focuses on the elaboration of niobium carbide based electrocatalyst supports for the PEMFC cathode to replace the conventional carbon based supports that notoriously suffer from corrosion in fuel cell operating conditions. The approach is to associate this alternative chemical composition with controlled morphologies in order to design electronically conductive and chemically stable materials with the appropriate porosity. Three different syntheses involving hydrothermal template synthesis or electrospinning have been developed leading to three different morphologies: nanostructured powders with high surface area, self-standing nanofibrous mats, and nanotubes with porous walls. These various supports have been catalysed by deposition of platinum nanoparticles synthesised by a microwave-assisted polyol method, and they have been characterised for their chemical and structural composition, morphology, and electrochemical properties. This work demonstrates that the Pt loaded NbC supports feature a greater electrochemical stability than a commercial Pt/C reference and similar electrocatalytic activities towards the oxygen reduction reaction.

Keywords: Niobium carbide; electrocatalyst support; oxygen reduction reaction; electrospinning; energy conversion devices; controlled morphology; nanotubes; nanofibres.

Résumé

La durabilité des piles à combustible à membrane échangeuse de proton (PEMFC) est un des verrous technologiques majeurs qui freinent leurs implantations sur le marché. Ces travaux de thèse s'inscrivent dans ce contexte en proposant l'élaboration de matériaux en carbure de niobium comme support de catalyseur pour remplacer les supports carbonés actuellement utilisés dans les cathodes de PEMFC. Notre démarche est d'associer cette composition à différentes morphologies contrôlées pour développer des matériaux conducteurs, présentant une porosité adaptée et chimiquement plus stable que le carbone qui se corrode dans les conditions de fonctionnement des PEMFC. Ainsi trois voies de synthèse basées sur des techniques variées (filage électrostatique, synthèse hydrothermal avec agent structurant) ont été étudiées aboutissant à trois types de morphologie : des poudres nanostructurées, des tissus nanofibreux et des nanotubes aux parois poreuses. Après leurs caractérisations structurales et morphologiques approfondies, ces supports ont été catalysés avec des nanoparticules de platine synthétisées par une méthode polyol assisté par micro-onde. La finalité de ce projet est d'évaluer les performances électrochimiques relatives à la réaction de réduction de l'oxygène de ces supports catalysés pour mettre en avant leurs exceptionnelles stabilités comparées à un support catalysé de référence (Pt/C) sans perte significative d'activité catalytique.

Mots clefs : Carbure de niobium ; Support de catalyseur ; Réduction de l'oxygène ; électrofilage électrostatique ; conversion d'énergie ; morphologie contrôlée ; nanotubes ; nanofibres.

Laboratoire Agregats, Interfaces et Matériaux pour l'Energie UMR5253 – CC1502
Université de Montpellier,Place Eugène Bataillon – 34095 Montpellier Cedex 5